Lifetime of Atomic Spin Chains

Enhancing spin lifetime, remote detection of magnons and implementation of ESR-STM

Elbertse, R.J.G.

DOI
10.4233/uuid:e9374d12-699f-46e5-b963-ae061690b0b3

Publication date
2022

Document Version
Final published version

Citation (APA)
Elbertse, R. J. G. (2022). *Lifetime of Atomic Spin Chains: Enhancing spin lifetime, remote detection of magnons and implementation of ESR-STM*. [Dissertation (TU Delft), Delft University of Technology]. https://doi.org/10.4233/uuid:e9374d12-699f-46e5-b963-ae061690b0b3

Lifetime of Atomic Spin Chains

Enhancing spin lifetime, remote detection of magnons and implementation of ESR-STM

LIFETIME OF ATOMIC SPIN CHAINS

ENHANCING SPIN LIFETIME, REMOTE DETECTION OF MAGNONS AND IMPLEMENTATION OF ESR-STM

Dissertation

for the purpose of obtaining the degree of doctor
at Delft University of Technology
by the authority of the Rector Magnificus, Prof. Dr. Ir. T.H.J.J. van der Hagen,
chair of the Board for Doctorates
to be defended publicly on
Wednesday 23 November 2022 at 10:00 o'clock

by

Robbie ELBERTSE

Master of Science in Applied Physics, Delft University of Technology, the Netherlands
born in Zoetermeer, the Netherland.

This dissertation has been approved by the promotors.

Composition of the doctoral committee::

Rector Magnificus,	Chairperson
Prof. dr. A. F. Otte,	Delft University of Technology, promotor
Prof. dr. H. S. J. van de Zant	Delft University of Technology, promotor

Independent members:

Prof. dr. Y. Blanter,	Delft University of Technology
Prof. dr. G. A. Steele,	Delft University of Technology
Prof. Dr. S. Loth,	Universität Stuttgart, Duitsland
Prof. dr. A. J. Heinrich	Center for Quantum Nanoscience Seoul, South-Korea
Prof. dr. F. Delgado Acosta	Universidad de la Laguna, Spain
Prof. dr. S. C. Conesa Boj	Delft University of Technology

Keywords: Spin chain, lifetime, diabolic, ESR-STM, Remote detection

Printed by: Gildeprint

Front & Back: Three dimensional rendering of (front) a magnon on an atomic chain headed towards an atomic detector, (back bottom) an atomic spin chain in a superposition and (back top) a magnetic tip excited by a photon probing an atom.

Casimir PhD-Series 2022-35
ISBN 978-90-8593-544-5

An electronic version of this dissertation is available at
http://repository.tudelft.nl/.

Contents

SUMMARY

This thesis describes atomic spin chains subject to magnetic anisotropy. Such chains, assembled through means of scanning tunneling microscopy (STM), can be home to a plethora of magnetic states and spin physics. This includes quantum tunneling of magnetization, the injection and delocalization of magnons and, for single atoms, the application of electron spin resonance (ESR). Each phenomenon happens at their own timescale which is dependent on the isolation of the spin chain from the environment, ranging from seconds to picoseconds.

Chapter 1 introduces the topic of scanning tunneling microscopy and summarized the thesis in detail. The purpose is to provide meaning to those who are not as familiar with university-level physics. Addressed is the operation of STM, basic descriptions of spin states and superposition and the main Hamiltonian used throughout this thesis is described. The chapter ends with a quick glance on how the lifetime of Fe chains on $Cu_2N/Cu(100)$ can be enhanced, what magnons are and how they are recorded and why the installation of an antenna is necessary for ESR-STM.

Chapter 2 provides the theoretical foundation of the thesis. The main Hamiltonian is built up from its parts, and in each step an exploration of the lifetime of the two lowest energy states is provided. This leads to the finding that when applying a magnetic field along the hard axis of a chain of Fe atoms on $Cu_2N/Cu(100)$ an energy crossing occurs called a diabolic point. Close to this diabolic point, with the application of a small value of a field along the easy axis, the lifetimes of the two states increases by orders of magnitude as the so-called scattering amplitude dips to a minimum. This scattering amplitude is a measure for how likely a quantum tunneling of magnetization is to occur and also takes into account spin flip-flops of tunneling electrons. It is found that for an $S = 2$ system there are 2 diabolic points, and a chain is built of length N there are $2N$ diabolic points. Finally, a brief introduction into magnons is provided.

Chapter 3 describes the experimental methods. This includes an explanation of how scanning tunneling microscopy works and compares some details of three different STM machines. The chapter then goes into three methods: inelastic electron tunneling spectroscopy (IETS), pump and probe (P&P) and electron spin resonance (ESR), all in the context of STM. Each method is described in three parts: key results both from the field and in the context of this thesis, the physics behind the method and the implementation. For the implementation of P&P and ESR-STM simulations involving Markov Chains are presented, to illustrate the time ensemble measurement.

Chapter 4 shows experimental results on the lifetime enhancement near a diabolic point. The experiments are performed on Fe_5 and Fe_6 and show that lifetime of the two

lowest energy states can be increased by 2-3 orders of magnitude, leading to a lifetime of more than 30 s for Fe_6. The phenomenon is robust to changes in experimental settings such as magnetic field not along the hard axis, tip-sample voltage and current setpoint. Supported by simulations, we find that the even chain Fe_6 experiences different g-factors for each atom, which leads a lifting of the otherwise degenerate ground states. Two follow-up experiments are proposed, one in which a second diabolic point is measured and one in which the peak in the lifetime is used for spectroscopic purposes to find the coupling strength between the chain and an atom with its easy axis perpendicular to that of the chain.

Chapter 5 addresses the higher-lying states of these atomic spin chains. Through injection tunneling electrons, effectively S_+ and S_- operators are applied on the system, which brings the chain into a superposition of energy states. The result is a magnon which delocalizes across the chain and decays in about 10 ps. A nearby atomic detector is built to detect and record the arrival of these magnons at the end of the chain. Statistics are gathered on the arrival rate in various set-ups and the results are corroborated with simulations, indicating a correct understanding of the underlying physics of magnons. The longest travel distance measured is 9 atoms, which amounts to 6.8 nm.

Chapter 6 explores the installation of an antenna for transmission of radio frequency (RF) signals to the tip-sample junction. This is done in the context of ESR-STM which requires such signals. The chapter covers tests to determine the best cabling leading to the antenna, and tests to determine the best set-up of the antenna close to the tip-sample junction. During the installation *ex situ* transmission data is recorded which is then compared with *in situ* data and shows a compare transmission. The chapter closes off with some basic ESR-STM data and interpretation for illustrative purposes.

SAMENVATTING

Deze scriptie beschrijft atomaire spinketens die magnetische anisotropie ondervinden. Zulke ketens, gebouwd met behulp van scanning tunneling microscopy (STM), kunnen verscheidene magnetische toestanden en spin fysica bevatten, waaronder kwantum tunneling van magnetizatie, de injectie en delocalizering van magnonen en, voor enkele atomen, de toepassing van electron spin resonantie (ESR). Elk van deze fenomenen gebeurt op hun eigen tijdsschaal, uitlopend van seconden tot picoseconden, die afhankelijk is van de mate waarop de keten geïsoleerd is van de omgeving,

Hoofdstuk 1 introduceert de scanning tunneling microscoop en vat de gehele thesis samen in grote detail. Het doel van dit hoofdstuk is om de thesis ook toegankelijk te maken voor hen die geen universiteits-niveau natuurkunde hebben gevolgd. Beschreven wordt hoe de STM werkt, hoe spintoestanden en superposities werken ook en de voornaamste Hamiltoniaan die gebruikt wordt in de thesis. Het hoofdstuk eindigt met een korte blik op hoe de levensduur van Fe ketens op $Cu_2N/Cu(100)$ verlengt kan worden, wat magnonen zijn en ze gedetecteerd kunnen worden en waarom de installatie van een antenne noodzakkelijk is voor ESR-STM.

Hoofdstuk 2 bouwt de theoretische basis van deze scriptie op. Hierbij wordt de Hamiltoniaan opgebouwd vanuit zijn onderdelen en wordt in elke step gekeken naar de levenduur van de twee laagste energietoestanden, Hierin wordt duidelijk dat het toepassen van een magneetveld langs de harde as van een keten van Fe atomen op $Cu_2N/Cu(100)$ zorgt voor een energiekruising, ookwel een diabolisch punt genoemd. Dicht bij dit diabolisch punt, met een klein magneetveld langs de gemakkelijke as, kan de levenduur van de twee toestanden met enkele ordergroottes toenemen. Tegelijkertijd neemt de zogenoemde verstrooiingsamplitude af. Dit is een maat van hoe waarschijnlijk een kwantum tunneling van magnetizatie kan plaatsvinden, en neemt ook spin flip-flops door tunneling electronen met zich mee. We vinden dat voor een S = 2 systeem dat er twee diabolische punten zijn en dat een keten met lengte N zorgt voor $2N$ diabolische punten. Op het einde wordt een kleine introductie tot magnonen gegeven.

Hoofdstuk 3 beschrijft de experimentele methodes. Hierin wordt ook uitgelegd hoe scanning tunneling microscopie werkt en worden de details van drie verschillende STMs met elkaar vergeleken. Het hoofdstuk gaat daarna in de diepte voor drie STM methodes: inelastische electron tunneling spectroscopy (IETS), pump en probe (P&P) en electron spin resonantie (ESR). Elke methode wordt in drie delen beschreven: de hoofdresulten zowel van ander onderzoek als mijn eigen werk, de fysica die achter de methoden zit en de implementatie. Voor de implementatie van P&P en ESR-STM zijn er Markov Keten simulatie gedaan die de tijdsensemble uitgelegd.

Hoofdstuk 4 laat experimentele resultaten zien van de levensduurverlenging nabij een diabolisch punt. De experimenten zijn uitgevoefd op Fe_5 en Fe_6 en laten zien dat de levensduur van de twee laagste energietoestanden met zo'n 2-3 ordergrootte kan worden verlengd, wat leidt tot een levensduur van meer dan 30 s voor Fe_6. Dit fenomeen is robuust tegen veranderingen in experimentele omstandigeheden zoals magneetveld langs een andere as dan de harde as, tip-substraat spanning of de tunnelstroom. Ondersteund door simulatie, vinden we dat voor de even keten Fe_6 de verschillende atomen een andere g-factoor hebben, wat de ontaarding van de grondtoestanden opheft. Twee vervolgonderzoeken worden voorgesteld. De eerste waarbij een tweede diabolisch punt wordt gemeten. De andere waarbij de piek in de levenduur voor spectroscopie wordt toegepast, waarmee de koppelingsenergie tussen de keten en een ander atoom met zijn gemakkelijke as loodrecht op die van de keten kan worden vastgestelt.

Hoofdstuk 5 verdiept zich in de hogere energietoestanden van deze atomaire spinketens. Door het injecteren van de tunnelelektronen wordt er effectief een S_+ of S_- operator toegepast op de Hamiltoniaan, wat de keten in een superpositie van hogere energietoestanden brengt. Dit resulteerd in een magnoon die zich delocalizeerd over de keten en na ongeveerd 10 ps uitdooft. Een nabije atomaire detector is gebouwd die de aankomst van de magnoon op de laatste atoom van de keten detecteert. Met voldoende statistiek over de aankomstkans in verschillende ketens en opstellingen kunnen de resultaten vergeleken worden met simulaties, wat heeft geleidt tot een indicatie dat de theorie goed begrepen is. De langste gemeten magnoon reisafsafstand is 9 atomen, wat neer komt op 6.8 nm.

Hoofstuk 6 onderzoekt de installatie van een antenne voor de transmissie van radio frequent (RF) signalen naar de tip-substraat junctie. Dit wordt gedaan in de context can ESR-STM die dit soort signalen nodig heeft. Het hoofdstuk gaat over tests die gedaan zijn om de beste bekabeling naar de antenne te bepalen, en tests om de beste opstelling voor de antenne te bepalen. Tijdens de installatie zijn er *ex situ* metingen gedann van de transmissie, die vervolgens met *in situ* metingen vergeleken kunnen worden, wat leidt tot een goede overéénkomst. Het hoofdstuk eindigt met wat basis ESR-STM metingen in de interpretatie daarvan.

PREFACE

The advancement of science cannot be seen as the work of only researchers. For what is a scientist, without a equipment? A theoretician will need a computer, an experimentalist will need their experimental setup. Both require funding and companies that provide such hardware. And both require a society that supports the advancement of science through labour and goals. As such, I find it a scientist's duty to give their knowledge back to society. With that in mind, Chapter 1 will cover the entire thesis with an audience in mind that has a high-school level physics understanding and mathematics.

On a similar note, the implementation of Open Data supports the idea that a researcher's work is available to all. Hence I strive to provide an adequate Open Data folder for all my first author publications which is not just a data dump, but provides context. The additional advantage here is that this ensures proper and structured archiving of important data. The data from Chapter 5 is already available on doi:

https://doi.org/10.5281/zenodo.3759448

Further data may become available pending publications.

Robbie Elbertse
Delft, July 2022

1

INTRODUCTION

1.1. OVERVIEW

This thesis has three highlights to share. First is the theoretical and experimental finding of diabolic points in atomic spin chains which can be used for enhancing spin lifetime, explored in Chapter 2 and Chapter 4, respectively. Second is a scheme for detecting short-lived spin waves on these spin chains. Through means of an atomic trap, theoretical understanding of these waves is corroborated in Chapter 5 Finally, in light of the recent developments around ESR-STM (see Chapter 3), Chapter 6 explores the installation of an antenna for such purposes.

This chapter will provide an introduction of the fundamental concepts in simple terms. This chapter is intended to provide understanding for those less familiar with university-level physics. We will go over the Hamiltonian, also shown in Chapter 2 which is an equation that describes all the energy in the system, from which the quantum states can be found. In this particular case, the Hamiltonian will relate to atoms on a surface whose spin magnetic moment will be considered only. The origin of various potentials working on the atoms will be discussed, as well as how the atoms couple together to form chains. As also described in Chapter 3, an introduction on scanning tunneling microscopy (STM), through which the measurements take place, will be given. With a basic understanding of the context, an overview of the results in Chapter 4 will be provided, in which the lifetime of spin chains is extended by more than three orders of magnitude from milliseconds to seconds. The lifetime relates to the two lowest energy states, but for the higher energy states one can consider waves along the chain. Typically their lifetime is in the order of picoseconds. Chapter 5 will show how, using a Remote Detection scheme, these can still be measured. We will also go through a shallow description of electron spin resonance (ESR) through STM to understand why the antenna installation, as described in Chapter 6 is relevant.

1

1.2. FUNDAMENTALS OF STM

[Section 3.2] The Scanning Tunneling Microscope (STM), has been around since the 1980s, having received a Nobel prize in 1986 (see box). It consists of a needle (called *tip*) that hovers above a conducting surface (called *sample*) at a distance of a few ångström (Å = 0.1nm), comparable to the size of a single atom. At this distance, electrons are able to *tunnel* through the vacuum between tip and sample, a quantum mechanic effect that would be classically forbidden. This tunneling of electrons happens in both directions, but it can be guided by applying a voltage. As one applies a positive voltage on the tip, electrons in the tip will gain energy equal to $e \cdot V$, where e is the elementary charge and V is the voltage. This energy is thus in electronvolt, eV, the name of which describes its quantity. Electrons in the tip, now at a higher energy, can travel to the sample where these higher energy states are not occupied. On the other hand, even the conduction electrons in the sample with the most energy, those at the Fermi energy E_F, cannot find a unoccupied state in the tip; their conduction is therefore blocked. This results in a one-way stream of electrons upon application of a voltage. The rate at which these electrons tunnel is extremely dependent on the distance: every 100 pm distance increase, reduces the rate by a factor ten. It is clear that it provides tremendous resolution in height. By scanning the tip over the surface, one can build up a 2D-image pixel-by-pixel to get what is a called a topography. Such a topography is shown in Figure 3.1b.

Trivia

Gerd Binnig (b. 1947, Germany; left photo) and Heinrich Rohrer (b. 1933, Switzerland; right photo) shared half of the 1986 the Nobel Prize in Physics "for their design of the scanning tunneling microscope". The other half was awarded to Ernst Ruska (b. 1906, Germany) "for his fundamental work in electron optics, and for the design of the first electron microscope".

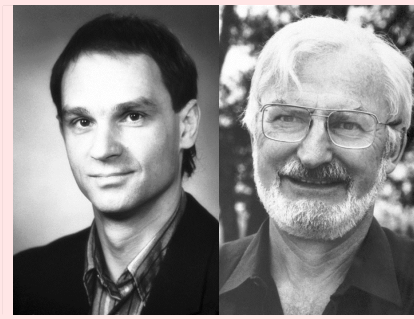

The former two were affiliated with IBM Zurich, Switzerland where, in 1981, they developed the first STM. Binnig went on to develop the AFM in 1985 at IBM Almaden (near San Francisco), which is also where ESR-STM was first discovered, in 2015.

[Section 3.3] But an STM is more than just a glorified microscope. It can also be used to study the electronic properties of the sample, such as the density of states. It does this by sweeping the voltage and looking at the resulting I,V-curve. The density of states, the distribution of states available for electrons as a function of energy, can be both continuous and discrete. This depends on whether one is probing bulk material or single atoms, respectively. In this thesis will explore the density of states of Fe chains on a single atomic Cu_2N layer on bulk Cu(100). This thesis will also present the density of states of Fe and

Ti on MgO/Ag, for the purpose of exploring the usage of ESR-STM, though it will not be the main focus.. Such atoms adsorbed on surfaces are called adatoms. The insulating MgO and Cu_2N layers serve three purposes: (1) it isolates the metal adatoms from the metal substrate allowing us to consider them individually rather than part of the bulk and (2) this decoupling also serves to reduce the flow of tunnelling electrons, reducing the disturbances they cause, and (3) it provides a surface on which we can place the atoms with some interesting features. These features include large magnetic anisotropy [section 2.1.1] and excellent coupling between neighbouring atoms [section 2.2], both essential ingredients for Chapter 4 and Chapter 5. Furthermore, in the case of the insulating layer MgO, it provides a polar surface which seems to be an essential ingredient for ESR [section 3.5]. We will go further into details on these concepts shortly.

1.3. FUNDAMENTALS OF ATOMIC SPIN CHAINS

Besides topographies and energy spectra, the STM can also be used to pick up and drop off individual atoms. This allows for the building of atomic structures, such as the ones shown in Figure 4.1 or the tripartite chain shown in Figure 5.1. There, Fe adatoms are placed on Cu_2N/Cu, where the characteristics of the insulating Cu_2N layer play a crucial role: the magnetic anisotropy and the surface-mediated coupling between neighbouring atoms. Here I will attempt to explain these in simple terms, as they, together with the magnetic field, fully describe the basic principles of those papers. So let us tackle these three concepts, in simplified terms.

In order to understand magnetic anisotropy, it is important to realize how electrons are tied to their atoms. They do so by following the Pauli Exclusion principle: this states that no two electrons can be in the same state at once. This happens because electrons are so-called fermions; particles with half-integer spin. This property spin is something all particles have - though it may also be equal to zero, as is the case for higgs bosons. The spin, or more accurately called spin angular momentum, is often imagined as the electron spinning around its own axis, which can have a defined axis. This quantity spin is quantized: it's exactly $S = {}^1/_2$ for all electrons. For any spin S, states emerge ranging from $-S, -S+1, -S+2, ..., S-1, S$. In this case, however, that range only permit two states: $m_s = -{}^1/_2$ and $m_s = {}^1/_2$, where m_s is the spin state. Similarly, an electron can have orbital angular momentum, associated with its orbit around the nucleus of an atom. While the rules are similar, they give rise to the electron shells you may be familiar with. Each shell (principal number n) has subshells (principal number l). It can often be instructive to look at only the outer shell, as it is often not fully filled, which gives rise to interesting physics. This is the case of Fe, where it has six electrons in its outer d-shell, which, with $l = 2$ allows for ten electrons total ($m_l = -2$, $m_l = -1$, $m_l = 0$, $m_l = 1$, $m_l = 2$ - times two for the two spin states). The six electrons arrange themselves such that we can regard Fe as an $S = 2$ system, thus having five spin states.

MAGNETIC ANISOTROPY

As mentioned before, one can imagine the spin to be around a certain axis. This is also the case for the $S = 2$ system. When Fe is placed on top of the Cu_2N surface, it gets incorporated into the molecular network and will experience electrostatic strain from its neighbouring atoms (as does any atom in a lattice). This strain may be different along different axes, causing an anisotropic (i.e. not isotropic, i.e. not the same in all directions) electrostatic force. In the particular case of Fe on $Cu_2N/Cu(100)$ on a so-called Cu-site, this has an effect on the spin, causing it to prefer one axis over another. If we pick the quantization axis (which is a mathematical choice) to be along the preferred axis (called *easy axis*), we can say that the spin is pointing along this axis to the biggest extent while in the ground state. In other words, this anisotropy causes the $m_s = -2$ and $m_s = +2$ states to be with the least amount of energy. The remaining states ($m_s = -1$, $m_s = 0$, $m_s = +1$) therefore have more energy. Since the anisotropy has an effect on the (magnetic) spin states, it is called magnetic anisotropy. Mathematically this can be described with a Hamiltonian as such:

$$H_{\text{anistropy}} = DS_z^2 + E(S_x^2 - S_y^2) \tag{1.1}$$

Here D is the easy-axis anisotropy term which defines the axis of the ground state, and E is the hard-plane anisotropy term which defines the energy difference between the other two axes. With $D < 0$, and $|E| < \frac{|D|}{3}$, it follows that $m_s = \pm 2$ gives the ground state: the state with the least amount of energy. To see this, simply fill in $m_s = \pm 2$. Note that both states are the ground state, and are therefore degenerate. In reality they are mixed, but we will get to that soon. For the case of Fe on a Cu-site on $Cu_2N/Cu(100)$ this means the ground states lie in an axis in-plane.

HEISENBERG EXCHANGE COUPLING

The way that the Fe atom lies in the Cu_2N molecular network defines not only the magnetic anisotropy, but also its so-called exchange coupling with neighbouring Fe atoms. Depending on the angle and distance between the atoms this coupling can favour neighbouring atoms to point parallel or anti-parallel. For a chain of atoms this can be mathematically described as:

$$H_{\text{Heisenberg}} = \sum_i J_i S^i \cdot S^{i+1} \tag{1.2}$$

Here J is the exchange coupling term, which favours parallel spins (ferromagnetism) for $J < 0$ and anti-parallel spins (antiferromagnetism) for $J > 0$. The i stands for the i^{th} atom in a chain and the sum is over all the atoms in a chain. As the coupling strength may be different between various neighbours (for example, if the spacing is different), the value J is pair-dependent. Throughout this work the most important coupling is that between Fe atoms with a distance of two lattice sites, where $J = -0.7$ meV. As a result of this we get two degenerate states that are comprised mostly of so-called Néel states, which (in the case of a chain of length three) are defined as $N_A = \{-2, +2, -2\}$ and $N_B = \{+2, -2, +2\}$, although they also contain a mixture of other states.

ZEEMAN SPLITTING

Finally, it is possible to turn on a magnetic field in most STMs, including ours. These fields reach several Teslas, similar to (or even more powerful than) an MRI scanner. In 1896-7 Zeeman discovered that magnetic fields can split certain states in energy. This was shown to be spin states. In our case this means that, even though according to the magnetic anistropy the states $m_s = -2$ and $m_s = +2$ should have the same energy, in the presence of an external magnetic field this degeneracy can be lifted. Mathematically this can be described as:

$$H_{\text{Zeeman}} = g\mu_B \mathbf{B} \cdot \mathbf{S} \tag{1.3}$$

Here g is the g-factor (approximately 2) and μ_B is the Bohr magneton, both constants. The external field $\mathbf{B}$ and the atom's spin $\mathbf{S}$ are both vectors, meaning, for example, a field along the $\hat{z}$-direction will result in S_z terms. Now also the degeneracy of a chain of length three is broken, but not that of even chains like length two or six.

Trivia

Pieter Zeeman (b. 1865, Netherlands; left photo) won the Nobel Prize in 1902 together with Hendrik Lorentz (b. 1853, Netherlands; right photo) for the discovery of the Zeeman effect, described as "in recognition of the extraordinary service they rendered by their researches into the influence of magnetism upon radiation phenomena".

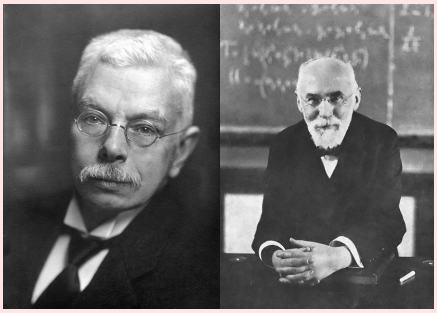

COMBING ALL INGREDIENTS

[Chapter 2] When we combine these three ingredients into a carefully selected chain of Fe atoms, we can describe this mathematically as simply the sum of the parts:

$$H_{\text{RemDet}} = \sum_i^N \left(g\mu_B \mathbf{B} \cdot \mathbf{S}_i + D S_{z,i}^2 + E(S_{x,i}^2 - S_{y,i}^2) \right) + \sum_i^{N-1} \left(J_i S_i \cdot S_{i+1} \right) \tag{1.4}$$

Here i runs over all the atoms, up to N atoms. In the case of measurements around the diabolic point, as in Chapter 4, we use a single chain, whereas for remote detection, as in Chapter 5, there are three chains that are weakly coupled. Let us start with understanding how this Hamiltonian affects a simple chain of three Fe atoms on $Cu_2N/Cu(100)$. For this, we will need to know the exact values of g, μ_B, D, E and J_i, which can be found in Appendix A.1, as well as $\mathbf{B}$. The value of $\mathbf{B}$ can be freely changed during the experiment, and as such will be stated each time. Referring to Figure 4.1a, we see how for a for

1

a pentamer, Fe_5, atoms B and D appear smaller. This can also be seen on the trimers, Fe_3, in Figure 5.1. This illustrates that the ground state is one that is defined mostly by the states $\{-2,+2,-2,+2,-2\}$ and $\{-2,+2,-2\}$, respectively. This is because in both situations there's an external magnetic field along the z-direction $\mathbf{B} = B\hat{z}$, which is defined as the easy-axis (so in-plane) of about 0.5 T.

SUPERPOSITIONS

Now it is important to realize the difference between classical approximations and the real quantum mechanics. It is true that in the presence of a strictly positive B_z the energy ground state is dominated by N_B, but the energy ground state consists of other spin states as well: it's a superposition of various spin states and also contains a small contribution of N_A. If we call the energy ground state ψ_0 and the first excited state ψ_1 we can say that (values are illustrative only):

$$\begin{aligned} \psi_0 &\approx 0.01N_A + 0.98N_B + ... \\ \psi_1 &\approx 0.98N_A + 0.01N_B + ... \end{aligned} \tag{1.5}$$

This can also be shown visually in a diagram, such as in Figure 2.5, which applies to a single atom, and so $N_A = \{+2\}$ and $N_B = \{-2\}$. In that diagram, ψ_0 is shown in red, ψ_1 is shown in blue and they are both composite of three states. We also see states with more energy (yellow and cyan). In order to go from one states to another, it is important that the spin-value of each state is at most 1 different: this is what a tunneling electron can supply by going from $+1/2$ to $-1/2$ or vice versa. This is called spin selectivity. Thus, still keeping an eye on Figure 2.5, with enough energy it is quite likely for the red state (mostly occupying $\{-2\}$) to go to the yellow state (mostly occupying $\{-1\}$), and then the black state (mostly occuping $\{0\}$) and then the cyan state (mostly occupying $\{+1\}$) and then the blue state (mostly occupying $\{+2\}$). However, to achieve this the system needs to be supplied enough energy to bridge the gap from the red state to the yellow state. This is considered a barrier, and so this kind of red-to-blue transition is called an over-the-barrier transition. This makes use of the dominant spin-state in each energy state. It is also possible to go directly from the red state to the blue state, but the likelihood of this is far smaller (with the numbers given in Equation 1.5 this would be about $0.01 \times 0.98 + 0.98 \times 0.01 \approx 0.02$, compared to likelihood of about 0.5 through the yellow state). This direct transition from red to blue is only possible because of the superposition effect and is called a through-the-barrier transition.

Depending on the measurement conditions (e.g. the bias voltage, temperature, magnetic field, current) the combination of over-the-barrier and through-the-barrier excitations leads to limited lifetimes of the states. The current understanding is that when we measure for example ψ_0, we actually measure mostly N_B as the electrons of the tunneling current do effectively do a spin-measurement. Hence we will refer to these lifetimes as spin lifetimes. When the voltage and temperature are low enough that there are basically no over-the-barrier excitations, the lifetime is limited by through-the-barrier excitations. Depending on the length of the chain, these can range from μs (for Fe_3) to

miliseconds (for Fe_6) to hundreds of miliseconds (for Fe_6) or longer (for longer chains). It is these lifetimes that we are interested in, in Chapter 4. It is the lifetime of the higher-lying states, the ones the atom or chain goes through during an over-the-barrier excitation (e.g. yellow in Figure 2.5), that we're interested in, in Chapter 5.

We have now discussed the important ingredients to understand the main takeaways from this thesis.

1.4. FUNDAMENTALS OF LIFETIME ENHANCEMENT NEAR A DIABOLIC POINT

In this section, the following main points will be made:

- Even in the absence of an external field, there is an energy difference between ψ_0 and ψ_1
- The signs in Equation 1.5 are wrong. Upon proper application this will lead to symmetric and anti-symmetric states.
- When increasing $B_x = \mathbf{B}\cdot\hat{x}$ there will be crossing at B_{diab} where the energy difference between the two is minimal. If $B_z = \mathbf{B}\cdot\hat{z} = 0$ this energy difference is zero and this is called a diabolic point.
- For $B_x < B_{\text{diab}}$ the symmetric state has the least energy, for $B_x > B_{\text{diab}}$ the anti-symmetric state has the lowest energy
- Around the diabolic point the superposition effect gets reduces, which reduces through-the-barrier transitions, increasing the spin lifetime of the ground state and first excited state.

The description following Equation 1.2 tells us that the states are mixed, which is also in the superposition of Equation 1.5. This is because the term $E(S_x^2 - S_y^2)$ can be rewritten as $\frac{E}{2}(S_+^2 + S_-^2)$, where S_+ is the spin raising operator and S_- is the spin lowering operator. With these terms being squared, the states that are two spin units apart are mixed: $\{-2, 0, +2\}$ and $\{-1, +1\}$. As a result, Figure 2.3 shows that ψ_0 (red) now has a contribution in $m_s = 0$. Not only that, but Table 2.2 shows that ψ_0 has positive signs in both $m_s = -2$ and $m_s = +2$, whereas ψ_1 has a negative sign for $m_s = -2$. Hence we call ψ_0 symmetric and ψ_1 anti-symmetric. The same table shows that there is already an energy difference between the two states, as a result from this symmetry. Thus the values of Equation 1.5 were only used for illustrative purposes.

It turns out that one can change the energy related to this symmetry by increasing B_x. This is shown in Figure 2.8c, where the blue curve shows the energy difference between ψ_0 and ψ_1 for a single atom. We see that this goes to zero around 9.5 T, which is called the diabolic point B_{diab}. Beyond the diabolic point the anti-symmetric state has less energy and is therefor the ground state. This means that that ground state's contribution of $N_B = \{m_s = -2\}$ needs to change from negative to positive. Exactly at the crossing this

contribution would then have to be zero exactly. Then $\psi_0 \approx N_B$ and $\psi_1 \approx N_A$. Now it is practically impossible to apply $B_x = B_{\text{diab}}$ exactly. But what happens when instead of a crossing, we make it an avoided crossing, like in Figure 2.11d? We can do this by associating N_A and N_B with different energy through applying B_z, i.e. Zeeman energy.

When we do this, there is a transition regime where ψ_0 smoothly changed from symmetric to anti-symmetric. This is important, because now the superposition effect, and hence the through-the-barrier transitions and hence the lifetimes changes smoothly. This is shown in panel b of the same figure: orange and pink show the spin lifetime of ψ_0 and ψ_1, and the green curve shows a measure for the likelihood of transitions. We see that around diabolic point the likelihood drops and the lifetime of both states go up. The resulting peak in the lifetime is something we can measure and have measured (see all figures of Chapter 4).

Now as to why is this point called a diabolic point, this has to do with the shape of the energy diagram when plotting this against B_x and B_z. This is shown in Figure 2.13 and is reminiscent of the toy diabolo. Notice that previous energy plots showed the difference between ψ_0 and ψ_1, this plot shows both ψ_0 (in orange) and ψ_1 (in pink).

Through further studies it is found that an even chain, Fe_6, which is not supposed to have any energy difference between N_A and N_B, still has some difference in energy between them. We relate this to the g-factor of Equation 1.4 being different for each atom.

1.5. FUNDAMENTALS OF REMOTE DETECTION

In this section, the following main points will be made:

- Spin excitations can result in spin waves called magnons, with a lifetime about 10 ps.
- Magnons move across the chain and will deviate the spin-value of atoms from their ground state value.
- A sensor can be placed at the back of a chain to record whether a wave reaches the end of the chain.
- The sensors is based on Fe_8 which normally has two ground states that are degenerate.
- The sensor is prepared such that when an incoming wave lifts the degeneracy, the sensor is in an excited state. If the sensor switches states (by going to the ground state) it is a sign of incoming wave.
- By repetition of the experiment, enough statistical evidence can be found to support the claim that the sensor reads the incoming waves, and thus information about the waves can be determined.

When a state is not a pure energy state, the phase(s) between the contributions will oscillate: in effect the state will cycle through the various components. This is true also for $\{-2,+2,-2\}$ and in fact, the cycling between ψ_0 and ψ_1 (and the other energy states that contain this spin state) can be seen as the through-the-barrier transition. For other spin states, other interesting phenomena happen.

When a tunnel electron goes from the tip to the adatom to the substrate, it does a spin-measurement on the adatom. During this it can either keep its spin or exchange it, resulting in the aforementioned spin selectivity. Imagine a tunneling electron reaching the first atom of a trimer, Fe_3, in its ground state. The spin-measurement will result in $\{-2,+2,-2\}$ and so the spin exchange would result in $\{-1,+2,-2\}$. When this latter spin state cycles through its energy states it effectively sets of a wave along the chain, resulting some time later in a significant contribution in $\{-2,+2,-1\}$: the excitation spreads along the chain. This takes about 30 ps, and can be seen in Figure 5.7. However, other electrons that tunnel (either from the tip or from the bath of electrons at the substrate) will decay this excitation in about 7 ps. So only very few of these excitations, or magnons, make it from the first atom to the third atom. Nonetheless, the ones that do make will result in the third atom's spin-value deviating from its ground state value. Since our STM tip cannot initiate an excitation in the first atom and move to the third atom within 30 ps (it would easily take 1 ms), we would need some kind of sensor that measures this deviation of spin-value and records it, for the tip to check post-excitation.

This is where the sensor, shown in Figure 5.1, comes in. Panel a shows how the **in**put chain is a trimer, the **out**put chain is an octomer, Fe_8, and a **reset** is another trimer. The trimers will have their ground state dominated by $\{-2,+2,-2\}$, while the octomer has two degenerate ground states: N_A and N_B. We define N_A such that the atom closest to the input trimer is $m_s = -2$, as indicated by the red atom. Since the three chains are spaced such that there is a weak coupling between the chains that favours like spins, the sensor's N_A state will be happy on the input side. However on the reset side, the last atom of the octomer will be $m_s = +2$, resulting in an unhappy coupling with the reset lead. The octomer is said to be frustrated: even when it switches to N_B there will be one side happy and one side unhappy. Notice that N_A and N_B are the spin states, but the energy states they are related to, ψ_A and ψ_B, follow the same logic, since their composition is dominated by N_A and N_B, respectively.

But what happens when the closest atom of the input trimer, atom A, is no longer has dominated by $m_s = -2$ due to an incoming magnon? In that case the happy coupling with the input lead is broken and the system is out of balance: it is now energetically more favourable for the octomer to switch to N_B. Although the lifetime of N_A and N_B is still in the order of seconds, there is now a significant difference between the lifetime of both, resulting on N_B being much more favoured. Hence a complete measurement cycle would consist of preparing the octomer in N_A, initiating an excitation in the farthest atom of the input chain, atom C, and then checking of the octomer changed to N_B. Repeat this many times, and do the same starting from N_B instead, and statistically speaking the states starting from N_A are more likely to have switched to N_B than vice

versa.

Experimental results confirm this, as shown in the other figures of Chapter 5. The excitation leading to a switch from N_A to N_B is described by the switching probability P_H: a switch away from happy coupling to the input trimer. An excitation leading to a switch from N_B to N_A is described by the switching probability P_U: a switch away from unhappy coupling to the input trimer. The value P_U should be low as the magnon brings the outlead from a degenerate state to a ground state: a switch to N_A implies an excitation - which is less likely.

We can now find the switching rates in various experimental setup, for example with different chain sizes, or initiating the excitation on different atoms. We can then compare these results with theoretical models to corroborate the models, which is done success.

1.6. FUNDAMENTALS OF ESR

So far we have discussed lifetimes of ψ_0 and ψ_1 for chains in the case of the lifetime enhancement through a diabolic point, and the lifetime and movement of excitations on chains beyond ψ_1 in the case of remote detection. Now we will focus on a single atom, and for simplicity will take $S = {}^1/_2$, leaving only two states: $m_s = -{}^1/_2$ and $m_s = +{}^1/_2$. Since the magnetic anisotropy terms work on square of the spin operators S_x, S_z and S_z, they have no effect on this system (after all, $(+{}^1/_2)^2 = (-{}^1/_2)^2$). Hence only the Zeeman energy is relevant, which for a few Tesla amounts to a few hundred μeV.

[Section 3.5] The static magnetic field not only yields a Zeeman energy, but also lets the atom's spin precess around the axis of the field, leading to what is known as Larmor precession with its frequency being called the Larmor frequency, which is proportional to the Zeeman energy following $E = hf$, where h is the Planck constant. This field we define as the $\hat{z}$-axis and so one can imagine this similar to Delft being spun around the axis of the Earth. The idea of ESR is to apply an oscillating magnetic field perpendicular to the static field at the Larmor frequency. This would result in a secondary Larmor precession, called a Rabi rotation, now about an axis through the equator: as if Delft is precessing from North to South. With the static field inducing energy along the $\hat{z}$-direction (North-South), the spin is essential precessing along its two states $m_s = -2$ and $m_s = +2$. The frequency of this oscillation, which is a function of the amplitude of the oscillating field, is called a Rabi flop rate.

Trivia

Electron Spin Resonance (ESR) is conceptually similar to Nuclear Magnetic Resonance (NMR), the latter of which was first discovered by Isidor Rabi (b. 1898, Austria-Hungary, now Poland) in 1938, leading to a Nobel Prize in 1944 "for his resonance method for recording the magnetic properties of atomic nuclei". In that same year Yevgeny Zavoisky (b. 1907, Russia, now Ukraine) discovered ESR.

A recent development is the application of ESR on single atoms by means of STM. So how does one get such an oscillating magnetic field? While most STMs are equipped with a large superconducting electromagnet, such equipment is only suited for static fields, not oscillating ones. The way ESR-STM has been proven to work is by applying an oscillating voltage to the tip-sample junction - either through the cabling going to the tip or through an antenna nearby. We will call this the driving voltage. In the case of a single atomic layer (monolayer) of MgO on Ag, the monolayer starts to oscillate along with this driving voltage (or rather driving electric field). Most atoms on the surface will do the same, including any atom under our STM tip. Through means of a magnetic field gradient induced by a neighbouing atom, either on the surface or a magnetic apex atom on the tip, the probed atoms experiences an oscillating field as it moves up and down through this gradient.

The biggest hurdle in this is to apply an oscillating voltage at the right frequency (radio frequencies (RF): about 10-20GHz or higher) of significant amplitude. Most cabling is not suitable for this, and so specific cabling needs to be installed either directly to the tip or to a nearby antenna. Chapter 6 described the installation of an antenna for this purpose and also shows some ESR-STM results.

The advantage of ESR-STM is twofold: First, because the driving mechanism is extremely sensitive to the applied frequency, up to a few tens of MHz, there is extremely energy resolution: 50 μeV. This is much better than the accuracy of 1 meV that is typically obtained through the I,V-curve. Secondly: by performing Rabi oscillations, there is essentially a very coherent control of the spin. This means that the spin can be precisely rotated and prepared into states, which is important for quantum computing, among other things.

2

THEORY

In this chapter we will discuss the theoretical model which underlies the experiments performed throughout this thesis. We will take a bottom-up approach where, over the course of several steps, different terms in our spin chain Hamiltonian will be turned on. For each term we will discuss its origins, and shows the effect of turning it on by looking at the energy diagram and a simulated IETS measurement. Along the way, we will explore state switching, and how it relates to lifetimes of two (nearly degenerate) states. We will see how under certain conditions a diabolic point can be measured. This is an energy crossing in parameter space with profound effects on the lifetime. These lifetimes can be measured through telegraphic noise as is done in Chapter 4. We will see that these diabolic points exist both for single atoms and atomic spin chains. For the latter we will also look into the propagation of excitations called magnons. For this we will use the time-dependent Schrödinger equation. The magnons will be presented as non-pure energy eigenstates, and so their phase will oscillate until they decay, which will be considered to happen after a set time. The results in this chapter are specifically tailored towards Fe on $Cu_2N/Cu(100)$, although most of the lessons are univerisally applicable. Throughout this chapter the terms "mixing" and "mixed state" will be used. This refers to superimposed classical states, and do not refer to ensemble measurements. Many of the calculations in this thesis are based on on code written during a MSc thesis project of Jorn Rietveld.

Our spin chain Hamiltonian can be described in the most general form for this thesis as:

$$H_0 = \sum_i^N \left(g_i \mu_B \mathbf{B}_i \cdot \mathbf{S}_i + D_i S_{z,i}^2 + E_i (S_{x,i}^2 - S_{y,i}^2) \right) + \sum_i^{N-1} \left(J_i S_i \cdot S_{i+1} \right) \tag{2.1}$$

Here g_i is the g-factor on atom i, $\mu_B = \frac{e\hbar}{2m_e}$ is the Bohr magneton, where e is the electron charge, $\hbar$ is the reduced Planck's constant and m_e is the electron rest mass. $\mathbf{B}_i$ is the total magnetic field on atom i, $\mathbf{S}_i$ is the spin of atom i, D_i is the easy-axis magnetic

anisotropy term on atom i, E_i is the hard-plane magnetic anisotropy term on atom i and J_i is the total coupling strength between atoms i and $i+1$. We will now start from the simplest Hamiltonian and work our way towards H_0. The first step is the trivial case of $H = 0$ in which nothing happens. So let's quickly move on to the next step.

2

2.1. ATOMIC SPIN ON A SURFACE

2.1.1. UNIAXIAL MAGNETIC ANISOTROPY

An atom placed on a surface, an adatom, may cause a rearrangement of the local electronic structure [1]. Likewise, the local structure will certainly affect the electrons of the adatom. This, together with spin-orbit coupling, may lead to magnetic anisotropy where the adatom's spin S (as found through, for example, Hund's rules) will prefer to align along a certain axis, or the exact opposite: prefers to align away from a certain axis. In the former case we speak of an easy axis, in the latter case we speak of an easy plane (or hard axis). This can be mathematically described as:

$$H_{\mathrm{D}} = DS_z^2 \tag{2.2}$$

Here D is known as the magnetic anisotropy constant and is purely an observational constant, with the origin lying in spin-orbit coupling and crystal field [2]. For the case of $S = 1/2$ the value of D is arbitrary, since $S_\alpha^2 = I$ the identity matrix where $\alpha \in \{x, y, z\}$, but for larger values of S the energy diagram clearly shows which values of D give an easy axis and which give a hard axis, see Figure 2.1. Here for two situations the energy diagram is given. The colors indicate the different states, from red, blue, yellow, cyan to black in order of increasing energy. As we will see later on, the opacity of the circles indicate the contribution to each state. In this case, the circles are at their maximum opacity indicating pure states.

For $D > 0$ it costs energy to lie along the z-axis, so the ground state will be $m_s = 0$, lying somewhere in the x,y-plane. For $D < 0$, the ground state is degenerate among $m_s = -S$ and $m_s = +S$, with an energy barrier in between. Is this enough to allow for state switching? Since most of this thesis pertains to Fe on Cu-sites on Cu_2N/Cu(100), let us consider specifically the case where $S = 2$, $D = -1.87$ meV. This value is used in Chapter 5 and lies in between other literature values of -1.55 [1][3] and -2.1 [4]. Table 2.1 shows the energy distribution and spin-state distribution of the five states, for the given situation.

Table 2.1: State decomposition for Equation 2.2, with $D = -1.87$ meV.

	$m_s = -2$	$m_s = -1$	$m_s = 0$	$m_s = +1$	$m_s = +2$	Energy (meV)
ψ_0	1					0
ψ_1					1	0
ψ_2				1		5.61
ψ_3		1				5.61
ψ_4			1			7.48

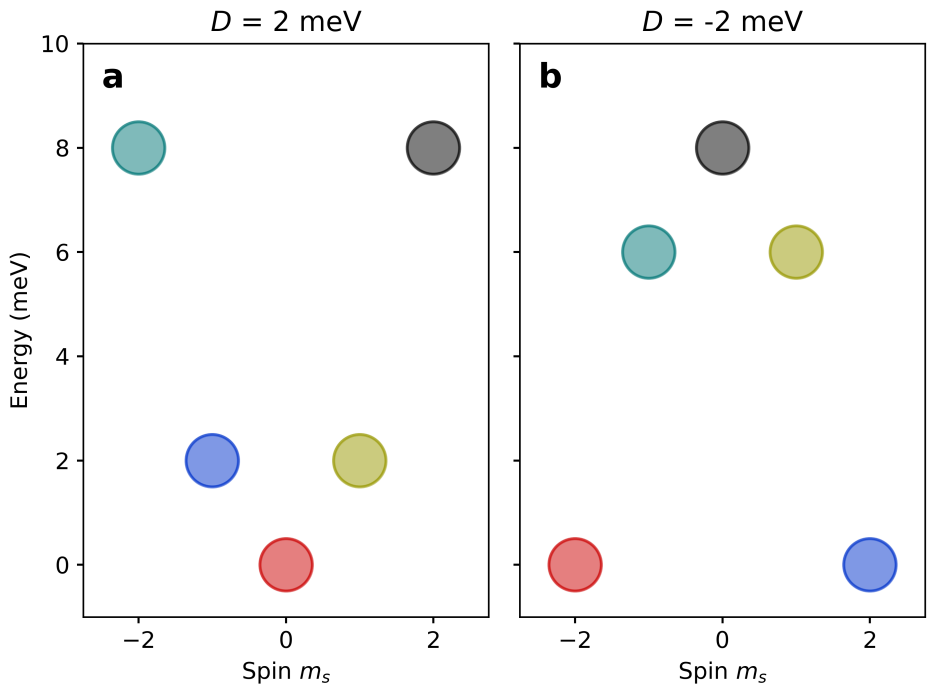

Figure 2.1: Energy diagram for Equation 2.2. **(a)** Energy diagram for all five states with $N = 1$, $S = 2$, $D = 2$ meV. **(b)** Same as **a**, but for $D = -2$ meV. Colors from lowest to highest energy states are red, blue, yellow, cyan and black, respectively.

The ground states are degenerate at 0 meV with pure spin-states $\psi_0 = |S_z = -2\rangle$ and $\psi_1 = |m_s = +2\rangle$. The next two states, also degenerate at $E_2 = E_3 = 3D$, consist of pure spin-states $\psi_2 = |m_s = -1\rangle$ and $\psi_3 = |m_s = +1\rangle$. Finally, the fifth state consists of the pure spin-state $\psi_4 = |m_s = 0\rangle$ at $E_4 = 4D$. While the results seem almost trivial, it provides a good backbone for further adjustments to the Hamiltonian.

TRANSITION RATES

Before we introduce more terms into the Hamiltonian, we will take a look at transition rates between states. To this end we will consider two separate things, although they are both based on the same rate equations, which will be introduced shortly. We will consider inelastic electron tunneling spectroscopy (IETS) simulations on the one hand, and lifetime simulations on the other hand. The corresponding experimental methods are discussed in Section 3.3 for IETS and Chapter 4 for lifetime measurements. In this chapter we will consider the following: (1) simulated IETS measurements for various parameters and (2) the expected lifetime of the ground state and the first excited state, together with a so-called scattering amplitude and the energy difference between these two states $\Delta E_{0,1}$.

Rate equations, also known as Pauli master equations, are based on Fermi's golden rule and have the following form:

$$\frac{dn_i(t)}{dt} = \sum_j r_{ij} n_j(t) - r_{ji} n_i(t) \tag{2.3}$$

The rates r_{ji} describe the transitions from eigenstate $|\psi_i\rangle$ to eigenstate $|\psi_j\rangle$. This relates the change of occupation $n_i(t)$ of state i over time to the rates in and out of state $|\psi_i\rangle$. These rates include inelastic and elastic transitions (i.e. $|\psi_i\rangle \rightarrow |\psi_i\rangle$). We will assume the system to be in a steady state such that $\frac{dn_i(t)}{dt} = 0$. The rates are a summation of four contributions: $r_{ji} = r_{ji}^{s\rightarrow t} + r_{ji}^{s\rightarrow s} + r_{ji}^{t\rightarrow s} + r_{ji}^{t\rightarrow t}$ where t and s denote the tip and sample, respectively. The rate $r_{ji}^{a\rightarrow b}$ is the number of transitions from $|\psi_i\rangle$ to $|\psi_j\rangle$ per second due to electrons traveling from electrode a, via the adatom to electrode b. Tip-tip interactions are considered negligible, so only the first three are considered. Since during each transition, an electron needs to leave its original lead, an electron-hole pair is created locally. The adatom is coupled to the electron bath through exchange coupling. During a tunnel process, an electron-hole pair is created, where the electron hops on to the adatom in a co-tunneling process, leading to a second order perturbation model, described through Kondo exchange coupling, with coupling strength J^2 between electrode and adatom. In order to account for the energy difference between two adatom states $\Delta E_{i,j}$, the tunnel electrons must have enough energy through an applied bias voltage V_{bias} and thermal broadening:

$$r_{ji}^{a\rightarrow b} = \frac{\tilde{G}}{e^2} \int_{-\infty}^{\infty} F(E)[1 - F(E + e\tilde{V} - E_i + E_j)] \cdot P_{ji}^{a\rightarrow b} dE \tag{2.4}$$

Here the terms with tilde are defined differently depending on the electrodes. For $s \leftrightarrow t$, $\tilde{G} = G$ where G is the conductance between the tip and e is the electron charge. Meanwhile for $s \rightarrow s$, $\tilde{G} = G_S$ which is the conductance to the substrate and $\tilde{V} = 0$ as this does not depend on bias voltage. $F(E)$ is the Fermi distribution, dependent on temperature, E_i and E_j are the energies of states $|\psi_i\rangle$ and $|\psi_j\rangle$, $\tilde{V} = V_{\text{bias}}$ and $P_{ji}^{a\rightarrow b}$ is the spin part of the equation. After all, the total spin the system has to be conserved. Defining $m_s^e = {}^1/_2$ as $|\uparrow\rangle$ and $m_s^e = -{}^1/_2$ as $|\downarrow\rangle$, there are four possibilities in terms of spin: $|\uparrow\rangle \rightarrow |\uparrow\rangle$, $|\uparrow\rangle \rightarrow |\downarrow\rangle$, $|\downarrow\rangle \rightarrow |\uparrow\rangle$ and $|\downarrow\rangle \rightarrow |\downarrow\rangle$. The first and last preserve the spin of the electron, whereas the other two allow for a flip-flop between the electron and the system. The tip may be spin-polarized, and so:

$$P_{ji}^{a\rightarrow b} = \frac{1}{P_0} \sum_{\sigma,\sigma'} Y(\psi_j, \sigma', \psi_i, \sigma)\tilde{\eta} \tag{2.5}$$

Here $\tilde{\eta} = \frac{1}{2} + \eta\sigma$ for $s \rightarrow t$, $\tilde{\eta} = \frac{1}{2} + \eta\sigma'$ for $t \rightarrow s$ and $\tilde{\eta} = 1$ for $s \rightarrow s$. The term η is the tip's polarization between -1 and 1. The terms σ and σ' are the spin of the incoming and outgoing electron, respectively. The normalization factor $P_0 = \sum_\sigma Y(\psi_0, \sigma, \psi_0, \sigma)(\frac{1}{2} + \eta\sigma)$ so that the total transition is 1. The transition intensity function Y defines how likely a tunnel electron is able to cause a state switch through one of the four previously mentioned possibilities and can be calculated as such:

$$
\begin{aligned}
Y(\psi_j,\sigma',\psi_i,\sigma) &= |\langle\psi_j,\sigma'|S_x\sigma_x + S_y\sigma_y + S_z\sigma_z + u|\psi_i,\sigma\rangle|^2 \\
&= |\langle\psi_j,\sigma'|\frac{S_+\sigma_- + S_-\sigma_+}{2} + S_z\sigma_z + u|\psi_i,\sigma\rangle|^2
\end{aligned}
\tag{2.6}
$$

Here S_α and σ_α ($\alpha = \{x,y,z\}$) are the spin operators acting on the spin of the system and electron, respectively. The term u, being a constant, only affects the transition rate when $i = j$ and accounts for elastic tunneling independent of spin. For more information on these rate equations, see [5–8]. We will newly introduce the following term known as the scattering amplitude:

$$
P_{i,j} = P_0 \cdot P_{ji}^{s\rightarrow s} = \sum_{\sigma,\sigma'} Y(\psi_j,\sigma',\psi_i,\sigma) \tag{2.7}
$$

Here $u = 0$ for $P_{ji}^{s\rightarrow s}$. This value considers merely whether a switch between two states ψ_i and ψ_j is possible due a tunnel electron following one of the previously four mentioned possibilities. This value is easy to calculate based on the Hamiltonian and its solutions and does not depend on specifics of the tip. We use $P_{0,1}$, together with the energy difference $\Delta E_{0,1}$, to understand the lifetime the ground state and the first excited state. Note that $P_{0,1} = P_{1,0}$.

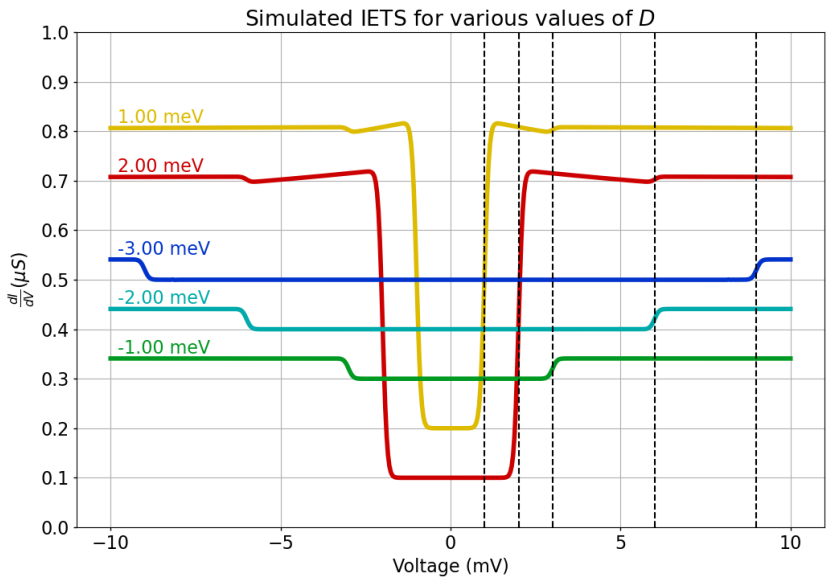

Figure 2.2: Simulated IETS for Equation 2.2. Dashed lines at 1 meV, 2 meV, 3 meV, 6 meV and 9 meV. Consecutive plots (red, yellow, green, cyan, blue) are offset by 0.1μS. $T = 0.5$ K. $u = 0.5$, $b_0 = 0$, $G = 0.1\mu$S and $G_S = 3.1\mu$S

Figure 2.2 shows the simulations of IETS measurements, for various values of D, based on equation 2.2, at a temperature of $T = 0.5K$, representative of experimental conditions. The tip is assumed to be over the adatom at a conductance of $G = 0.1\mu$S (which corresponds to 100 pA at 10 mV). The conductance of the adatom with the bath is taken at $G_S = 3.1$ μS [4]. Finally, the term $u = 0.5$, which is tells us how many of the tunneling electrons interact with the system and $b_0 = 0$ to let all electrons interact. Each IETS simulation will have these parameters unless stated otherwise, and are hence omitted in future figures. For $D > 0$ we find a changes in the IETS curves at $V_{\text{bias}} = 1D$ and at $3D$. In the former case our tunneling electrons have enough energy to excite the adatom's spin from $m_s = 0$ to $m_s = \pm 1$. Then as the tunnel bias increases the transition rate goes down slightly. This is not due to third order interactions that some simulations include [8], since these are not implemented. Instead, this is due to saturation where extra electrons are not able to excite the system faster than the system has time to relax, until we reach $3D$ where a second electron is able to excite the system from $m_s = \pm 1$ to $m_s = \pm 2$. Notice that at $4D$ nothing happens: a single electron is never able to provide $\Delta s = \pm 2$. Likewise, for $D < 0$ we find symmetric steps at exactly $eV = \pm 3D$, akin to [9]. However, it is important to realize that this is the *only* step in the simulated IETS. Unlike before, both $\psi_0 \rightarrow \psi_3$ and $\psi_3 \rightarrow \psi_4$ are accessible at the same bias voltage, so no second step appears. For the remainder of this thesis we will assume $D = -1.87$ meV.

One can ask the question whether the system resides in ψ_0 or ψ_1 as they are both degenerate. The truth that the system resides in both states, but in a classical sense: the Boltzmann distribution indeed determines both states should occur with equal probability. However, since the energy eigenstates are pure spin states that have $\Delta m_s > 1$ the scattering amplitude $P_{0,1} = 0$ and so the lifetime of both states, in the absence of any excitation, is infinite. Only through interaction (by having $T > 0$ or $eV_{\text{bias}} > \Delta E_{0,2}$) can the system switch between the two states. In such a case, one would indeed expect an equal distribution across the time-ensemble. For low temperature and bias voltage we can consider these states stable. One possible way to overcome this stability, which we will see once we introduce the transverse magnetic anisotropy term E, is by having the energy eigenstates ψ_0 and ψ_1 become superpositions of spin states: these will be called mixed states. For such mixed spin states, it is possible to quantum tunnel between two states that share components in the same spin state, as $P_{0,1} > 0$. In order for this to work a measurement is required. One can imagine this as collapsing the energy eigenstate ψ_0 to a spinstate and subsequently relaxing this excited virtual state to another energy eigenstate ψ_1. Any passing electron can do this, be it from the substrate bath or the tunneling electrons. Such a measurement maintains the electron's spin. However, it is also possible for the measuring electron to exchange its spin with the system, which is known as a flip-flop.

Having introduced D, we can now write a small list of conclusions:

Summary

- For $D < 0$ and $S = 2$ the states ψ_0 and ψ_1 revolve around $m_s = \pm 2$.
- In the absence of mixing terms and with $|m_s^{\psi_0} - m_s^{\psi_1}| > 1$ the scattering amplitude $P_{0,1} = 0$ and so without going through intermediate states, the lifetimes of ψ_0 and ψ_1 approach infinity.

2.1.2. TRANSVERSE MAGNETIC ANISOTROPY

The uniaxial magnetic anisotropy assumes a single axis to be (dis)favoured. This typically happens when an adatom is on a four-fold symmetric site, such as Fe on an O-site on MgO [9], or Fe on the N-site on Cu_2N [10], although here quadruple terms are also of importance. There are also plenty of systems where there is a relative preference between the two remaining axes such Mn on Cu-site on Cu_2N [5], our proto-system Fe on Cu_2N [1] or single molecular magnets (SSM) such as those with Fe_4 [11], Fe_8 [12] or Mn_12 [13]. For this we introduce the Transverse Magnetic Anisotropy term E, which gives the energy difference between alignment along the x-axis and y-axis of the system. The total Hamiltonian will then look like:

$$H_{\mathrm{DE}} = DS_z^2 + E(S_x^2 - S_y^2) \tag{2.8}$$

In the case of Fe on a Cu-site on Cu_2N, the atoms experiences the three axes quite differently: along its z-axis (in-plane) there are N atoms, along its x-axis (in-plane) there are vacancies and along the y-axis (out-of-plane) there is a clear boundary. This results in $E = 0.31$ meV. The resulting energy eigenstates are now superpositions of spinstates, as shown in Table 2.2. Compare this with [1]. Note that if $E < 0$ or $E > |D/3|$, the axes should be redefined.

Table 2.2: State decomposition for Equation 2.8, with $D = -1.87$ meV and $E = 0.31$ meV.

	$m_s = -2$	$m_s = -1$	$m_s = 0$	$m_s = +1$	$m_s = +2$	Energy (meV)
ψ_0	0.700		-0.139		0.700	0
ψ_1	-0.707				0.707	0.15
ψ_2		0.707		-0.707		4.83
ψ_3		0.707		0.707		6.69
ψ_4	-0.099		-0.990		-0.099	7.78

The introduction of the transverse term has some profound effects: it not only mixes the states, but also removes the degeneracy of the two lowest energy eigenstates. The

exact value of $\Delta E_{0,1}$, the excitation energy of ψ_1, has no known useful analytical expression. The mixing of states ψ_0 and ψ_1 is possible because $E(S_x^2 - S_y^2) = \frac{E}{2}(S_+^2 + S_-^2)$: any two spin-states that are a multiple of two S_+ or S_- operators away will mix. This causes $m_s = \{-2, 0, +2\}$ and $m_s = \{-1, +1\}$ to mutually mix. In fact, when picking E arbitrarily small, but finite, states ψ_0 and ψ_1 are superposed as shown - with the value of E only determining the contribution of $m_s = 0$ to ψ_0. Since there is now energy to be gained in the x,y-plane, this term determines the energy difference between the two states. Notice that ψ_0 and ψ_1 can be seen as an even and odd combinations of $m_s = -2$ and $m_s = +2$, respectively. In fact, let's already name these symmetric and anti-symmetric combinations as $N_+ \approx N_A + N_B$ and $N_- \approx N_A - N_B$, respectively. Here $N_A = |+2\rangle$ and $N_B = |-2\rangle$ are defined as fully polarized spin states. The approximation is not an equal sign due to a contribution of $m_s = 0$ in N_+ and the lack of coefficients. For an $S = 1$ system the ground state and first excited state *are* exactly symmetric and anti-symmetric [14].

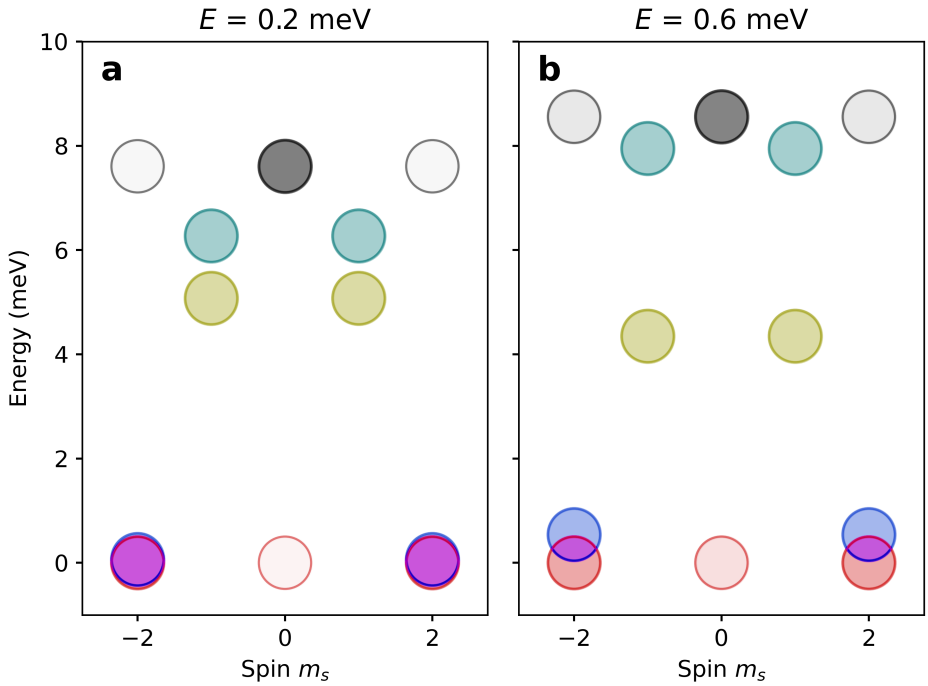

Figure 2.3: Energy diagram for Equation 2.8. **(a)** Energy diagram for all five states of $N = 1$, $S = 2$, $D = -1.87$ meV, $E = 0.2$ meV **(b)** Same as **a**, but for $E = 0.6$ meV. Color coding same as Figure 2.1. Opacity is a measure of state contribution. Blended colors (such as purple) indicate contribution is shared among different energy eigenstates that are close in energy.

This superposing is also shown in Figure 2.3. Notice that since two energy eigenstates can now both have contributions in the same m_s-state, the circles' opacity is a measure for the amplitude of this contribution. We see that increasing E increases the contri-

bution of $m_s = 0$ in $\psi_0 = N_+$, increasing $\Delta E_{0,1}$. As $|\langle 0|\psi_0\rangle|$ increases, $|\langle 0|\psi_4\rangle|$ naturally decreases and instead ψ_4 occupies more $m_s = \pm 2$. A similar symmetric/anti-symmetric behaviour happens with ψ_2 and ψ_3, with an even stronger effect on the energy difference between the two.

TRANSITION RATES

As before, we can take a look at simulated IETS measurements, shown in Figure 2.4a. Included is the case of $E = 0.30$ meV, which can be compared with [1]. Now there is a finite scattering amplitude between ψ_0 and ψ_1 and hence transitions between them are not forbidden due to selection rules. For very small values of E, the energy difference between the two states is so small, that given $T = 0.5$ K, we are always able to excite between these two states. For larger values of E, this is not the case, and so an additional step appears indicating the required voltage for these excitations to occur. Additional steps can be found at the other dashed lines, which correspond to the excitation energies, as also shown in Table 2.2.

Now we can also consider the lifetimes of these two states as measured by means of an STM-tip. The lifetime of ψ_0 is plotted in Figure 2.4b, together with the scattering amplitude and (c) energy difference between the two states. We can see that the scattering amplitude $P_{0,1}$ alone is not indicative of the expected lifetime: it does have not a kink around $E = 0.25$ meV, separating the parameter space into a slowly increasing lifetime and a fast increasing lifetime regions. Instead, this kink is related to the energy difference. With $T = 0.1$ K and $V_{\text{bias}} = 0.1$ mV (corresponding energy is shown as a dashed line in subfigure (c)) the onset of the fast increasing lifetime is when the system, using the tunneling electrons, can no longer be excited $\psi_0 \rightarrow \psi_1$ and the lifetimes goes towards infinity (limited only by the tail of the Boltzmann distribution). The choice of T and V_{bias} is not typical, but chosen to illustrate the point that switches are only possible if both the scattering amplitude and energy permit. Notice that the lifetime of ψ_1 is fairly constant: it's always possible to relax to ψ_0.

Summary

- The presence of mixing terms (such as E) allows for under-the-barrier switches between $\psi_0 = N_+$ and $\psi_1 = N_-$.
- Mixing terms can increase $\Delta E_{0,1}$.
- Switches are not only limited by scattering amplitude $P_{0,1}$, but also by whether there is available energy to bridge $\Delta E_{0,1}$.

2.1.3. LONGITUDINAL MAGNETIC FIELD

The next term we will turn on is the Zeeman energy: an additional energy due to a magnetic moment in a magnetic field. The orbital momentum and spin-orbit coupling is

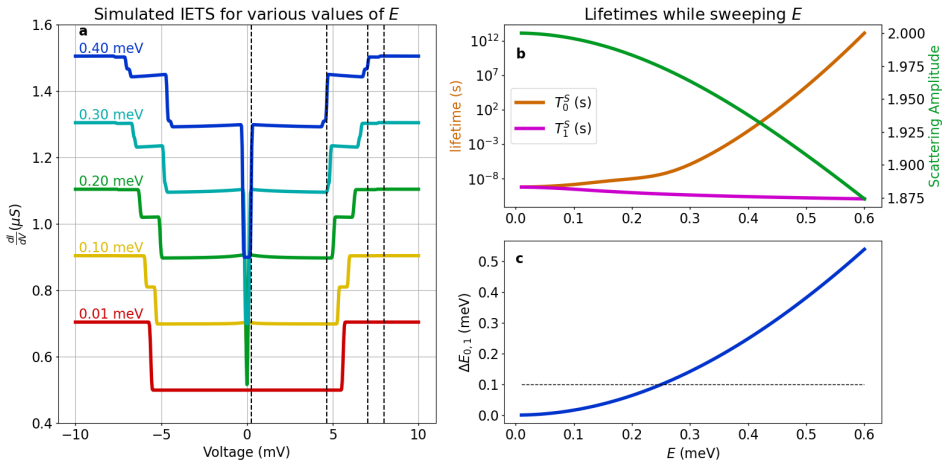

Figure 2.4: Simulated IETS and lifetime for Equation 2.8. **(a)** Simulated IETS measurements. Dashed lines at 0.25 meV, 4.66 meV, 7.06 meV and 7.98 meV corresponding to the steps for $E = 0.40$ meV. Consecutive plots (red, yellow, green, cyan, blue) are offset by 0.2μS. **(b)** Scattering amplitude (green) and lifetimes of ψ_0 (red) and ψ_1 (orange) as a function of transverse magnetic anisotropy term E, with $T = 0.1$ K. **(c)** Energy difference between ground state and first excited state for the same situation as **b**. The dashed line indicates $eV_{\text{bias}} = 0.1$ meV and used for the lifetime calculations.

considered in the magnetic anisotropy terms, leaving us with spin momentum only, so then: $H_{\text{Zeeman}} = g\mu_B \mathbf{B}\cdot\mathbf{S}$. Combining this with the previous terms we get:

$$H_{\text{SingleAtom}} = g\mu_B \mathbf{B}\cdot\mathbf{S} + DS_z^2 + E(S_x^2 - S_y^2) \tag{2.9}$$

The g is the g-factor, which is typically $g \approx 2$ and $\mu_B = 5.79\cdot 10^{-2}$ meV/T is the Bohr magneton. In the case of Fe on Cu_2N/Cu(100) this energy is smaller than D, though this is not necessarily the case. Also, in the case of $S = \frac{1}{2}$ where D does not matter, this energy actually dominates. This is the case for TiH on MgO. This system can be considered a spin-½ system and, in the presence of a magnetic field, its entire Hamiltonian can in principle be described by H_{Zeeman}. This is interesting for the purposes of ESR where the resulting two-level system is favoured for its simplicity and will be considered in section 3.5.

Going back to Fe on Cu_2N/Cu(100), where $g \approx 2.11$ and so $g\mu_B \approx 0.1$ meV/T, we can see that the term can be similar in magnitude to E. One has to consider the relative orientation of the magnetic field with respect to the easy axis as defined by the anisotropy. As we have established above, coefficients in front of S_z push the states towards ± 2, and coefficients in front of S_x or S_y have a strong effect on the superposition of states. This still holds here: by applying only B_z, the dot product yields S_z^2 which provides a typical Zeeman splitting. This is because the $\psi_0 \rightarrow N_B$ and $\psi_1 \rightarrow N_A$, which now split in energy due to the magnetic field. Meanwhile, applying B_x results in S_x terms which we saw before can be rewritten in terms of S_+ and S_- operators. Now instead of hydridizing states

that are two spin-values away ($\{-2,0,2\} and \{-1,+1\}$), neighbouring spin-values are hybridized as well. Nonetheless, even B_x will play a profound role in the energy distribution of the states.

From Table 2.3 we can see that the introduction of B_z respected the separation of $m_s = \{-2,0,2\}$ and $m_s = \{-1,1\}$. The choice of $B_z = 7T$ corresponds with [1]. From Figure 2.5 we can see that as B_z increases, the mixing is decreased for the four lowest states and each state now has a preferred "side". We will say it's skewed to either spin-direction. Moreover, due to the energy associated with each side, the states split further in energy. This can also be seen in the states ψ_2 and ψ_3.

Table 2.3: State decomposition for Equation 2.9, with $D = -1.87$ meV, $E = 0.31$ meV and $B_z = 7$ T

	$m_s = -2$	$m_s = -1$	$m_s = 0$	$m_s = +1$	$m_s = +2$	Energy (meV)
ψ_0	0.996		-0.083		0.018	0
ψ_1	-0.028		-0.125		0.992	3.388
ψ_2		-0.916		0.402		6.12
ψ_3		0.402		0.916		8.646
ψ_4	-0.08		-0.989		-0.127	9.412

As ψ_0 lowers in energy, all other states have moved up in comparison. At $B_z = 7T$ the energy difference $\Delta E_{0,1} > \Delta E_{1,2}$, which allows for over-the-barrier excitations one way, but not the other. As we will see shortly, this results in lifetime ratios that may be unexpected.

In order to prepare us for later, let's make the observation that ψ_0 is still symmetric and ψ_1 is still anti-symmetric, according to the previously given naming convention. Furthermore, ψ_0 is clearly skewed towards N_B and ψ_1 is skewed towards N_A.

TRANSITION RATES

Figure 2.6a shows that as B_z increases, the first step becomes smaller, indicating that the scattering amplitude $P_{1,0}$ decreases. This makes sense given that $\psi_0 \rightarrow N_B$ and $\psi_1 \rightarrow N_A$. Note that the second step becomes slightly taller as B_z increases: this makes sense because ψ_0 and ψ_2 are both heavily skewed towards $|-2\rangle$ and $|-1\rangle$, respectively, which are within $\Delta m_s = \pm 1$. However, these higher states are not as skewed as the lower states: Figure 2.5 and Table 2.3 both show that the $\langle +1|\psi_2\rangle > \langle +2|\psi_0\rangle$. Because of this $P_{2,1} > P_{0,1}$. This provides an important second relaxation path for $\psi_1 \rightarrow \psi_0$ namely through ψ_2 which higher intensity.

In fact, if we put $eV_{\text{bias}} = \Delta E_{0,1}$, as done in Figure 2.6b,c the lifetime T_1^S is limited by excitations through ψ_2. As a result, the ratio in lifetimes $\frac{T_1^S}{T_0^S}$ is much lower. If there

were no higher states available, from the Fermi-Dirac distribution at the given conditions (1 K), we would expect a lifetime ratio close to 10^{-2}. Instead, ignoring bath electrons for now and the tip at $eV_{\text{bias}} = \Delta E_{0,1}$, we find this ratio to be about 10^{-3}. This is due to over-the-barrier excitations one way, but not the other. Bath electrons will have thermal energy significantly below $\Delta E_{0,1}$, hence they assist in relaxation only. Once we include these, the ratio drops to about 10^{-4}. One must therefore always consider over-the-barrier excitations.

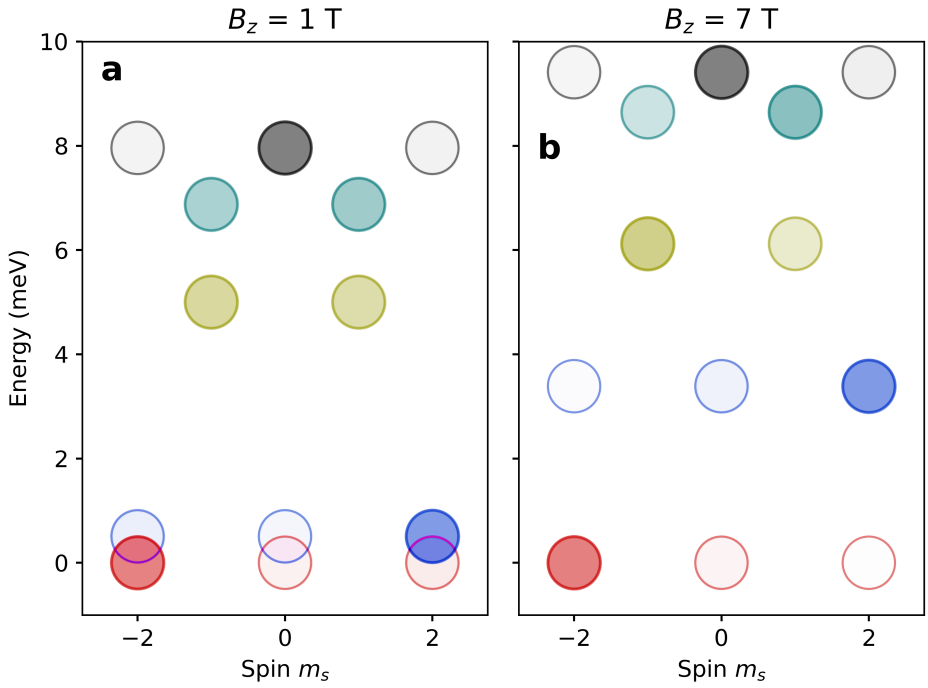

Figure 2.5: Energy diagram for Equation 2.9. **(a)** Energy diagram for all five states of $N = 1$, $S = 2$, $D = -1.87$ meV, $E = 0.31$ meV and $B_z = 1$ T. **(b)** Same as **a**, but for $B_z = 7$ T. Color coding same as Figure 2.3.

The lifetime of ψ_0 in Figure 2.6b clearly shows a kink occuring at $B_z \approx 7$ T, when the tunnel electrons stop having enough energy to excite the system to ψ_1. As a result, only the tail of the Fermi-Dirac distribution is able to excite the system towards ψ_1, resulting in very long lifetimes for ψ_0, while the lifetimes of ψ_1 is barely affected.

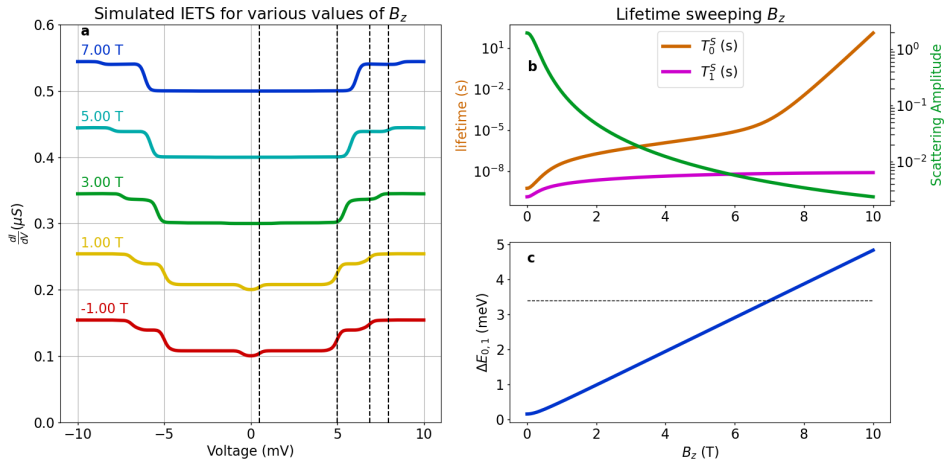

Figure 2.6: Simulated IETS and lifetime for Equation 2.9. (a) Simulated IETS measurements. Dashed lines at 0.51 meV, 5.00 meV, 6.88 meV and 7.96 meV corresponding to the steps for $B_z = \pm 1$ T. Consecutive plots (red, yellow, green, cyan, blue) are offset by 0.1μS. **(b)** Scattering amplitude (green) and lifetimes of ψ_0 (red) and ψ_1 (orange) as a function of easy axis magnetic field B_z. **(c)** Energy difference between ground state and first excited state for the same situation as **b**. The dashed line indicates the $eV_{\text{bias}} = 3.388$ meV, which corresponds to $\Delta E_{0,1}$ for $B_z = 7$ T and used for the lifetime calculations. Temperature in **a, b** is $T = 1$ K.

Summary

- The states $N_+ \approx N_A + N_B$ and $N_- \approx N_A - N_B$ become less valid when a longitudinal field is applied.
- Instead, the application of a longitudinal field skews the two lowest energy eigenstates towards N_B and N_A, respectively.
- Over-the-barrier excitations as a result of a too high bias voltage or temperature can result lower lifetimes for one of both states.

2.1.4. TRANSVERSE MAGNETIC FIELD

What happens if we instead apply a magnetic field along the hard axis: B_x? Before we saw how $S_x^2 - S_y^2 = \frac{S_+^2 + S_-^2}{2}$. Based on similar rewriting of spin-operators, $S_x = \frac{S_+ + S_-}{2}$. As a result, all five spin states $m_s = \{-2, -1, 0, 1, 2\}$ are now linked together. Figure 2.7 shows this is true for all states except for ψ_1 and ψ_2, which exhibit anti-symmetric behaviour in that they have no contribution in $m_s = 0$.

The most important point to focus on is that as B_x increases, $\Delta E_{0,1}$ decreases. With B_x large enough, an energy crossing will occur at a so-called diabolic point B_{diab}. When $B_x > B_{\text{diab}}$ the ground state is no longer $\sim N_+$, but instead $\sim N_-$. This leads to several

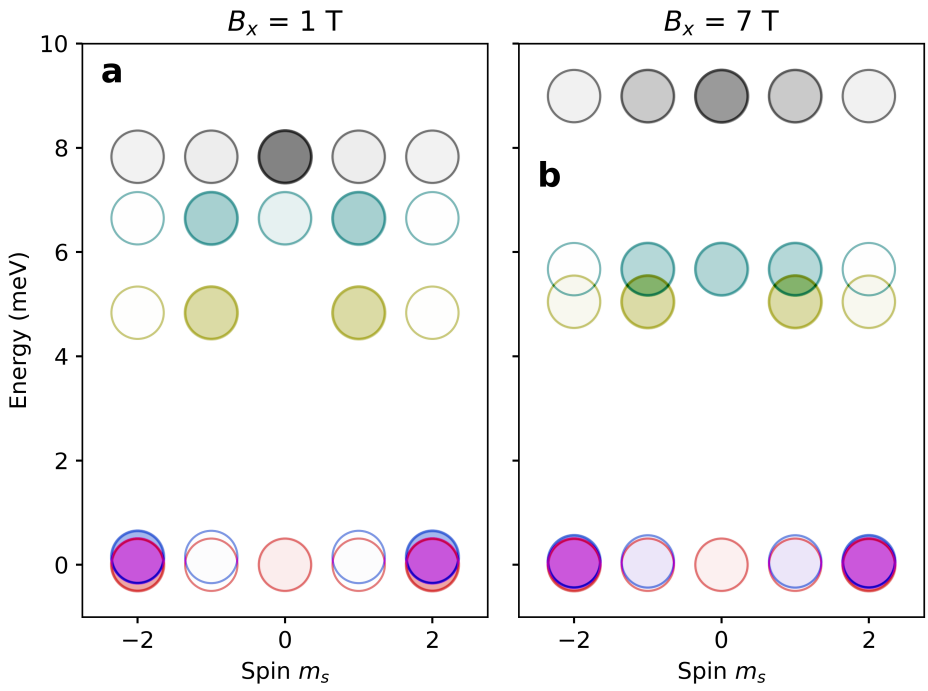

Figure 2.7: Energy diagram for Equation 2.9. **(a)** Energy diagram for all five states of $N = 1$, $S = 2$, $D = -1.87$ meV, $E = 0.31$ meV and $B_x = 1$ T. **(b)** Same as **a**, but for $B_x = 7$ T. Color coding same as Figure 2.3.

questions:

1. Why does B_x affect $\Delta E_{0,1}$?
2. Is there an analytical expression to B_{diab}?
3. Is there a phase transition at B_{diab}?
4. Is there any other behaviour when B_x increases even further?
5. How do pertubations like B_z affect this energy crossing?

To fully answers these questions means venturing into the realms of diabolic points, Berry phases and instantons [15–19], most of which is outside the scope of this thesis. What we can say is that there is an analytical expression to these diabolic points [15]:

$$B_{\text{diab}}(n) = (S - n - \frac{1}{2})\frac{2\sqrt{2E(E-D)}}{g\mu_B} \tag{2.10}$$

Here S is the spin of our system, in our case $S = 2$. The diabolic point number n tells us there can be more such points. In this case the number of points is quite limited: $|n| = \{0, 1\}$. The absolute signs tell us that we will only focus on positive values of

B_x, as the effect is entirely symmetric. The total number of diabolic points is equal S rounded down (e.g. 2 points if $S = 2.5$). Based on Equation 2.10, we find in our case that $B_{\text{diab}}(1) \approx 9.5$ T. Within the context of bistability, there is nothing of interest yet: it is impossible to place our $B_x = B_{\text{diab}}$ with infinite precision and the behaviour close to this point is nothing out of the ordinary. The lifetime graph can be fully described by the energy. We will soon see that this is not always the case.

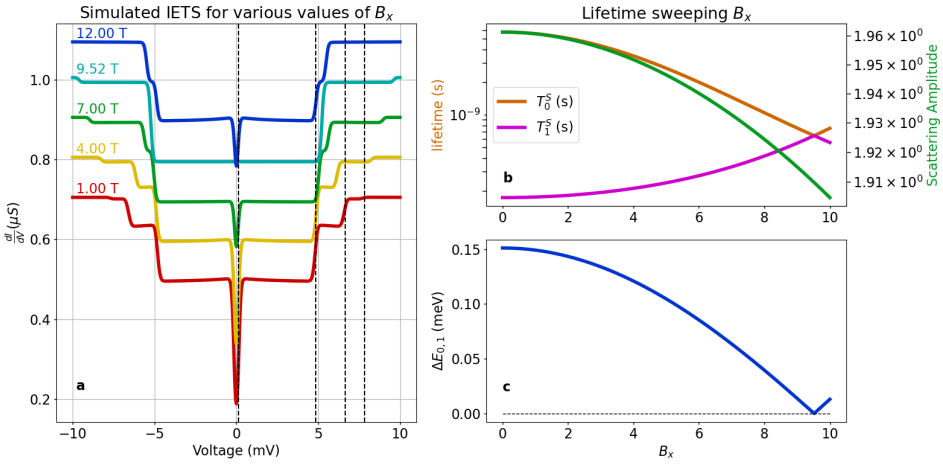

Figure 2.8: Simulated IETS and lifetime for Equation 2.9. (a) Simulated IETS measurements. Dashed lines at 0.15 meV, 4.84 meV, 6.65 meV and 7.83 meV corresponding to the steps for $B_x = \pm 1$ T. Consecutive plots (red, yellow, green, cyan, blue) are offset by 0.1μS. **(b)** Scattering amplitude (green) and lifetimes of ψ_0 (red) and ψ_1 (orange) as a function of hard axis magnetic field B_x, with $T = 0.5$ K **(c)** Energy difference between ground state and first excited state for the same situation as **b**. The dashed line indicates the $eV_{\text{bias}} = 0$ meV and used for the lifetime calculations.

To return to our questions: the exact reason why B_x lowers $\Delta E_{0,1}$ remains outside the scope of this thesis. The other questions are not outside the scope of this thesis. There is an analytical expression, as given by Equation 2.10, and there is no phase transition as behaviour is otherwise the same before and after these diabolic points. However, beyond the last (in this case second) diabolic point there is a phase transition in that the ground state is determined by B_x and there is a linear growth with this magnetic field: Zeeman splitting. Depending on the spin of the system there may be more such points. In the next section we will see how a longitudinal field B_z will allow us to probe the "inside" of this diabolic point as the crossing becomes an avoided crossing with a certain range in parameter space.

TRANSITION RATES

Figure 2.8a also clearly shows the decreasing $\Delta E_{0,1}$, with the first step becoming smaller as B_x increases: at $B_x = B_{\text{diab}}$ the excitations become already possible without any bias voltage. Besides the shifting of the steps, the IETS spectra look remarkably similar. This

is consistent with literature [1, 20]. Focusing now on Figure 2.8b,c we see behaviour as expected. For simiplicity's sake, we have $V_{\text{bias}} = 0V$. As the energy gap decreases, the lifetime ratio goes to unity. This can be fully described by the energy, as the scattering amplitude $P_{i,j}$ barely changes. Beyond B_{diab} there seems nothing different, but in reality the definitions of ψ_0 and ψ_1 have now changed. To the right of the diabolic point $\psi_0 \approx N_-$ and $\psi_1 \approx N_+$, which is the reverse compared to before the diabolic point.

We can decide to plot this on a Bloch sphere, as shown in Figure 2.9. Notice that we placed the states N_A and N_B at the poles, such that the eigenstates resides on the x,y-plane now. Before the diabolic point, we are in the situation described by subfigure (a), after the diabolic point it's panel (b). It's as if passing the diabolic point induced an instantaneous inversion along the y,z-plane, the plane spanning the poles .

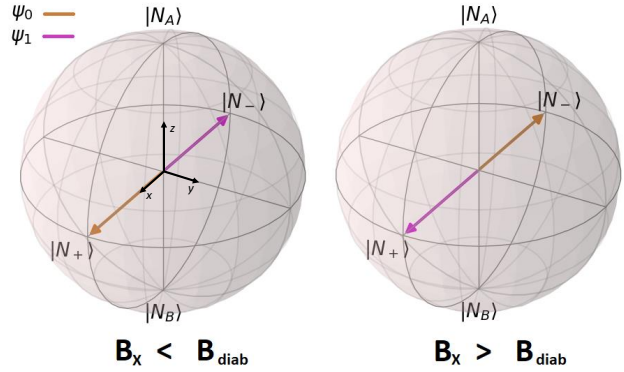

Figure 2.9: Bloch picture of N_+ and N_-. (a) For $B_x < B_{\text{diab}}$ the ground state (orange) is at $\psi_0 = N_+ = N_A + N_B$. The first excitated state (pink) is at $\psi_1 = N_- = N_A - N_B$. **(b)** For $B_x > B_{\text{diab}}$ the states underwent an inversion along the y,z-plane. The states being exactly at the equator holds only for no perturbation (e.g. $B_z = 0$ mT).

Summary

- Sweeping B_x yields so-called *diabolic* points B_{diab} where the states N_+ and N_- cross in energy.
- This energy crossing can be seen as inversion along the y,z-plane of a Bloch sphere containing N_A and N_B on the top and bottom, respectively.
- The number of diabolic points depends on the spin of the system and they occur at values gives by Equation 2.10.

2.1.5. LONGITUDINAL AND TRANSVERSE FIELD

As we have just seen, there are diabolic points where the states $N_+ \approx N_A + N_B$ and $N_- \approx N_A - N_B$ cross in energy (as defined along $\langle N_+|H|N_+\rangle$ and $\langle N_-|H|N_-\rangle$). Then a natural

question to ask is what would happen at the crossing if N_A and N_B have different energies? We have seen that we can apply such energy through application of B_z. So that is what we will investigate now.

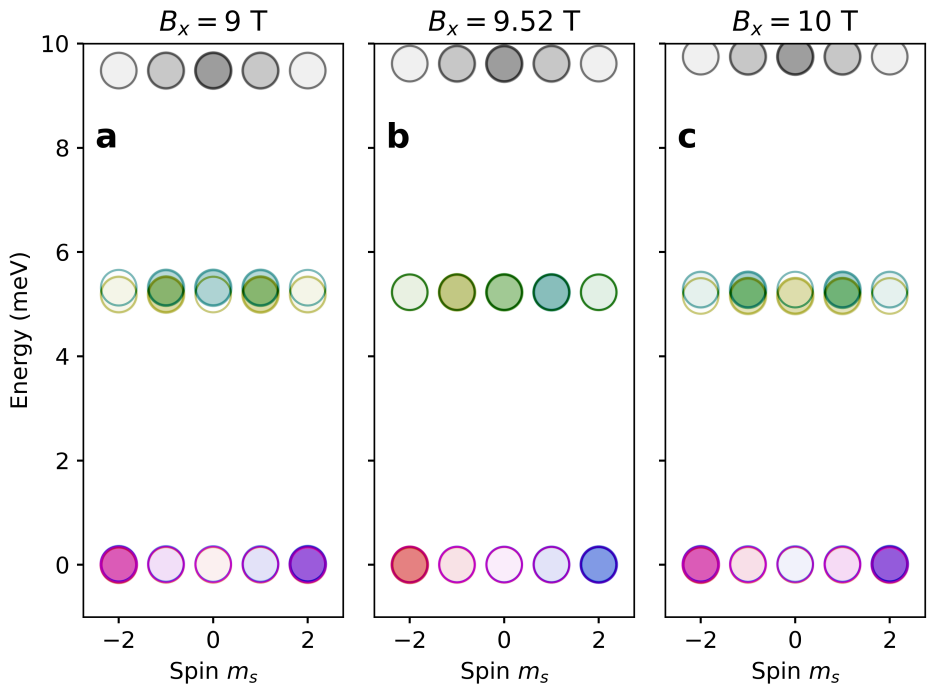

Figure 2.10: Energy diagram for Equation 2.9. **(a)** Energy diagram for all five states of $N = 1$, $S = 2$, $D = -1.87$ meV, $E = 0.31$ meV and $B_z = 10$ mT and $B_x = 9$ T. **(b)** Same as **a**, but for $B_x = 9.52$ T. **(c)** Same as **a**, but for $B_x = 10$ T. Color coding same as Figure 2.3.

We will now look at the energy diagram in three situations. Figure 2.10a shows the energy diagram at $\mathbf{B} = (9, 0, 0.01)$ T, (b) shows $\mathbf{B} = (9.52, 0, 0.01)$ T and (c) shows $\mathbf{B} = (10, 0, 0.01)$ T . So, one well before the diabolic point, one at the diabolic point and one well beyond the diabolic point. It's clear that at the diabolic point ψ_0 is still heavily skewed towards N_B (and $\psi_1 \rightarrow N_A$) as the contributions in $m_s = \pm 2$ are red/blue instead of shades of purple: this is reminiscent of what we saw in Figure 2.5. This same skewing also happens in the higher states ψ_2 and ψ_3. When we're not on the diabolic point, such as at $B_x = 9$ T, there is still some skewing, but to a significant smaller degree. The fact that the figure shows shades of purple at $m_s = \pm 2$ instead of red/blue indicates that both energy eigenstates have significant contributions in both spin states. This leads to a large scattering amplitude $P_{0,1}$. A similar point can be made about states ψ_2 and ψ_3. When we go beyond the diabolic point, we see similar behaviour, although now the symmetry has now changed. Now ψ_1 and ψ_2 contain a contribution in $m_s = 0$. This extreme skewing towards N_A and N_B and resulting decrease in the scattering amplitude has profound

effects on the lifetime of these two lowest energy eigenstates, which we will explore now.

TRANSITION RATES

With the effect of the diabolic point on IETS fully captured by Figure 2.8, we will now consider only the lifetime, scattering amplitude and energy plots in this subsubsection. These are shown in Figure 2.11. In this case $V_{\text{bias}} = 3$ mV, which reflects experimental conditions.

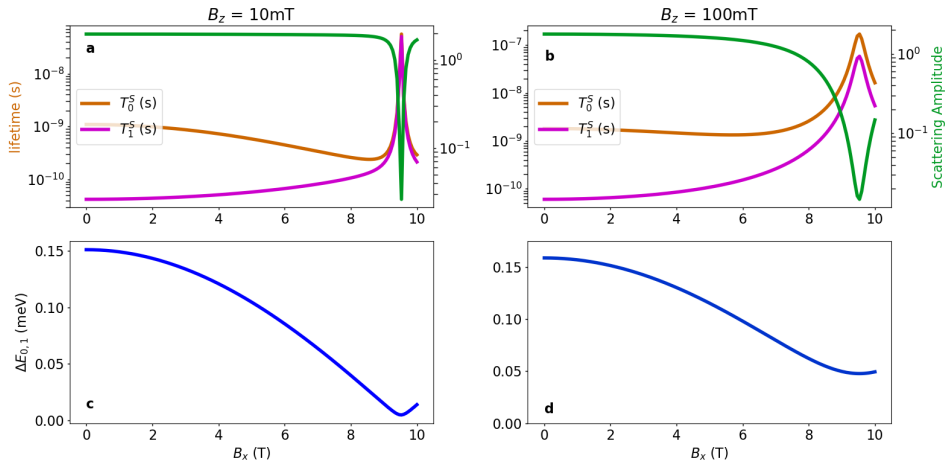

Figure 2.11: Lifetime for Equation 2.9 around the diabolic point. **(a)** Scattering amplitude (green) and lifetimes of ψ_0 (red) and ψ_1 (orange) as a function of hard axis magnetic field B_x. $eV_{\text{bias}} = 3$ meV and $B_z = 10$ mT, with $T = 0.5$ K. **(b)** Energy difference between ground state and first excited state for the same situation as **a**. **(c-d)** Same as **a-b** but for $B_z = 100$ mT.

Unlike anything we have seen before, there are now peaks in both lifetimes, which coincide with a dip in the scattering amplitude and the avoided crossing in the energy. We find that the larger the avoided crossing gap size, the larger the lifetime peak width W. This affects both T_0^{S} and T_1^{S}. These peaks in the lifetime are actually measurable, and have been done so experimentally for spin chains in Chapter 4. For now we will explore (1) why this happens (2) what the relationship between peak width and gap size $W(\Delta)$ looks like, and (3) whether this also work for chain? For the first two points we refer to Figure 2.12.

Shown in Figure 2.12a we see how, just like before, there is a rotation along the Bloch sphere when we pass the diabolic point. There are two major differences, though. The first is that, even far from the diabolic point the application of B_z skews the states $\psi_0 \rightarrow N_B$ and $\psi_1 \rightarrow N_A$, as we have seen in section 2.1.3. This is represented by having the state vectors point at about 50° away from the x,y-plane, although the exact angle is not relevant for this conceptual picture. Either way, ψ_0 is still on the front side, indicating that its still symmetric (N_+). When we have far surpassed the diabolic point, we will again find ourselves at 50°, but now with ψ_1 on the N_+ side, as we have seen in section 2.1.4. The

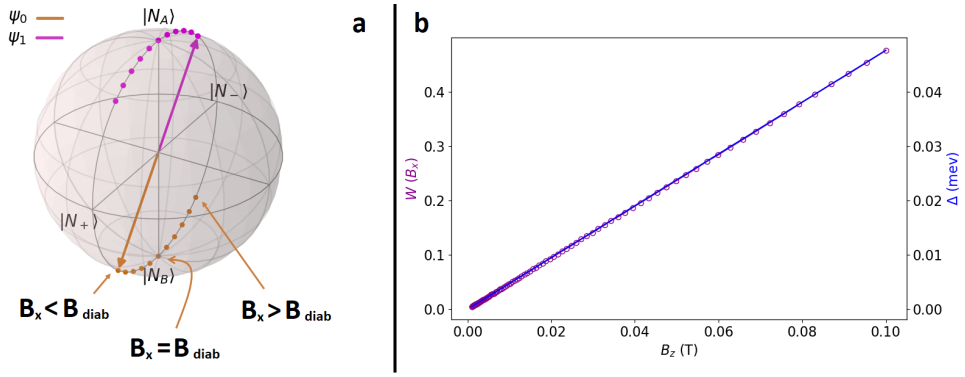

Figure 2.12: Effect of pertubation on the Bloch rotation and peak width. **(a)** A Bloch sphere representing the two lowest energy eigenstates (orange and pink, respectively) in a vector field containing B_z and B_x as a function of N_A and N_B. The arrows indicate the states when $B_x < B_{\text{diab}}$. The dots show intermediate steps as B_x crosses B_{diab}. Of particular importance is that when $B_x = B_{\text{diab}}$ the eigenstates are at N_B and N_A. **(b)** Peak width W (purple circles) and avoided crossing gap energy Δ (blue line) as a function of B_z.

second important difference is that instead of an immediate inversion, the states take about the avoided crossing's width in B_x-space to rotate. During this rotation, at exactly $B_x \approx B_{\text{diab}}$, the states $\psi_0 \approx N_B$ and $\psi_1 = N_A$. This is also shown in Figure 2.10. At this point the scattering amplitude $P_{1,0}$ will be extremely small, leading to an increase in the lifetime of several orders of magnitude, as shown in Figure 2.11.

Shown in Figure 2.12b we see that as we increase the term B_z both the avoided crossing gap Δ and peak width W increase linearly. The avoided crossing gap Δ is defined as the $\Delta E_{0,1}$ at the diabolic point. The peak width is defined as the difference $|B_{\text{diab}} - B_x^*|$ where $T_1^S(B_x^*) = \frac{T_1^S(B_{\text{diab}})}{10}$, so one order of magnitude smaller. We use this definition instead of the more common FWHM (full width at half maximum) because, as shown in Figure 2.11b it is hard to define where the peak in ψ_1 even starts. Not surprisingly Δ increases linearly with B_z as this represents the Zeeman energy. The actual value of Δ is slightly smaller (~ 3%), reflecting the fact that $\langle -2|\psi_0\rangle \neq 1$. A similar linear relationship exists between W and B_z. There must therefore then also be a linear relationship between the avoided crossing energy Δ and peak width W. In the specific case simulated here, we find $W \approx 10\Delta/\text{meV}$ (in Teslas). This approximation holds for $T \sim 1$ K and $V_{\text{bias}} \sim 3$mV, but has room for deviation in both experimental parameters and the values of D, E and g.

Finally, let us consider where the name *diabolic point* comes from. It was termed by Michael Berry since, when plotting the energy E and magnetic fields B_x and B_z in a 3D-plot, you get something similar to the shape of the toy *diabolo*: a double cone [21]. This is also true in our case, as evidenced by Figure 2.13. The energy surfaces of ψ_0 (orange) and ψ_1 (pink) spanned by B_x and B_z around the diabolic point indeed follow a similar shape. As was previously shown, there are multiple of these diabolic points in the B_x,B_z-parameter space [15], although we will mostly be focusing on this one. Notice

that Figure 2.16 are two vertical slices through this diabolo. As we will see in Chapter 4, due to the experimental situation, B_x and B_z are swept at the same, with a certain ratio. This then results in a diagonal slice through this diabolo.

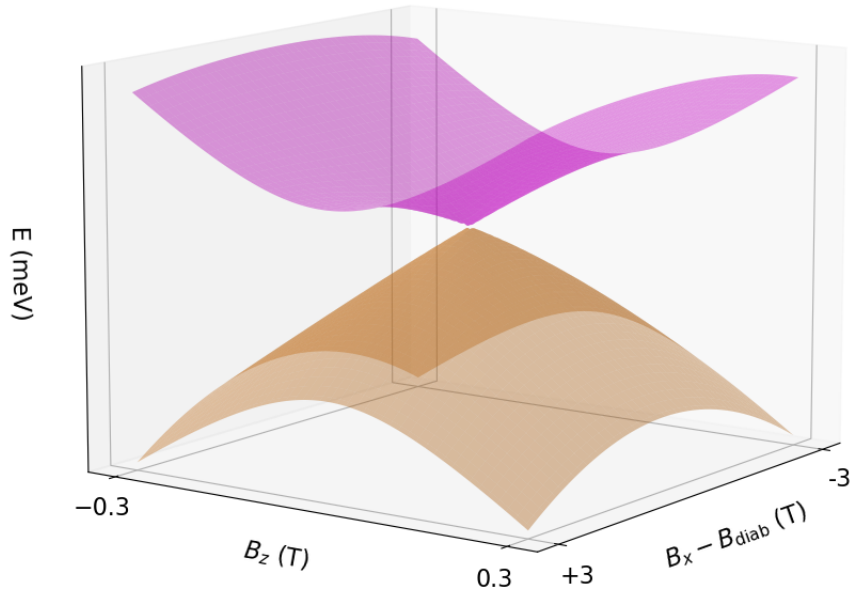

Figure 2.13: Diabolic Point in 3-dimension parameter space. The diabolic point shows a double cone-like structure between when plotting the energies of ψ_0 (orange) and ψ_1 (pink) as a function of B_x and B_z around the diabolic point. Image is a simulation result but slightly modified for clarity, as the original result include a strong slope.

Armed with a thorough understanding of how Equation 2.1 affects a single atom and can even lead to diabolic points, we can turn our attention to chains of atoms.

Summary

- The application of a longitudinal field B_z creates an avoided crossing with gap size Δ, around which the Bloch sphere inversion of the diabolic point happens in a trajectory around the edge of the Bloch sphere along the x,z-plane.
- Exactly at the diabolic point $\sigma_{1,0}$ is reduced to a minimum which leads to a peak in the lifetime.
- For Fe_1 on Cu-sites on $Cu_2N/Cu(100)$ the peak width can be approximated as $W \approx 10\Delta$ T/meV

2.2. ATOMIC SPIN CHAIN

So far we have explored physics of a single adatom. We will now extend this exploration to chains. In particular, chains of Fe_N, where N is the chain length, on $Cu_2N/Cu(100)$. The way the atoms of the chain couple together can be summarized as was done by the last part of Equation 2.1:

$$H_{\text{Heisenberg}} = \sum_{i}^{n-1} J_i S_i \cdot S_{i+1} \tag{2.11}$$

Here J_i is the coupling strength between spin S_i and S_{i+1} belonging to atoms i and $i+1$. The value of J_i may depend on the spacing and orientation between the atoms. This will be important in the case Chapter 5. This equation considers only nearest-neighour coupling. We will now continue in our exploration of the how the Hamiltonian leads to diabolic points and, as we will see soon, magnons. Before all of that, let us take a look at the simulated IETS spectra.

2.2.1. COUPLING STRENGTH J

It's important to realize a big distinction between inner and outer atoms. For a chain of size $N = 2$, there are only two outer atoms, each of which experience a single coupling strength J. Meanwhile for $N = 3$ the inner atom experiences two coupling strengths J. This leads to a clear distinction between inner and outer atoms. As such when we consider a chain of $N = 3$, we will look at inner and outer atoms seperately. Further on we also consider a chain of $N = 2$.

We can now also introduce the term Néel states. These are relevant for the case $J > 0$ where neighbouring atoms are antiferromagnetically coupled. These are $N_A = \{+2, -2, +2, ..\}$ and $N_B = \{-2, -2, +2, ..\}$. We can see that if $N = 1$, we get the $N_A = \langle +2 \rangle$ and $N_B = \langle -2 \rangle$.

Figure 2.14 shows the simulated IETS spectra for various values of J, for a trimer: a chain of length $N = 3$. We now see many more smaller steps, which is due to the fact that we now have 5^3 states, many of whom are present in this voltage range. In fact, for $J = 0.7$ meV, the first 18 states are in this voltage range of ± 10 mV. As is clear from the difference between IETS spectra for the (a) outer and (b) inner atom, many of the the associated steps are hidden. The dashed lines show where the main step is for outer and inner atoms at $J = 0.7$ meV. These are different because for outer atoms it is excitations towards $\{\pm 1, \pm 2, \pm 2\}$ and $\{\pm 2, \pm 2, \pm 1\}$ whereas for inner atoms they are towards $\{\pm 2, \pm 1, \pm 2\}$. As we have discussed before, these latter are associated with higher energy due to the additional cost in J. What is also apparent from the (a) is that for $J = \pm 0.1$ there is still a step at lower energies, leading towards ψ_1. In the next section we will explore this further.

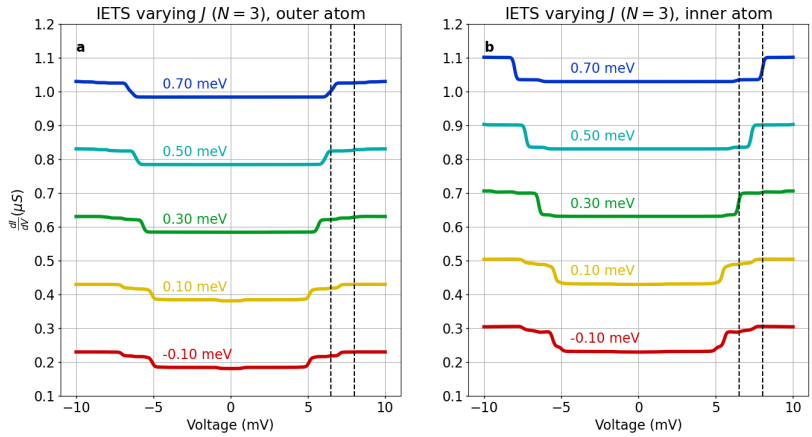

Figure 2.14: Simulated IETS and lifetime for Equation 2.1. (a,b) Simulated IETS measurements for outer and inner atoms of trimer, respectively for various values of J. Dashed lines at 6.50 meV, 8.02 meV corresponding to the steps for $J = 0.7$ meV for outer and inner atom respectively. Consecutive plots (red, yellow, green, cyan, blue) are offset by 0.2μS. Third atom has $D^* = 1.86$ meV to increase numerical stability.

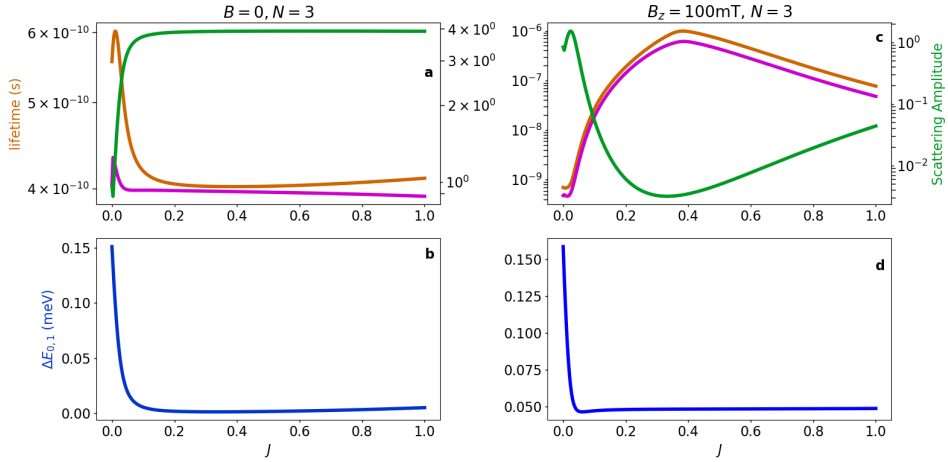

Figure 2.15: Lifetime for Equation 2.1 around the diabolic point for $N = 3$. (a) Scattering amplitude (green) and lifetimes of ψ_0 (red) and ψ_1 (orange) as a function of coupling strength J. $eV_{\text{bias}} = 3$ meV and $B_z = 0$ T, with $T = 0.5$ K. Third atom has $D^* = 1.86$ meV to increase numerical stability. **(b)** Energy difference between ground state and first excited state for the same situation as **a**. **(c-d)** Same as **a-b** but for $B_z = 100$ mT.

2.2.2. TRANSITION RATES

We will explore two different scenarios, as shown in Figure 2.15: $\mathbf{B} = (0,0,0)$ T and $\mathbf{B} = (0,0,0.1)$ T. Right from the start it is clear that for J very small the scattering amplitude $P_{1,0}$ is reduced significantly compared to the single atom case. This is because ψ_0 has

significant contributions in all eight states $\{\pm2,\pm2,\pm2\}$, due to being in the mostly N_+ state for all three atoms. Meanwhile ψ_1 only has significant contributions in the two Néel states $\pm\{2,-2,2\}$. However, as soon as J increases $\Delta E_{0,1}$ decreases from the value 0.15 meV (as caused by the magnetic anisotropy term E) as both energy eigenstates align themselves with the Néel states $\pm\{2,-2,2\}$ as the coupling strength J dominates. As a result the scattering amplitude $P_{0,1}$ increases towards its maximum value. When an additional field B_z is applied $P_{0,1}$ goes down for increasing J as $\psi_0 \to N_B$ and $\psi_1 \to N_A$. As J increases even further, the contribution $\langle N_A|\psi_0\rangle$ and $\langle N_B|\psi_0\rangle$ increases as the Zeeman term becomes relatively small, which in turn increases $P_{0,1}$ again.

Throughout this thesis we will consider two values: $J = 0.7$ meV and $J' = -0.05$ meV. The first term is used for two Fe atoms that are two lattice sites apart along the easy axis. These are used in Chapters 4 and 5. The second one is used for two Fe atoms that are three lattice sites apart along the same easy axis. With $J < 0$ this will cause ferromagnetic coupling. This is used only for Chapter 5. For the rest of this theory chapter we will assume $J = 0.7$ meV unless stated otherwise.

2.2.3. DIABOLIC POINTS IN CHAINS

The question of what chain length N to study lifetimes of boils down to the following two considerations. (1) The longer the chain the longer the lifetime. This is because as N increases the states spread out over more spin eigenstates and $P_{0,1}$ decreases exponentially. (2) For J large enough, odd chains in a field containing B_z *will* gain Zeeman energy, wheras even chains *will not*. This is because in even chains for every spin aligned with the field, there will be a spin anti-aligned. In otherwords N_A and N_B have the same energy, irrespective of B_z.

This last point would then also suggest that it is impossible to measure diabolic points on even chains, as peak width W would be zero. However, in Chapter 4 it is shown that even on Fe_6 it is possible to measure a diabolic point with significant width. This is because during experiments the exact values of D, E, J and g are not exactly the same for each atom. This leads to energy differences between N_A and N_B. From simulations we can see that variations in D and E don't cause a significant Δ, but variations in g do. Nonetheless, it can sometimes be useful to have a value $D^* = D + 0.01$ meV to assure we don't simulate an idealized case, as this breaks symmetry. Furthermore, a magnetic field produced by the probing tip can cause a local field felt by only a single atom. This also causes Δ to increase.

We will consider two cases. The first case is an odd chain ($N = 3$) in a B_z field, and the second is an even chain ($N = 2$) with either a tip field or inhomogenous values of g with a B_z field. As we will see later, the introduction of J splits the diabolic points in N. In order to look at a single diabolic point only, we will look at large enough values of J, so $J = \{0.3, 0.5, 0.7, 1.0\}$ meV. These are plotted in Figure 2.16. This includes the experimentally relevant $J = 0.7$ meV, plotted thicker. For further distinguishing, the case $J = 1.0$ meV is dotted.

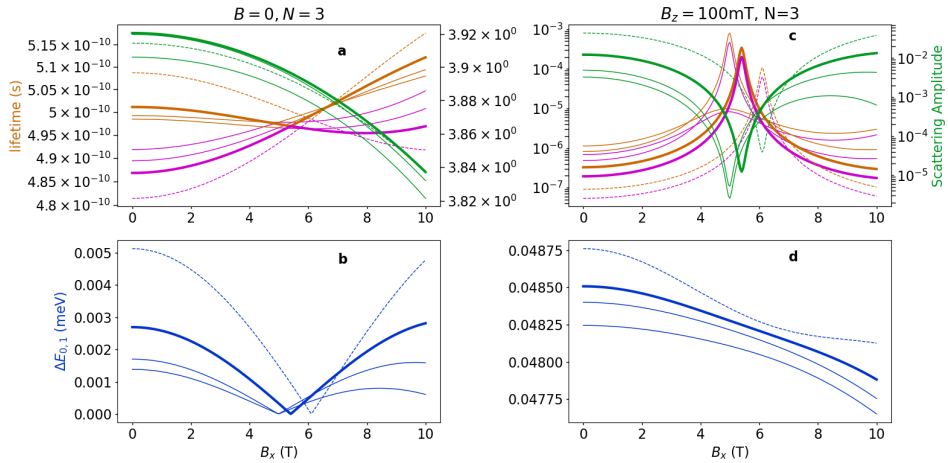

Figure 2.16: Lifetime for Equation 2.1 around the diabolic point for $N = 3$ and various J. (a) Scattering amplitude (green) and lifetimes of ψ_0 (red) and ψ_1 (orange) as a function of hard axis magnetic field B_x for values $J = \{0.3, 0.5, 0.7, 1.0\}$. Thick lines apply to $J = 0.7$ meV, dotted lines apply to $J = 1.0$ meV. $T = 1$ K, $u = 0.5$. $G = 0.1\mu$S, $G_S = 3.1\mu$S, $eV_{\text{bias}} = 3$ meV and $B_z = 0$ T. **(b)** Energy difference between ground state and first excited state for the same situation as **a**. **(c-d** Same as **a-b** but for $B_z = 100$ mT.

Compared to the single atom case, now irrespective of the value of J, the peak position B_{diab} has decreased significantly, to about 5 T. Overall the value of J does not seem to matter too much in this regime. The actual value of J may therefore deviate from the literature value $J = 0.7$ meV (thick in the plots) without loss of qualitative behaviour. What's interesting is that while there is no peak in T_1 for $B_z = 0$ T, there is a clear minimum of Δ. In contrast, while there is peak in T_1 for $B_z = 100$ mT, there is no clear minimum in Δ (with a faint exception at $J = 1.0$ meV (dotted)). The same thing is happening as before: irrespective of B_z there is a diabolic point B_{diab} where for $B_x < B_{\text{diab}}$ the ground state $\psi_0 \approx N_+$ and the first excited state $\psi_0 \approx N_-$. Beyond the diabolic point these are reversed. This leads to an energy crossing. When a perturbation energy makes this crossing an avoided crossing, as in the case of $B_z = 100$ mT, there is now a transition region. In the middle of this transition region, around $B_x = B_{\text{diab}}$, the states $\psi_0 \approx N_B$ and $\psi_1 \approx N_A$, which reduces $\sigma_{0,1}$ leading a peak in the lifetime. Although it may be very hard to tell from the energy spectra, there is in fact an avoided crossing, even at $B_z = 100$ mT.

We will now look at the case where $N = 2$ and apply both a local tip field on the one hand, and an inhomogenous g-factor with global B_z on the other hand. These are shown in Figure 2.17. On the left is the situation without any of these modifications. The middle shows three cases: $B_{\text{tip}} = \{0.1, 1, 10\}$ mT. The right shows the situation with an external global field of $B_z = 10$ mT and the first atom having a g-factor of 2.30, instead of 2.11.

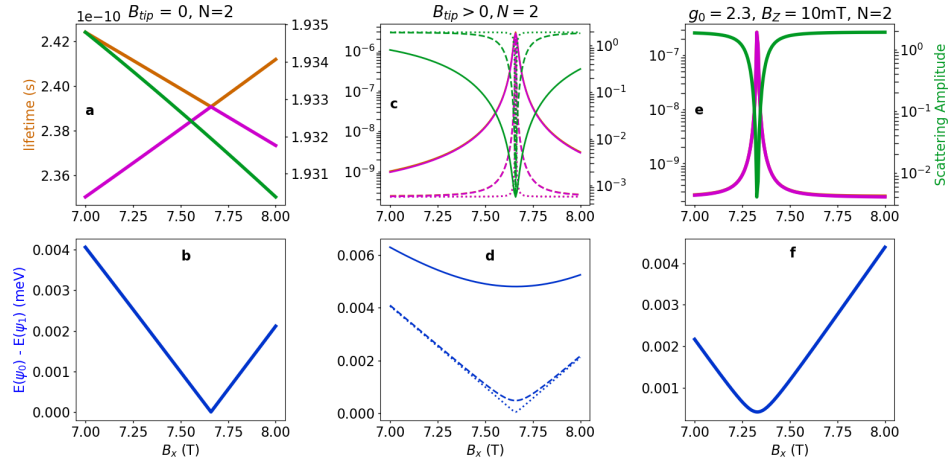

Figure 2.17: Lifetime for Equation 2.1 around the diabolic point for $N = 2$ **(a)** Scattering amplitude (green) and lifetimes of ψ_0 (red) and ψ_1 (orange) as a function of hard axis magnetic field B_x. $eV_{\text{bias}} = 3$ meV and $B_z = 0$ T. **(b)** Energy difference between ground state and first excited state for the same situation as **a**. **(c-d)** Same as **a-b** but for $B_{\text{tip}} = \{0.1, 1, 10\}$ mT, for respectively dotted, dashed and solid lines. **(c-d)** Same as **a-b** but with the first atom having $g = 2.30$ and $B_z = 10$ mT

As before, even though we see an energy crossing (left), we do not see a peak in the lifetime. The only way to see this is by "opening" the crossing and make it an avoided crossing. Figure (middle) nicely shows that as the avoided crossing becomes bigger, so does the peak width. Figure (right) shows that the peak can move depending on the value of g. What's interesting is that the peak occurs exactly in the middle of the two expected crossings, corresponding to the two values of g.

We have previously established Equation 2.10 to help us estimate B_{diab}. Unfortunately there is no known analytical expression for the value of B_{diab} for chains. The total number of diabolic points is the highest integer value of the total spin of the system. Thus, if $J = 0$ meV, there are N separate diabolic points on top of each: one for each atom. Once J increases, and the neighbouring atoms start to interact with one another, these overlapping diabolic points will fan out, as shown in Figure 2.18. For $J > 0$, i.e. antiferromagnetic chains, there is an value of J where B_{diab} reaches a minimum which depends on the length of the chain. For $J < 0$, i.e. ferromagnetic chains, there values of B_{diab} of the lowest diabolic points decreases for stronger values of J. Note, however, that for such ferromagnetic chains not only is the lifetime longer already for smaller chains, but also due to the larger gap energy between Δ the peak widths will be larger, leading to peaks that are harder to distinguish from one another. A full analysis of these possible other chains is outside the scope of this thesis.

For experimental results on these spin chains which exhibit diabolic point behaviour, we refer to Chapter 4. We will now move on to other behaviour in these same spin-chains. Here, instead of looking at the lifetimes of energy eigenstates, we will instead be looking at superpositions of energy eigenstates through excitations. The subsequent

non-pure states will evolve over time under the time-dependent Schrödinger equation.

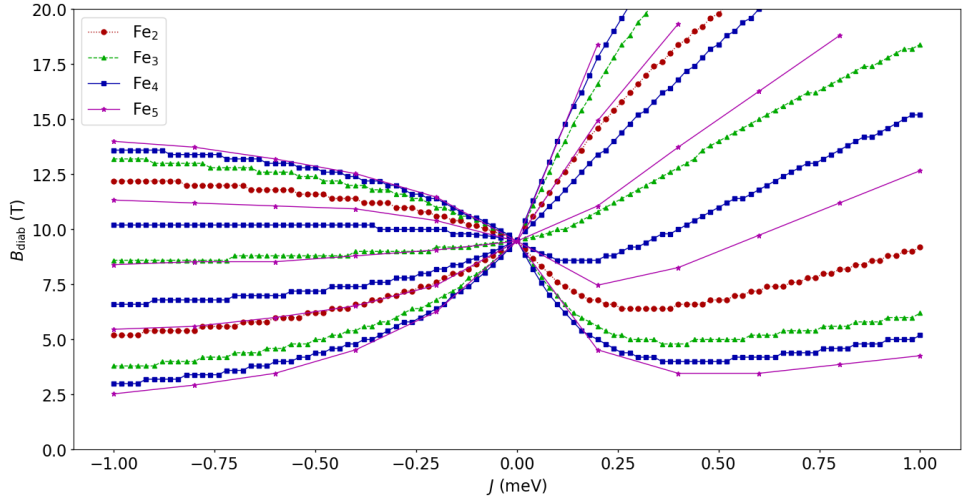

Figure 2.18: B_{diab} **for different chain lengths** N **and coupling strength** J Shown is calculated value of B_{diab} based on minima in the unperturbed energy spectra. Different colors, markers indicate different chain lengths.

2.2.4. TIME EVOLUTION OF A SPIN CHAIN

Any state that is not an energy eigenstate will have one or more phases that oscillates between its constituent eigenstates. The simplest example of this is a two-level system that is in a superposition of $\alpha|\uparrow\rangle+\beta|\downarrow\rangle$ in a magnetic field. Following the time-dependent Schrödinger equation this state will have an oscillating phase [22]:

$$\psi = \alpha e^{\frac{i\mu_B B}{\hbar}t}|\uparrow\rangle + \beta e^{-\frac{i\mu_B B}{\hbar}t}|\uparrow\rangle \tag{2.12}$$

This has also been shown experimentally and is used extensively in, among others, spin echo experiments [23] [24], [25]. We will explore this same concept in our spin chains as done in Chapter 5. The initial state, not an energy eigenstate, will be defined as follows. We initialize our spin chain by finding the ground state of equation 2.1. With $D = -1.87$ meV, $E - 0.31$ meV, $g = 2.11$, $J = 0.7$ meV, N odd, this will lead energy eigenstates where the ground state has a large contribution in $m_{s,1} = +2$ (the spin state of the first atom). On this atom we will apply an S_- operator. This is done to simulate a tunneling electron that performs a spin flip with the system. The system is then left to evolve over time. These simulations are repeated with instead of an S_- operator on the first atom, an S_+ operator is applied on the second atom. Subsequent repetitions of these simulations have S_+ operators applied on the odd-numbered atoms and S_- operators applied on the even-numbered atoms. During each simulation only a single operator is applied and the system is left to evolve for some time.

BIBLIOGRAPHY

1. Hirjibehedin, C. F. *et al.* Large Magnetic Anisotropy of a Single Atomic Spin Embedded in a Surface Molecular Network. *Science* **317,** 1199–1203. https://doi.org/10.1126/science.1146110 (2007).
2. Dai, D., Xiang, H. & Whangbo, M.-H. Effects of spin-orbit coupling on magnetic properties of discrete and extended magnetic systems. *Journal of computational chemistry* **29,** 2187–209. https://doi.org/10.1002/jcc.21011 (Oct. 2008).
3. Spinelli, A., Bryant, B., Delgado, F., Fernández-Rossier, J. & Otte, A. F. Imaging of spin waves in atomically designed nanomagnets. *Nature Materials* **13,** 782. https://doi.org/10.1038/nmat4018 (July 2014).
4. Yan, S., Choi, D.-J., Burgess, J. A. J., Rolf-Pissarczyk, S. & Loth, S. Control of quantum magnets by atomic exchange bias. *Nature Nanotechnology* **10,** 40. https://www.doi.org/10.1038/nnano.2014.281 (Dec. 2014).
5. Loth, S. *et al.* Controlling the state of quantum spins with electric currents. *Nature Physics* **6,** 340–344. ISSN: 1745-2481. https://doi.org/10.1038/nphys1616 (May 2010).
6. Delgado, F. & Fernández-Rossier, J. Spin dynamics of current-driven single magnetic adatoms and molecules. *Phys. Rev. B* **82,** 134414. https://doi.org/10.1103/PhysRevB.82.134414 (13 Oct. 2010).
7. Delgado, F., Hirjibehedin, C. & Fernández-Rossier, J. Consequences of Kondo exchange on quantum spins. *Surface Science* **630,** 337–342. ISSN: 0039-6028. https://doi.org/10.1016/j.susc.2014.07.009 (2014).
8. Ternes, M. Spin excitations and correlations in scanning tunneling spectroscopy. *New Journal of Physics* **17,** 063016. https://doi.org/10.1088/1367-2630/17/6/063016 (June 2015).
9. Choi, T., Lutz, C. P. & Heinrich, A. J. Studies of magnetic dipolar interaction between individual atoms using ESR-STM. *Current Applied Physics* **17,** 1513–1517. ISSN: 1567-1739. https://doi.org/10.1016/j.cap.2017.08.011 (2017).
10. Rejali, R. *et al.* Complete reversal of the atomic unquenched orbital moment by a single electron. *npj Quantum Materials* **5,** 60. ISSN: 2397-4648. https://doi.org/10.1038/s41535-020-00262-w (Aug. 2020).
11. Misiorny, M. *et al.* Probing transverse magnetic anisotropy by electronic transport through a single-molecule magnet. *Phys. Rev. B* **91,** 035442. https://doi.org/10.1103/PhysRevB.91.035442 (3 Jan. 2015).
12. Burzuri, E. *et al.* Quantum Interference Oscillations of the Superparamagnetic Blocking in an Fe_8 Molecular Nanomagnet. *Phys. Rev. Lett.* **111,** 057201. https://doi.org/10.1103/PhysRevLett.111.057201 (5 July 2013).

13. Bircher, R., Chaboussant, G., Sieber, A., Güdel, H. U. & Mutka, H. Transverse magnetic anisotropy in Mn_{12} acetate: Direct determination by inelastic neutron scattering. *Phys. Rev. B* **70,** 212413. https://doi.org/10.1103/PhysRevB.70.212413 (21 Dec. 2004).

14. Delgado, F. & Fernández-Rossier, J. Spin decoherence of magnetic atoms on surfaces. *Progress in Surface Science* **92,** 40–82. ISSN: 0079-6816. https://doi.org/10.1016/j.progsurf.2016.12.001 (2017).

15. Bruno, P. Berry Phase, Topology, and Degeneracies in Quantum Nanomagnets. *Physical Review Letters* **96.** https://doi.org/10.1103/physrevlett.96.117208 (Mar. 2006).

16. Garg, A. Berry phases near degeneracies: Beyond the simplest case. *American Journal of Physics* **78,** 661–670. https://doi.org/10.1119/1.3377135 (2010).

17. Wernsdorfer, W. & Sessoli, R. Quantum Phase Interference and Parity Effects in Magnetic Molecular Clusters. *Science* **284,** 133–135. https://doi.org/10.1126/science.284.5411.133 (1999).

18. Wernsdorfer, W., Chakov, N. E. & Christou, G. Quantum Phase Interference and Spin-Parity in Mn_{12} Single-Molecule Magnets. *Phys. Rev. Lett.* **95,** 037203. https://doi.org/10.1103/PhysRevLett.95.037203 (3 July 2005).

19. Villain, J. & Fort, A. Magnetic tunneling told to ignorants by two ignorants. *The European Physical Journal B - Condensed Matter and Complex Systems* **17,** 69–83. ISSN: 1434-6036. https://doi.org/10.1007/s100510070161 (Sept. 2000).

20. Žitko, R. & Pruschke, T. Many-particle effects in adsorbed magnetic atoms with easy-axis anisotropy: the case of Fe on the CuN/Cu(100) surface. *New Journal of Physics* **12,** 063040. https://doi.org/10.1088/1367-2630/12/6/063040 (June 2010).

21. Victor, B. M. & Mark, W. Diabolical points in the spectra of triangles. *Proc. R. Soc. Lond.* **A,** 15–43. https://doi.org/10.1098/rspa.1984.0022 (1984).

22. Feynman Richard P. (Richard Phillips), 1.-1. *The Feynman lectures on physics, Volume 3, 7-5* Vol. 2 has subtitle: The electromagnetic field; 3 has subtitle: Quantum mechanics.;Includes bibliographical references and indexes. https://search.library.wisc.edu/catalog/999468136802121 (Reading, Mass. : Addison-Wesley Pub. Co., c1963-1965., 1965 c1963).

23. Koppens, F. H. L., Nowack, K. C. & Vandersypen, L. M. K. Spin Echo of a Single Electron Spin in a Quantum Dot. *Phys. Rev. Lett.* **100,** 236802. https://doi.org/10.1103/PhysRevLett.100.236802 (23 June 2008).

24. Yang, K. *et al.* Coherent spin manipulation of individual atoms on a surface. *Science* **366,** 509–512. https://doi.org/10.1126/science.aay6779 (2019).

25. Veldman, L. M. *et al.* Free coherent evolution of a coupled atomic spin system initialized by electron scattering. *Science* **372,** 964–968. https://doi.org/10.1126/science.abg8223 (2021).

3

EXPERIMENTAL METHODS

3.1. INTRODUCTION

In this chapter the basic principles and techniques of measuring with a Scanning Tunneling Microscope (STM) will explained. The first section will address the basic measuring technique. Since the STMs used throughout this thesis all operate at cryogenic temperatures, their cooling systems are quickly discussed. Finally, three particular measuring techniques that are (becoming) common-practice in the field will be discussed: inelastic electron tunneling spectroscopy (IETS), pump and probe (P&P) and electron spin resonance (ESR). Their key results, physics explanation and implementation will be addressed. For the purposes of this thesis, IETS is used to identify atoms and binding sites. P&P is used to verify behaviour during the experiments performed in Chapter 5 and was used to explore lifetime of chains of length three during the experiments performed in Chapter 4. ESR is a technique with broad applications, but have specific cabling requirements which is further addressed in Chapter 6.

3.2. SCANNING TUNNELING MICROSCOPY

As explained in Chapter 1, STM is based on the tunneling effect of quantum mechanics. When two metals are brought close together without direct contact, such as a metallic tip and a metallic sample, the electrons of either metal can tunnel from one to another, causing a current to flow. This is because their wave function is not strictly confined to their respective metal. However, since this wave function decays exponential with distance, the tunnel current will follow a similar dependence on distance [1]:

$$I \propto e^{\Delta z / z_0} \tag{3.1}$$

Here Δz is the height between the two metals and z_0 is a decay length that depends on the tunnel barrier height for vacuum and the work functions of both electrodes. As a rule thumb, for two metal objects this comes down to one order of magnitude increase

in current for every Å distance closer. This extreme sensitivity requires extreme vibrational isolation, but also lends itself to extreme resolution. In order to sustain a current, a bias voltage V_{bias} needs to be applied between tip and sample. As shown in Figure 3.1a this raises the Fermi level of one electrode, allowing for a net flow between both. Notice that due to the a finite temperature T the energy distribution of conduction electrons follows a Fermi-Dirac distribution, where k_B is the Boltzmann constant. Hence, in order to study atomic structures on the surface with energy levels only several meV apart, an extremely low temperature is required. If an adatom is placed in between electrons, discrete energy levels become available which severely affects the tunneling, as shown in section 3.3. Through a feedback loop one can adjust the tip height such that a constant current is achieved. By scanning the tip across the surface, images can be constructed like in Figure 3.1b. Such topographies do not show the exact height of the surface, since the tunneling current is dependent also on the local conductance of the sample, which can be different depending on the voltage and substrate.

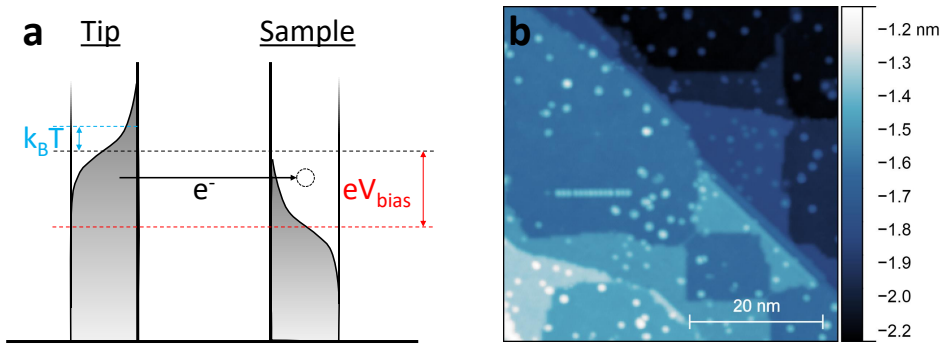

Figure 3.1: Tunnelling principle and topography. **(a)** Density of states (DOS) of a metallic tip and sample are shown in the gray shaded areas. Aside from the thermal broadening due to temperature T the DOS is assumed to be homogeneous. The gap between them represents the vacuum. The Fermi level of both are offset by a bias voltage V_{bias}. Both tip and sample are at a finite temperature T causing the Fermi-Dirac distribution to exhibit a smooth curve instead of a step edge at the Fermi level. An electron is shown to tunnel from the tip to an unoccupied state in the sample. **(b)** Topographic image made with an STM. Shown are individual atoms (circular) on top of Cu_2N and on top of Cu(100). Visible are various terraces. Shown is also a spinwave detector used in Chapter 5.

During my PhD I have worked with three different STMs: SPECS' JT, UNISOKU's USM-1300 ^{3}He and QNS's home-built Eve [2]. All three use liquid helium in a large cryostat to cool the STM to ~ 4 K and subsequently cool to ~ 1.3 K through the Joule-Thomson effect [3]. This technique requires an impedance between high-pressure He gas on one end, and liquefying low pressure He gas on the other. In case of the USM-1300 the impedance can be finely tuned. Furthermore, that STM uses ^{3}He gas in a closed circuit to cool down further to ~ 300 mK with a hold time of 24 – 48 h. Meanwhile the JT uses liquid nitrogen to slow down the helium exhaust from the large cryostat. The maximum fields that can be applied by the three STMs are $\mathbf{B}_{\text{JT}} = [0,0,3]$ T, $\mathbf{B}_{^3\text{He}} = [2,0,9]$ T and $\mathbf{B}_{\text{Eve}} \approx [6,0,4]$ T where the field in $\hat{x}$ implies an in-plane magnetic field and $\hat{z}$ implies

an out-of-plane magnetic field.

Each STM is equipped with a preamplifier which is typically mounted just outside the cryostat and used to upscale the current signals in order to reach the computer without losing signal-to-noise ratio. The gains range from 10^9 to 10^{11} with larger gains operating at lower frequencies. The operating frequency of the preamplifier is an important limitation on the following measuring techniques. It is also possible to incorporate the preamplifier into the cryostat in order to not amplify the noise resulting from high temperature cables [4].

We will now explore three techniques: IETS, Pump and Probe and ESR, which are all important not only for the context of this thesis, but for the field of atomic STM as a whole.

3.3. INELASTIC ELECTRON TUNNELING SPECTROSCOPY

Information Card

IETS

Purpose: Spectroscopy
Publication: Stipe et al. [5]
Hardware: Lock-in
Sample: all

3.3.1. INTRODUCTION

Inelastic electron tunneling microscopy, or IETS, has its roots in 1966 when it was used to study molecular vibrational modes [6]. Back then 10^9 bonds were measured at the same time. In 1998 the technique was implemented in conjunction with STM to measure a single molecule's vibrational mode [5]. The first time it was used to study spins of individuals atoms was in 2004 where individual magnese atoms were probed [7, 8]. The technique is actually the application of scanning tunneling spectroscopy (STS) in the situation where an inelastic scattering happens. In general, STS is used to measure the local DOS (LDOS). In its most basic form, this is done by taking the derivative of an I,V-curve. However, through the use of a lock-in amplifier, the signal-to-noise ratio can be enhanced significantly. The lock-in amplifier sends an oscillating V_{AC} on top of the tunneling V_{DC} to probe the slope of the I,V curve around V_{DC}.

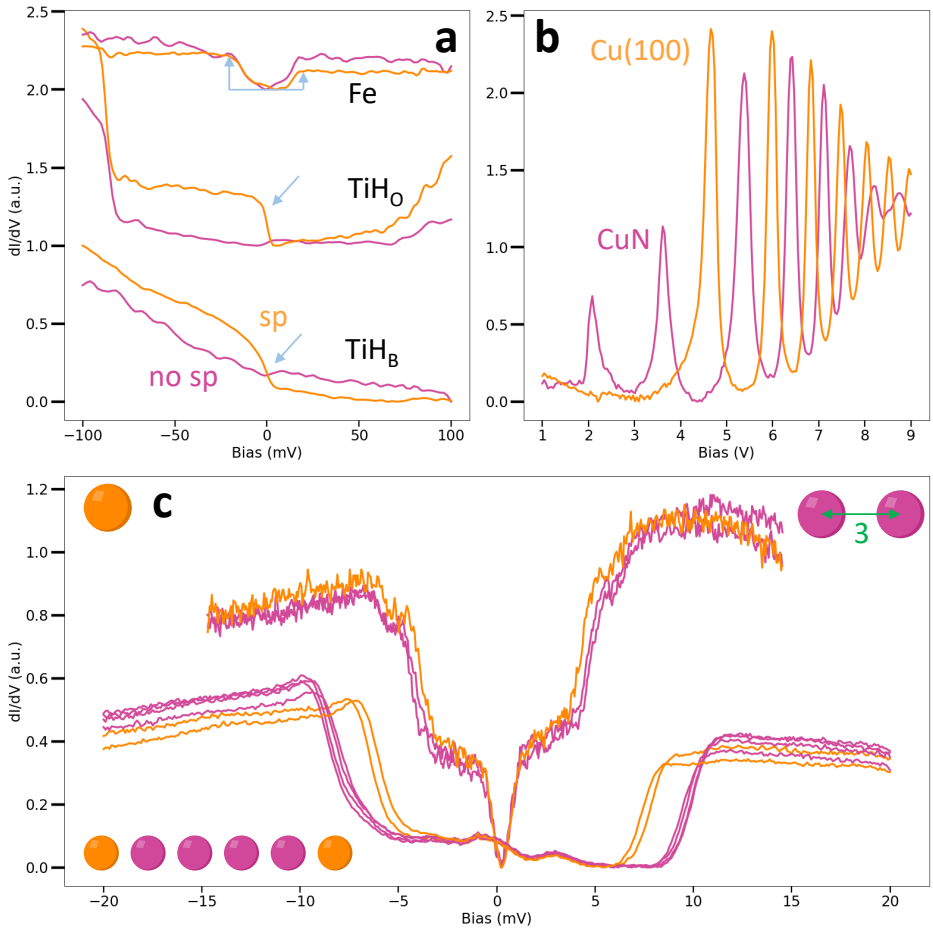

Figure 3.2: Applications of IETS (a) Identification of various elements on specific binding sites of MgO/Ag(100) with (orange) and without (magenta) a spin-polarized tip. Successive spectra are shifted by +1 a.u. for clarity and showcase TiH on a Bridge binding site, TiH on an Oxygen binding site and Fe. Blue arrows indicate spin polarized fingerprint. For all spectrum started after regulating at 100 pA, 100 mV with V_{AC} = 1 mV, T = 1.3 K. **(b)** Field emission resonances of CuN and Cu(100) using constant-current mode at I = 20 pA with V_{AC} = 100 mV, T = 1.3 K. **(c)** Spectra taken on an Fe monomer (orange) and a (3,0)-spaced dimer (magenta), in orange and magenta, respectively ($G = 5 \cdot 10^{-8}$ S, T = 0.35 K, B_Z = 1 T). Below are shown six spectra taken on an Fe_6 chain, with the outer atoms in orange, and the inner atoms in magenta. Data taken after regulating at 2 nA, 20 mV with V_{AC} = 500 μV, T = 1.3 K.

3.3.2. KEY POINTS

IETS spectra, or STS spectra in general, provide valuable information. Figure 3.2a shows how they can be used to identify elements and binding sites of adatoms or even whether the tip is spin-polarized (sp). From top the bottom, it shows Fe with and without sp, where the former has assymetric step sizes, TiH_O with and without sp, where the former shows a step around 0 mV and TiH_B with and without sp, where the former has a step

around 0 mV as well [9]. Also for identification purposes the detection of field emission resonances (FER) is as shown in Figure 3.2b to illustrate how it can be used to identify surfaces and substrates. While this technically does not fall within the scope of IETS as there are no inelastic tunneling channels, the method (scanning tunneling spectroscopy, or STS) is the same. In Figure 3.2c the method is used to deduce the coupling strength of a (3,0)-spaced dimer (top magenta) by comparing it with a lone Fe atom on CuN (orange). Fitting these spectra yields $J' \approx -0.05$ meV using the methods described in [10]. This value is used in Chapter 5. The same figure also shows six spectra on Fe_6 below, with the outer atoms in orange having a step at a lower voltage compared to the inner atoms in magenta.

3.3.3. PHYSICS

To first order, many of the findings of IETS can be described according to Figure 3.3 (left). Shown is an electron tunneling from the tip to the sample, similar to Figure 3.1a. This time, however, two tunneling paths are shown. An elastic path and an inelastic path in which energy is lost to the structure, an adatom in this case. This second channel is only available when the voltage is high enough to provide the tunneling electrons with enough energy to give to the adatom. Thus at certain voltages the conductance increases, which appears as steps in IETS measurements, as shown in Figure 3.2c. With the DOS being distributed around the Fermi energy with a variance determined by the temperature T these steps may be more or less broadened. However, this model fails to explain the large inelastic signals measured on, for example Fe on $Cu_2N/Cu(100)$ [11]. If we introduce the possibilities of virtual states to exist during the tunneling process in a cotunneling process, more experimental findings can be accounted for. This is shown in the inset of Figure 3.3 (right). In the initial state an electron at a higher energy (due to V_{bias}) had enough energy to perform an elastic (E) and inelastic (IE) tunneling event, as its excess energy exceeds the excitation energy $\Delta E_{0,1}$. In the process the electron enters the adatom, inducing a large charging energy U. This is allowed as long as $\sigma_E \sigma_t \leq \hbar/2$. The electron then hops off, either with or without raising the level of the other electron present. The inset of the diagram assumes $T = 0$ K for simplicity.

The result is steps in the IETS spectra at eV_{bias} coinciding with the energy differences between the states. These steps are the results of a larger conductance as more tunnelling paths have opened. As shown in Chapter 2, there is an additional requirement of spin selectivity: to first order only states that have $\Delta m_s = \pm 1$ are accessible, as Equation 2.5 must be finite.

3.3.4. IMPLEMENTATION

There are two methods to measure IETS, which both follow the same implementation as STS in general. For this reason, Figure 3.2 contains an example of STS which is not IETS. As explained in Section 3.3.3 the opening of additional tunnelling paths induces sudden increases in the conductance when sweeping V_{bias}. One can simply measure an I,V-curve and take the derivative to find dI/dV and locate steps in this. However, there is substantial noise in the I, V-curve both in I and in V_{bias}. Therefore the second method is much preferred. This involves a lock-in amplifier.

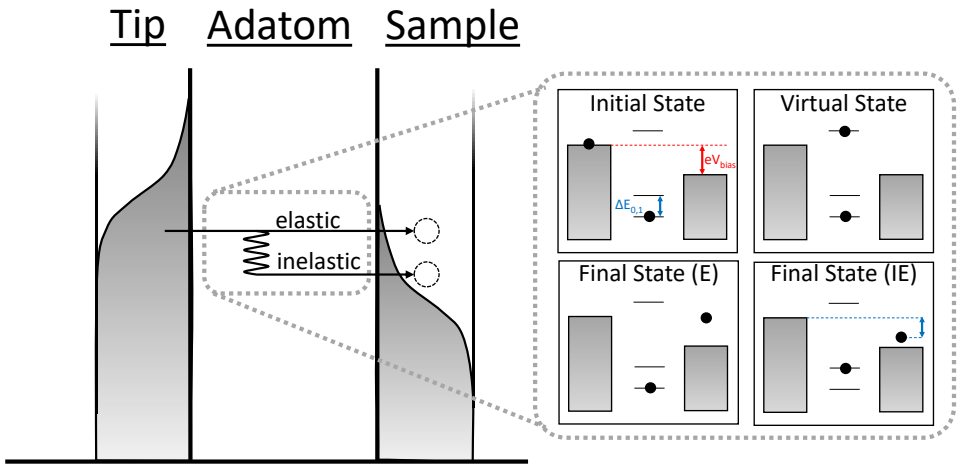

Figure 3.3: Co-tunneling process during IETS Tunneling is shown to happen elastically or inelastically. The inset shows that both are mediated through a virtual state where the tunneling electron is added to the adatom. In the elastic case this electron continues to the sample without any further interaction with the adatom. In the inelastic case the state of the adatom is lifted as the tunneling electron loses some of its energy. Note that in the inset the DOS of tip and sample are assumed to not be adjusted by temperature, but there is an difference in Fermi level due to bias voltage V_{bias}.

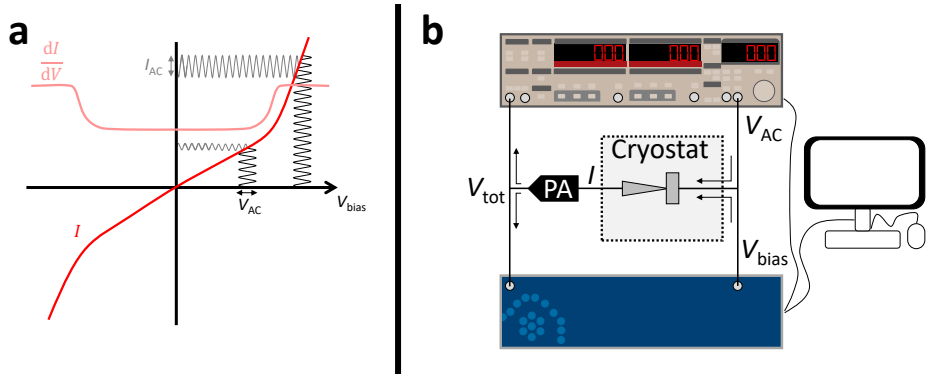

Figure 3.4: Lock-in measurement of IETS (a) An I,V-curve probed by V_{AC} yielding I_{AC} which is a measure for $\frac{\text{d}I}{\text{d}V}$. **(b)** Set-up for a lock-in measurement of IETS. A lock-in amplifier provides V_{AC} which is added on top of the V_{DC} provided by the STM operating system (e.g. Nanonis). The sum of both signals is sent to the tip-sample junction in the cryostat. The resulting current, is turned into a voltage through the preamplifier ("PA") and subsequently sent back to both the lock-in amplifier and STM operating system. Both of these machines are connected to the computer for the user to control and interpret.

Figure 3.4a shows how an I,V-curve (red) can be turned into a $^{\text{d}I}/_{\text{d}V}$-curve (salmon) through application of an oscillating V_{AC} at all values of V_{bias}. The resulting amplitude of I_{AC} is determined by the slope of the I,V-curve and is recorded. A kink in the slope

of the I, V-curve due to an increased conductance and is thus translated as a step in the lock-in signal.

To reduce noise on I_{AC} a lock-in amplifier relies on the orthogonality of sinusoidal waves. Both the STM operating system Nanonis and externals lock-in amplifiers (e.g. Stanford Research SR830 or Zurich Instruments HF2LI) can be used, with the later typically providing higher resolution and better signal-to-noise. Figure 3.4b shows how they provide a V_{AC} that is added on top of the DC V_{bias} to be sent to the tip-sample junction. The frequency of V_{AC}, also known as the lock-in frequency f_{LI} is typically high enough to avoid substantial $^1/_f$-noise [12], but low enough to stay within the operating range of the preamplifier. One must also take care of avoiding other noise sources such as resonance frequencies of certain mechanical parts of the system or 50 or 60 Hz noise (and its higher harmonics). The resulting current will be be of the form $I_{tot} = I_{DC} + I_{AC} + I_{noise}$ where I_{DC} is used to maintain a stable tunnel current, I_{AC} is the result of V_{AC} acting on the system and I_{noise} is the sum of all noises, all of which are turned into a voltage through the preamplifier. The last term will consist of noise at many different frequencies, but is assumed to be small at f_{LI} specifically. The signal is then sent to the lock-in amplifier where it is multiplied by V_{LI} operating also at f_{LI} and integrated over time. Following the orthogonality of I_{noise} with f_{LI} (except for the noise at f_{LI} itself), the resulting signal is a good measure for I_{AC}, which in turn is a good measure for the slope of the I, V-curve.

There are certain things to consider when using this technique. First, the magnitude of V_{AC} provides a lower limit for the resolution to be obtained. One can decide to make this voltage small, but the resulting signal will also be small. To overcome this one can use longer integration times with stronger low-pass filters (internal to the lock-in amplifiers). However, one should also consider the thermal broadening to make a weighed decision on acquisition time versus resolution. Secondly, while the output current I may be subject to excellent filtering techniques inherent to the lock-in, the supplied $V_{bias} + V_{AC}$ may have an additional V_{noise} which can put unintentional resolution limits.

The lock-in amplifier is also used in the next two techniques for its excellent noise reduction.

3.4. PUMP AND PROBE

Information Card

Pump and Probe

Purpose: Lifetime measurement
Publication: Loth at al. (2010) [13]
Hardware: PG or AWG, Lock-in
Sample: all
Limit before: 1ms
Limit after: 10ns

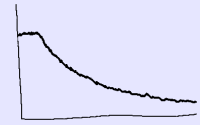

As the name suggests, in a Pump and Probe technique there are two separate entities: a pump and a probe. The technique has its origin in femtochemistry, for which the Nobel Prize in Chemistry was awarded in 1999 to Ahmed H. Zewail [14]. Its arrival to STM was done by Loth et al. in 2010 [13]. The key problem it tries to fix is reducing the disturbing effects of measurements and overcoming the low bandwidth of the preamplifier. The pump brings a system in an excited state, through whatever means is relevant for the technique. In the case of femtochemistry this is a laser pulse and in the case of STM this is a voltage pulse. Since the relaxation time may be affected by a continuous measurement, a separate probe pulse is sent some time later. The delay time between the pump and pulse allows the system to evolve without interference. It is therefore this delay time that is typically swept.

3.4.1. KEY RESULTS

Through this technique it is possible to probe relaxation times well beyond the limit of the preamplifier without losing the spatial resolution of the STM. In its original implementation, the lifetime of Fe-Cu dimers on $Cu_2N/Cu(100)$ was found to be around 100 ns and dependent on magnetic field. The technique has also been used to find the lifetime of the first excited state of an Fe_3-chain (trimer) on $Cu_2N/Cu(100)$ subject to a magnetic field B_z to be a couple of μs [15]. It has been used to determine the coupling between a magnetic nanobit and a similar trimer at various distances [16]. The technique has been used to study the effect of decoupling layer thickness on spin lifetime [17], and it has been to used to corroborate the findings of the first ESR-STM paper [18]. Subsequent ESR-STM experiments build upon this technique by implementing radio frequency signals for pulses, which results in, for example, Hahn-Echo experiments [19, 20] or use its base technique to measure coherent evolution after excitating a spin-$^1/_2$-dimer [21].

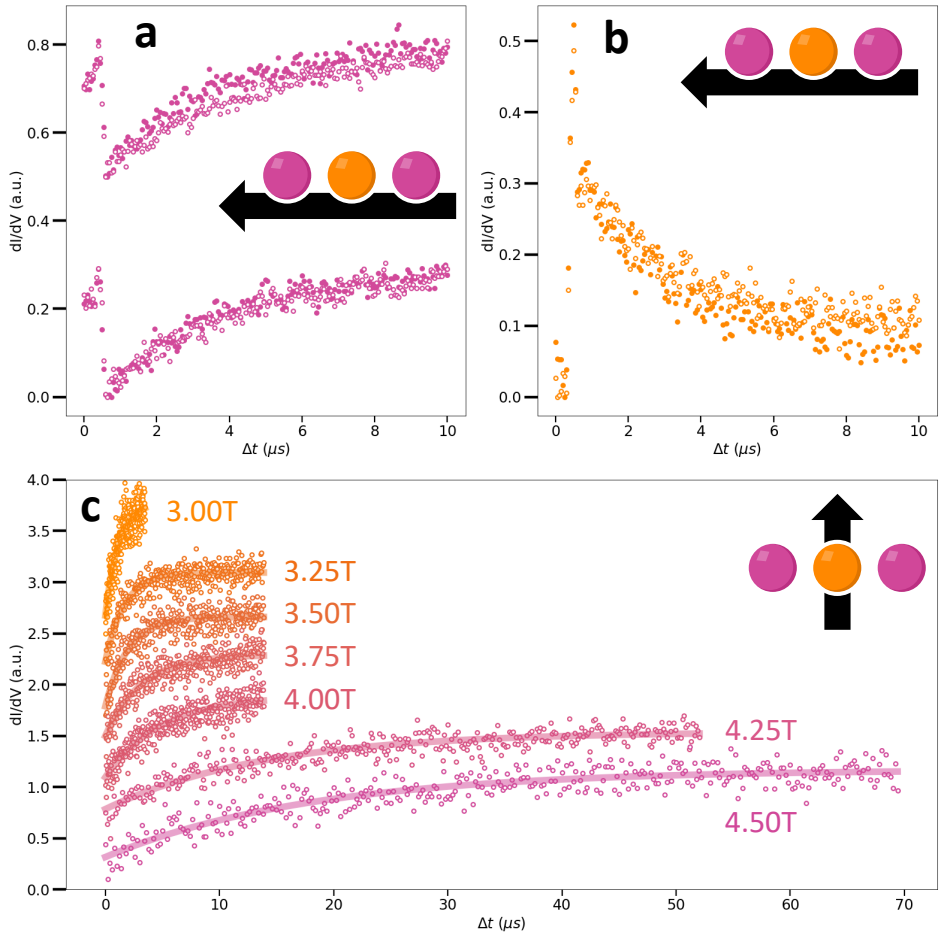

Figure 3.5: Pump and Probe data (a) Data on atoms A and C (offset up) of the two trimers on a "383" structure. Closed circles corresponds to left trimer (input lead), open circles correspond to the right trimer (reset lead). Average lifetime corresponds to 2.88 ± 2.65 μs and 3.53 ± 2.45 μs for atoms A and C, respectively. **(b)** Same as panel **a**, but for atom B with average lifetime of $2.77 \pm 2.44 \mu$s. All data taken after the tip was regulating at 12 mV, 1 nA with $V_{\text{pump}} = 20$ mV and $V_{\text{probe}} = 5$ mV and $B = 1$ T along the easy-axis as indicated by the arrow, $T = 1.5$ K. **(c)** Data on atom B of a lone trimer for various values of magnetic field along the hard axis, as indicated by the arrow. Lifetimes for seven field strengths in order from low to high are: 1.16 ± 0.09 μs, 1.66 ± 0.09 μs, 1.98 ± 0.11 μs, 3.15 ± 0.19 μs, 4.82 ± 0.40 μs, 14.01 ± 0.89 μs and 18.29 ± 1.026 μs. There is a magnetic field also along the easy axis at about 2% the strength as the shown field. Data taken after regulating at 10 mV, 200 pA and $V_{\text{pump}} = 35$ mV, $V_{\text{probe}} = 5$ mV. $T = 1.3$ K.

Shown in Figure 3.5a,b are pump and probe measurements on an input trimer of Chapter 5 with external field along the easy axis of the chain. We find a lifetime about twice as large as was previously reported for a one trimer [15]. We find $T_1 \approx 3$ μs. For atoms A, B and C we find $T_1^A = 2.88$ μs, $T_1^B = 2.77$ μs and $T_1^C = 3.53 \mu$s. The longer lifetime may be attributed to the presence of an octamer. We note a large uncertainty due to the number of measurements being small (see caption), but highlight that the order

of magnitude remains the same. We used $V_{\text{pump}} = 20$ mV, $V_{\text{pump}} = 5$ mV, $t_{\text{pump}} = 500$ ns.

Shown in Figure 3.5c are pump and probe measurements on atom B of a lone trimer subject to an external field along the hard axis of the chain. This data is to be put in context of Chapter 4 where the application of such a field has profound effects on the lifetime of Fe-chains on $Cu_2N/Cu(100)$. While increasing B_x does result in larger lifetimes, no peak in the lifetime is observed. We believe this is because the value of $B_x = B_{\text{diab}}$ exceeds the range available of B_x during the experiment for a trimer.

3.4.2. PHYSICS

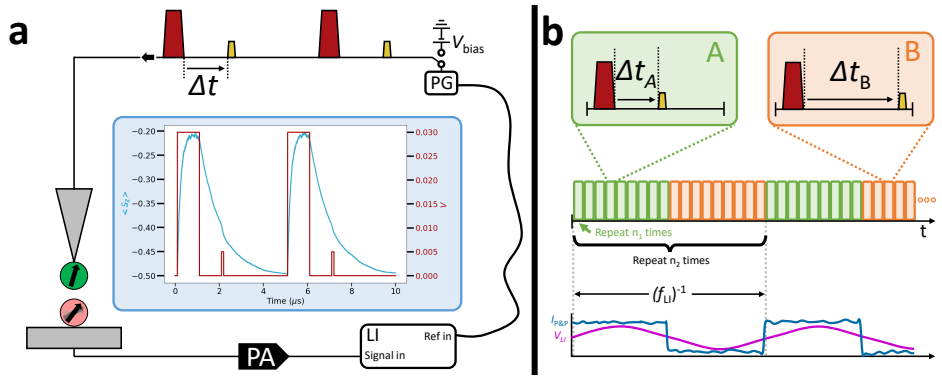

Figure 3.6: Pump and Probe measurement (a) Experimental set-up for pump probe measurements. A pulse generator (PG) sends two pulses at Δt delay, repeatedly. The first pulse is the pump pulse, the second pulse is the probe pulse. The pump induces an excitation in the adatom (salmon color). Through a spin-polarized tip (green atom) the current that is measured during the probe pulse will depend on the spin state. A time ensemble measurement takes place, as the preamplifier (PA) has a low pass filter and sends the signal to the lock-in amplifier (LI). Inset: Markov simulation, see text for more details. **(b)** The pulse generator sends two repeated cycles, A and B. They are repeated n_1 times before alternating, chosen such that $2n_1$ times the duration of a cycle fits in the lock-in time f_{LI}^{-1}. This is repeated n_2 for better signal-to-noise. The cycles A and B differ in that cycle A has a variable Δt_{A} that is swept in order to probe all delay times. Meanwhile Δt_{B} is kept constant and is longer.. Bottom: the voltage reaching the lock-in amplifier originates from a current that is higher during the repeated A cycles and lower during the repeated B cycles. This would then be multiplied by V_{LI} operating at the same frequency to enhance the difference between both cycles.

The basic principle of Pump and Probe rests on applying two pulses to the tip-sample junction, in order to probe the lifetime of the system. In this case we will consider the spin lifetime of an excited state on a hypothetical single atom, shown in salmon in Figure 3.6. The system is brought into excitation through means of the first pulse, the pump pulse where $eV_{\text{pump}} > E_{\text{exc}}$, i.e. with the pump voltage high enough to cause excitations in the system. For a two-level system this equates to $\Delta E_{0,1}$. The pump pulse is shown in red. Some delay time later, Δt to be exact, a second pulse reaches the tip-sample junction. Here $eV_{\text{probe}} < E_{\text{exc}}$ such that no excitations are performed. With a spin-polarized tip (indicated with a green apex atom) the exact current during both pulses will depend on the spin state of the system in question. During such a measurement the current during the probe pulse is compared for different delay times, which gives a measure of

the spin of the system over time. Since the lifetimes are typically much shorter than the preamplifier would pass through, the experiment is repeated thousands of times and averaged, yielding an ensemble measurement. For further signal-to-noise improvements this repeated cycle, called cycle A, will be compared with a repeated cycle B. More about this follows shortly.

We will now consider a Markov chain simulation repeated 10000 times and averaged to simulate a pump and probe ensemble measurement. The inset in Figure 3.6a shows a Markov chain simulation of a hypothetical atom, where in each time step electrons can either excite the system to $|\uparrow\rangle$, relax it to $|\downarrow\rangle$ or not interact at all. We let only one in a thousand electrons interact. We pick a spin-$^1/_2$ atom with excitation energy $\Delta E_{0,1} = 10$ meV. With $V_{\text{pump}} = 30$ mV, this is enough to excite the system, while $V_{\text{pump}} = 5$ mV can only probe the system. The tip-sample distance is such that during the pump pulse the current $I = 1$ nA, and the I,V-curve is consider linear. With time steps taken at 1 ns, this yields about 6 electrons per time step during the pump pulse from the tip, with an energy picked randomly between 0 and 30 meV. Additionally 1 electron per nanosecond is assumed to interact with the system from the bath, at 0 meV. Hence we assume $T = 0$ K. The actual number of electrons interacting with the system per time step is determined according to a Poisson distribution. The inset shows the voltage in red and the average spin value of all 10000 simulations in blue. Each simulation includes one repetition to indicate how the previous cycle does not affect the next cycle when the cycle length (chosen to be 5 μs) is long enough.

The inset shows how during the pump pulse the ensemble is brought into excitation, with $\langle S_z \rangle \rightarrow -0.20$, the weighed average based on excitations (10 ~ 30 mV) and relaxations (0 ~ 10 meV + bath electrons). Then after the pump pulse, the bath electrons slowly decay the ensemble state towards the ground state as a result of relaxations through the bath electrons. During the probe pulse the decay happens at a slightly faster rate. This simulation shows how the ensemble measurement leads to an exponential decay.

3.4.3. IMPLEMENTATION

In order to not be limited by the preamplifier, the pump and probe pulses will be sent along an A/B cycle oscillating between the two at f_{LI}. The output current, after passing the preamplifier, gets sent to a lock-in amplifier where the signal is multiplied by V_{LI}, an alternating voltage also operating at f_{LI}, resulting in a large signal-to-noise as explained in Section 3.3.4. The A cycle will contain relevant information about the spin, whereas the B cycle offers a reference signal. The lock-in amplifier will then output a value based on the difference between the A and B cycle. The cycles are shown in Figure 3.6b. The pump pulses are spaced far enough apart that one can assume the system to have fully relaxed by the time the second pump pulse arrives. In the A cycle the probe pulse is shortly after the pump pulse, measuring the spin-polarized current and thereby the spin value of the system, before it has relaxed. In the B-cycle the probe pulse is at the end of the cycle, such that the spin-polarized current corresponds to the system's ground state.

Hence the difference in current between the A and B cycle is only from the different spin value of the system. These A/B cycles are repeated until the signal-to-noise is considered sufficient, and the process is repeated with a different Δt_A between the pump and probe pulses in the A cycle.

The pulses can be generated by an arbitrary waveform generator (AWG) or a pulse generator (PG). Either way, the lock-in amplifier must be synchronized with the generator. This is done through an additional output by the generator which is fed to the lock-in amplifier as a reference.

3.5. ELECTRON SPIN RESONANCE

Information Card

Electron Spin Resonance

Purpose:	Coherent spin control
Publication:	Baumann et al.
Hardware:	RF, Lock-in, B-field
Sample:	MgO/Ag(100) (so far)
Limit before:	1meV
Limit after:	1ueV

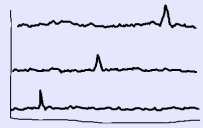

3.5.1. LARMOR PRECESSION AND ESR

Electron Spin Resonance in STM has its history in Nuclear Magnetic Resonance, first observed in 1938 [22], with the electron variant observed shortly thereafter in 1944 [23]. The first implementation in STM happened in 2015 [18], where it is applied on single atoms. In ESR-STM an oscillating voltage is applied to the tip-sample junction with a frequency equal to the Larmor frequency of an atom in a static external magnetic field. The addition of a local magnetic field gradient allows the probed atom to experience an oscillating magnetic field as the oscillating voltage pushes and pulls the atom. This causes an oscillating magnetic field at the same frequency as the Larmor frequency, subsequently allowing the atom's spin to coherently rotate. Besides the coherent control of the spin, the extreme sensitivity to the applied frequency allows for extremely fine energy sensitivity.

3.5.2. KEY RESULTS

Since the first implementation in 2015, a plethora of experiments have been performed, which can be generally differentiated by its two novelties: energy resolution and coherent spin control. In the former category, the hyperfine coupling of individual atoms is found [24], a large g-factor anisotropy has been found [25, 26], a tip's magnetic field has

been evaluated along a much larger range than previously possible [27], various coupling strengths have been quantified [28–32] and 3-dimension resonance images of single atoms have been achieved [33].

In the latter category, coherent coupling is determined [21], the nuclear polarization of single atoms is controlled [34], the spin coherence time of single atoms and dimers is enhenced [35], individual coherent control of two atoms is achieved [36] and staple quantum computing experiments such as Hahn echo is performed on individual atoms [19, 20]. It is worth mentioning that this technique has also been achieved on spin centers in molecules [37]. Until recently all spin centers were transition metal elements, such as Fe, Ti and Cu. More recently, ESR-STM is also shown to work on alkali metals [38].

Shown in Figure 3.7 is ESR data taken in the context of [2]. Panel a shows a very large peak of 3 pA. This current is the difference between an A and B cycle, in which the during the A-cycle ESR is performed and during the B-cycle no ESR is performed. The assymetric shape indicates that the difference in current between A and B cycles is not entirely due to so-called direct ESR in which the average $\langle Sz \rangle$ changes, but also due to so-called homodyne detection in which the tip is also spin-sensitive to $\langle S_x \rangle$ and/or $\langle S_y \rangle$, through which the atom is Larmor precessing [35]. This is the largest ESR peak published thus far. On the other end, panel b shows the peak published at the lowest tunneling current thus far: 800 fA. A best fit to a Fano lineshape [35] is provided. Panel c shows the linear relationship between ESR frequency and magnetic field, with the slope being determined by the g-factor. Here we find $g \approx 1.64$.

3.5.3. PHYSICS

We have previously established the Hamiltonian for a spin-½ system:

$$H_{\text{Zeeman}} = g\mu_B \mathbf{B} \cdot \mathbf{S} \tag{3.2}$$

As Joseph Larmor has shown, a spin in a magnetic field will precess around that magnetic field [39]. This is also true for the spin of an adatom, such as the spin-½ system TiH [18]. The oscillation frequency is known as the *Larmor frequency* $f_{\text{L}} = \gamma B$ where $\gamma = \frac{g\ mu_B}{\hbar}$. For the case of TiH on MgO, this amounts to about 30 GHz/T. The goal in ESR experiments is to apply an oscillating field at the same frequency as fL. Since most advanced equipment is rated up to 20-40GHz, this leads to applicable fields of ~ 1 T. For systems with larger spin, such as Fe's S = 2, a lower field is required.

Now consider a typical spin-½ particle, the electron, suspended in vacuum with a static magnetic field $\mathbf{B}_0 = B_0\hat{\mathbf{z}}$. The electron's spin will precess around the $\hat{\mathbf{z}}$-axis at f_{L}. Besides the precession, the magnetic field also causes Zeeman splitting: the splitting of the energy of the two eigenstates, see Figure 3.8. Without pertubation and at $T =$ 0 K, the electron will remain in its groundstate $|\downarrow\rangle$. Through the same mechanism that causes Larmor precession around the $\hat{\mathbf{z}}$-axis, the electron can be rotated along any other direction, by applying a magnetic field perpendicular to the plane of precession. Hence,

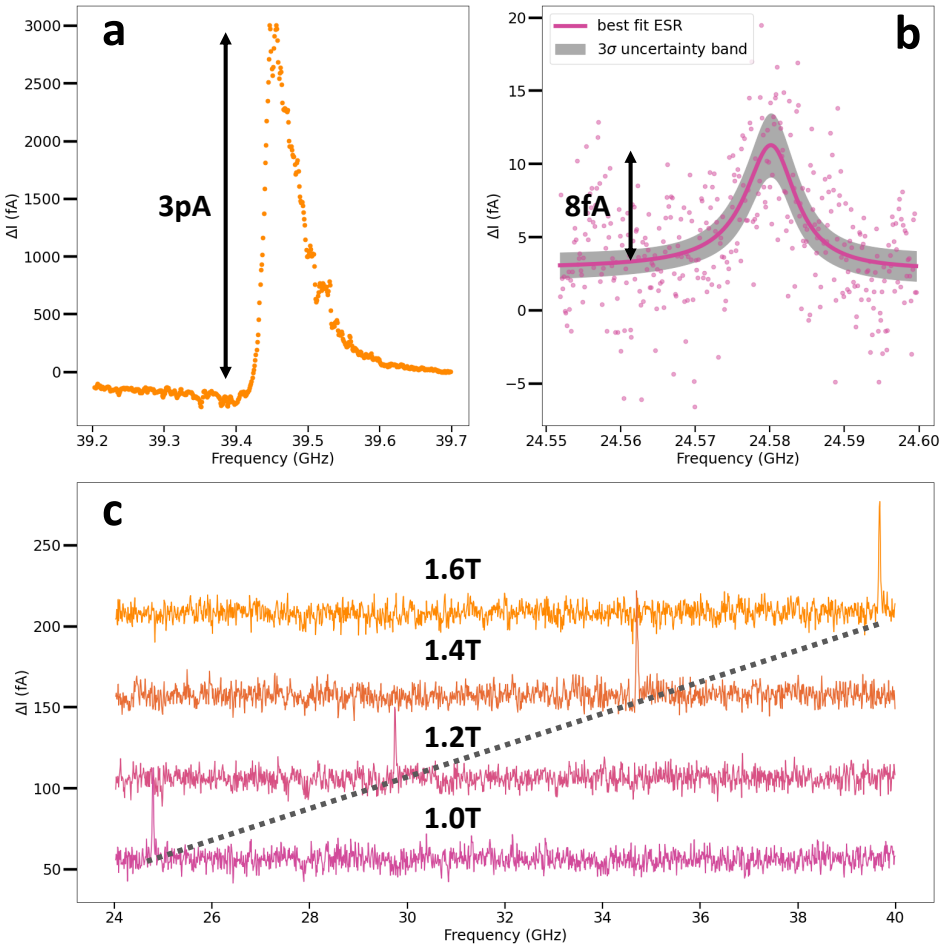

Figure 3.7: ESR data (a) Typical ESR peak with large peak height (3pA). V_{RF} = 20 mV applied to antenna, V_{DC} = 40 mV, I = 40 pA, B = 1.6 T **(b)** Very weak ESR peak with best fit. Data taken while stabilizing the tip at 800 fA, V_{DC} = 32 mV, V_{RF} = 30 mV applied to antenna, B = 1 T. **(c)** ESR peaks at increasing magnetic field, following a linear relation with the field. Subsequent traces are offset by 50 fA. V_{RF} = 20 mV applied to antenna, V_{DC} = 50 mV, I = 20 pA. All data taken at T = 1.3 K.

to bring the electron from $|\downarrow\rangle$ to $|\uparrow\rangle$, one needs a magnetic field in either the $\hat{\mathbf{x}}$- or $\hat{\mathbf{y}}$-direction. But since the electron is already precessing in this plane due to $\mathbf{B}_0$, a static field along the x,y-plane will not do. For one, such a field redefine the quantization axis, thereby keeping the electron in the newly-defined groundstate $|\downarrow'\rangle$. Secondly, even if we consider the additional field as only a pertubation, the precession direction along the z,x-plane (or z,y-plane) depends on the phase of the spin along the x,y-plane, effectively rocking the spin back and forth around $|\downarrow\rangle$. What is needed instead is an oscillating magnetic field with the oscillation frequency exactly matching the Larmor frquency due to $\mathbf{B}_0$.

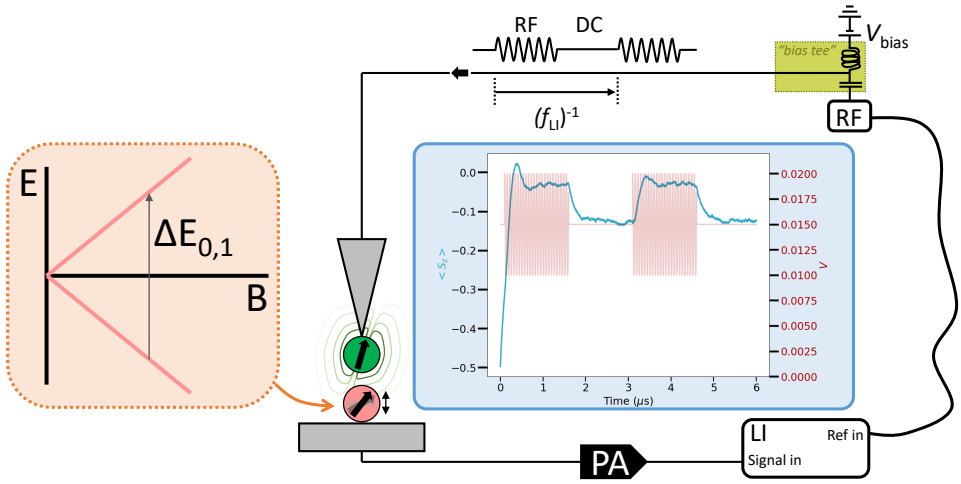

Figure 3.8: ESR measurement (a) Experimental set-up for ESR measurements. A radio frequency source (RF) sends bursts of RF voltage at a delay such that it matches the lock-in frequency f_{LI}. The RF voltage causes oscillating electrostatic fields that moves the adatom (salmon) through the tip's magnetic field gradient (shown on the green tip apex atom). Through a spin-polarized tip the current that is measured will depend on the spin state. A time ensemble measurement takes place, as the preamplifier (PA) has a low pass filter. Left inset: Two level system with Zeeman splitting as a model for the adatom. Right inset: Markov simulation, see text for more details.

To achieve this in ESR-STM, we place the spin-½ particle on a surface with a strong external magnetic field $\mathbf{B}_0$ and a local field gradient $\mathbf{B}_g = B_g(z)\hat{\mathbf{x}}$. Generally speaking the field gradient is provided by a magnetic tip apex as shown in Figure 3.8, although it is also possible to use a nearby magnetic atom on the surface [36]. Through means of oscillating electrostatic forces we oscillate the particle along the $\hat{\mathbf{z}}$-direction, thereby oscillating the value of B_g. Only when the electrostatic forces oscillate at f_L, will the spin rotate along the $\hat{\mathbf{x}}$-axis. Such a rotation is called a Rabi oscillation, and it forms the basis of most quantum computing operations. The oscillating electrostatic forces are applied through an oscillating voltage V_{RF} at the tip-sample junction, and so far only the surface MgO/Ag(100) has shown to properly mediate this into oscillatory motion. By carefully selecting the duration and intensity of V_{RF}, one can have coherent control of the spin. Due to the extreme sensitivity of this technique on the frequency f_{L}, which corresponds to an energy, ESR-STM gives unprecedented energy resolution.

As before, we will consider again a Markov Chain. This time, instead of only considering the two states $\langle\uparrow\rangle$ and $\langle\downarrow\rangle$, we will consider the latitude angle ϕ on the Bloch sphere spanned by those two states. In the simulation, to be repeated 10000 times, the system starts in $\phi = 0$, indicating $\langle\downarrow\rangle$. With a $eV_{\mathrm{DC}} = 15$ meV being larger than $\Delta E_{0,1} = 10$ meV, throughout the entire simulation there will excitations and relaxations happening, according to the same statistics as described in section 3.4. During the time that an additional $V_{\mathrm{RF}} = 5$ mV is applied, every timestep Δt, the angle is rotated by $\Delta\phi$ (equal to $\frac{\mathrm{rad}}{100}$).

During the averaging of the 10000 simulations, the value $\cos\phi$ is used to determine $\langle S_z \rangle$. Figure 3.8 shows the results in the right inset.

With the state being initialized at $\langle\downarrow\rangle$, the average value $\langle S_z \rangle$ increases rapidly to a steady state around -0.05. It first overshoots, as the likelihood of an excitation or relaxation having happened at this point is not large enough. Once the RF voltage is turned off, at 1.5 μs, the ensemble system decays to another steady state around -0.1. The difference between the two is explained by the RF voltage bringing the average value closer to exactly 0. During the actual ESR experiment this RF on/RF off is repeated many times and the difference between the two is measured through a lock-in amplifier. It therefore also essential that the population distribution between the two states does not start close to 50:50, which would happen if the temperature is too high.

3.5.4. IMPLEMENTATION

The implementation of ESR-STM is the most expensive out of experimental methods listed here. Not only does it require RF cabling down to the STM-head, but for most ESR-purposes an RF-generator of several tens of GHz is required (or AWG with similar options). The most basic ESR-STM signal scheme is called Continuous Wave (CW), and makes use of an RF-generator and a lock-in amplifier. More advanced techniques include double resonance, phase control and RF pulses which all require an IQ-mixer. Here we will discuss only CW. A brief overview will follow, but for a more in-depth implementation see Chapter 6.

Figure 3.8 shows that an RF generator's signal and the V_{bias} are combined through "bias tee". The RF generator also sends a reference signal to the lock-in amplifier for synchronization. Since the cabling to the tip-sample junction is lossy for signals in the GHz-range, a transfer function needs to be established. One way of doing this is by taking an IETS measurement along a step with and without an RF voltage added and comparing how much the step is smoothed out, at each required frequency [40]. The smoothing out would be the result of an additionally large oscillating voltage as shown in Figure 3.4a. The transfer function is limited by the cabling, and oftentimes one would have to install specific cables for this end. The cabling can be lead straight to the tip of the tip-sample junction, or to an antenna close to the junction as is done in Chapter 6. As described with the Markov Chains before, the RF signal is turned on and off at the lock-in frequency and the difference in average spin-polarized current is compared between the two through the lock-in amplifier that must operate at a frequency lower than the cut-off frequency of the preamplifier.

Based on the temperature of the system, one can determine what Zeeman energy is required to bring the population of the two states one is investigating far enough away from 50:50 in order to get a sizeable lock-in signal. This, then, determines both the required magnetic field and RF frequency. For example, most STMs operate around 1.5 K. For the population distribution to be at least 40:60, the required frequency would be 12.5 GHz. Alternatively one operates ESR-STM at lower temperatures [41].

BIBLIOGRAPHY

1. Binnig, G. & Rohrer, H. Scanning tunneling microscopy. *Surface Science* **152-153,** 17–26. ISSN: 0039-6028. https://doi.org/10.1016/0039-6028(85)90120-7 (1985).
2. Hwang, J. *et al.* Development of a scanning tunneling microscope for variable temperature electron spin resonance. *Review of Scientific Instruments* **93,** 093703. https://doi.org/10.1063/5.0096081 (2022).
3. Zhang, L., Miyamachi, T., Tomanić, T., Dehm, R. & Wulfhekel, W. A compact sub-Kelvin ultrahigh vacuum scanning tunneling microscope with high energy resolution and high stability. *Review of Scientific Instruments* **82,** 103702. https://doi.org/10.1063/1.3646468 (2011).
4. Birk, H., Oostveen, K. & Schönenberger, C. Preamplifier for electric-current noise measurements at low temperatures. *Review of Scientific Instruments* **67,** 2977–2980. https://doi.org/10.1063/1.1147083 (1996).
5. Stipe, B. C., Rezaei, M. A. & Ho, W. Single-Molecule Vibrational Spectroscopy and Microscopy. *Science* **280,** 1732–1735. https://doi.org/10.1126/science.280.5370.1732 (1998).
6. Jaklevic, R. C. & Lambe, J. Molecular Vibration Spectra by Electron Tunneling. *Phys. Rev. Lett.* **17,** 1139–1140. https://doi.org/10.1103/PhysRevLett.17.1139 (22 Nov. 1966).
7. Heinrich, A. J., Gupta, J. A., Lutz, C. P. & Eigler, D. M. Single-Atom Spin-Flip Spectroscopy. *Science* **306,** 466–469. https://doi.org/10.1126/science.1101077 (2004).
8. You, S., Lü, J.-T., Guo, J. & Jiang, Y. Recent advances in inelastic electron tunneling spectroscopy. *Advances in Physics: X* **2,** 907–936. https://doi.org/10.1080/23746149.2017.1372215 (2017).
9. Chen, Y., Bae, Y. & Heinrich, A. J. Harnessing the Quantum Behavior of Spins on Surfaces. *Advanced Materials* **n/a,** 2107534. https://doi.org/10.1002/adma.202107534.
10. Ternes, M. Spin excitations and correlations in scanning tunneling spectroscopy. *New Journal of Physics* **17,** 063016. https://doi.org/10.1088/1367-2630/17/6/063016 (June 2015).
11. Delgado, F. & Fernández-Rossier, J. Cotunneling theory of atomic spin inelastic electron tunneling spectroscopy. *Phys. Rev. B* **84,** 045439. https://www.doi.org/10.1103/PhysRevB.84.045439 (4 July 2011).

12. Bordoni, F., De Gasperis, G. & Ferri, G. 1/f noise of STM tunnel probe as a function of temperature. *AIP Conference Proceedings* **285,** 491–494. https://doi.org/10.1063/1.44643 (1993).

13. Loth, S., Etzkorn, M., Lutz, C. P., Eigler, D. M. & Heinrich, A. J. Measurement of Fast Electron Spin Relaxation Times with Atomic Resolution. *Science* **329,** 1628–1630. https://doi.org/10.1126/science.1191688 (2010).

14. Zewail, A. H. Laser Femtochemistry. *Science* **242,** 1645–1653. https://doi.org/10.1126/science.242.4886.1645 (1988).

15. Yan, S., Choi, D.-J., Burgess, J. A. J., Rolf-Pissarczyk, S. & Loth, S. Control of quantum magnets by atomic exchange bias. *Nature Nanotechnology* **10,** 40. https://www.doi.org/10.1038/nnano.2014.281 (Dec. 2014).

16. Yan, S. *et al.* Nonlocally sensing the magnetic states of nanoscale antiferromagnets with an atomic spin sensor. *Science Advances* **3.** https://doi.org/10.1126/sciadv.1603137 (2017).

17. Paul, W. *et al.* Control of the millisecond spin lifetime of an electrically probed atom. *Nature Physics* **13,** 403–407. ISSN: 1745-2481. https://doi.org/10.1038/nphys3965 (Apr. 2017).

18. Baumann, S. *et al.* Electron paramagnetic resonance of individual atoms on a surface. *Science* **350,** 417–420. https://doi.org/10.1126/science.aac8703 (2015).

19. Yang, K. *et al.* Coherent spin manipulation of individual atoms on a surface. *Science* **366,** 509–512. https://doi.org/10.1126/science.aay6779 (2019).

20. Willke, P. *et al.* Coherent Spin Control of Single Molecules on a Surface. *ACS Nano* **15,** 17959–17965. ISSN: 1936-0851. https://doi.org/10.1021/acsnano.1c06394 (Nov. 2021).

21. Veldman, L. M. *et al.* Free coherent evolution of a coupled atomic spin system initialized by electron scattering. *Science* **372,** 964–968. https://doi.org/10.1126/science.abg8223 (2021).

22. Rabi, I. I., Zacharias, J. R., Millman, S. & Kusch, P. A New Method of Measuring Nuclear Magnetic Moment. *Phys. Rev.* **53,** 318–318. https://doi.org/10.1103/PhysRev.53.318 (4 Feb. 1938).

23. Zavoisky, E. Spin-magnetic resonance in paramagnetics. *J Phys Ussr* **9,** 211–245 (1945).

24. Willke, P. *et al.* Hyperfine interaction of individual atoms on a surface. *Science* **362,** 336–339. https://doi.org/10.1126/science.aat7047 (2018).

25. Steinbrecher, M. *et al.* Quantifying the interplay between fine structure and geometry of an individual molecule on a surface. *Phys. Rev. B* **103,** 155405. https://doi.org/10.1103/PhysRevB.103.155405 (15 Apr. 2021).

26. Kim, J. *et al.* Spin resonance amplitude and frequency of a single atom on a surface in a vector magnetic field. *Phys. Rev. B* **104,** 174408. https://doi.org/10.1103/PhysRevB.104.174408 (17 Nov. 2021).

27. Yang, K. *et al.* Tuning the Exchange Bias on a Single Atom from 1 mT to 10 T. *Phys. Rev. Lett.* **122,** 227203. https://doi.org/10.1103/PhysRevLett.122.227203 (22 June 2019).

28. Yang, K. *et al.* Engineering the Eigenstates of Coupled Spin-1/2 Atoms on a Surface. *Phys. Rev. Lett.* **119,** 227206. https://doi.org/10.1103/PhysRevLett.119.227206 (22 Nov. 2017).

29. Choi, T., Lutz, C. P. & Heinrich, A. J. Studies of magnetic dipolar interaction between individual atoms using ESR-STM. *Current Applied Physics* **17,** 1513–1517. ISSN: 1567-1739. https://doi.org/10.1016/j.cap.2017.08.011 (2017).

30. Choi, T. *et al.* Atomic-scale sensing of the magnetic dipolar field from single atoms. *Nature Nanotechnology* **12,** 420–424. ISSN: 1748-3395. https://doi.org/10.1038/nnano.2017.18 (May 2017).

31. Natterer, F. D. *et al.* Reading and writing single-atom magnets. *Nature* **543,** 226–228. ISSN: 1476-4687. https://doi.org/10.1038/nature21371 (Mar. 2017).

32. Yang, K. *et al.* Probing resonating valence bond states in artificial quantum magnets. *Nature Communications* **12,** 993. ISSN: 2041-1723. https://doi.org/10.1038/s41467-021-21274-5 (Feb. 2021).

33. Willke, P., Yang, K., Bae, Y., Heinrich, A. J. & Lutz, C. P. Magnetic resonance imaging of single atoms on a surface. *Nature Physics* **15,** 1005–1010. ISSN: 1745-2481. https://doi.org/10.1038/s41567-019-0573-x (Oct. 2019).

34. Yang, K. *et al.* Electrically controlled nuclear polarization of individual atoms. *Nature Nanotechnology* **13,** 1120–1125. ISSN: 1748-3395. https://doi.org/10.1038/s41565-018-0296-7 (Dec. 2018).

35. Bae, Y. *et al.* Enhanced quantum coherence in exchange coupled spins via singlet-triplet transitions. *Science Advances* **4,** eaau4159. https://doi.org/10.1126/sciadv.aau4159 (2018).

36. Phark, S.-H. *et al. Double Electron Spin Resonance of Engineered Atomic Structures on a Surface* 2021. https://arxiv.org/abs/2108.09880.

37. Zhang, X. *et al.* Electron spin resonance of single iron phthalocyanine molecules and role of their non-localized spins in magnetic interactions. *Nature Chemistry* **14,** 59–65. ISSN: 1755-4349. https://doi.org/10.1038/s41557-021-00827-7 (Jan. 2022).

38. Kovarik, S. *et al.* Electron Paramagnetic Resonance of Alkali Metal Atoms and Dimers on Ultrathin MgO. *Nano Letters* **22,** 4176–4181. ISSN: 1530-6984. https://doi.org/10.1021/acs.nanolett.2c00980 (May 2022).

39. Feynman Richard P. (Richard Phillips), 1.-1. *The Feynman lectures on physics, Volume 2, 34-5* Vol. 2 has subtitle: The electromagnetic field; 3 has subtitle: Quantum mechanics.;Includes bibliographical references and indexes. https://search.library.wisc.edu/catalog/999468136802121 (Reading, Mass. : Addison-Wesley Pub. Co., c1963-1965., 1965 c1963).

40. Paul, W., Baumann, S., Lutz, C. P. & Heinrich, A. J. Generation of constant-amplitude radio-frequency sweeps at a tunnel junction for spin resonance STM. *Review of Scientific Instruments* **87,** 074703. https://doi.org/10.1063/1.4955446 (2016).

41. Van Weerdenburg, W. M. J. *et al.* A scanning tunneling microscope capable of electron spin resonance and pump–probe spectroscopy at mK temperature and in vector magnetic field. *Review of Scientific Instruments* **92,** 033906. https://doi.org/10.1063/5.0040011 (2021).

4

LIFETIME ENHANCEMENT NEAR A DIABOLIC POINT

One of the important quantities in computing technology, both classical and quantum, is the lifetime T^S of magnetic states. For atomic structures on surfaces, these are limited various sources. For example, the coupling with the environment, which can be overcome by placing the atomic structure on a decoupling layer [1–5] or by utilize nuclear spins [6]. The structure may also lack of large energy barriers which can be lifted through magnetic anisotropy [7–10], strong magnetic fields [11] or exchange fields [12] and hybridization of classical states. Another cause of limitation is hybridization of states, for which one would want to purify the states. Here we show an example of the latter by crossing a diabolic point, through application of a strong field along the hard-axis of an Fe_N-chain on Cu_2N/Cu(100). We show that this diabolic point can be measured on each individual atom, and can enhance the lifetime by more than two orders of magnitude and further show that these atoms are subject to minute changes of the g-factor along the chain.

Many physical phenomena where sudden order of magnitude changes happen for small variations in the input parameters are known as phase transitions. In these scenarios there are two regimes with a clear border or transition regime and a monotonic variation between the two regimes. A diabolic point is fundamentally different in that the behaviour is singular. The name, coined by Berry et al. [13] from the toy *diabolo*, refers to the double-cone shape of the energies of two states along a 2-dimensional parameter space, as shown in Figure 2.13. Many studies involving these points have been performed in the field of optics [14, 15] where the degeneracy of eigenstates at this point is used. In the field of condensed matter physics, of particular importance are studies on molecular nanomagnets [16–20].

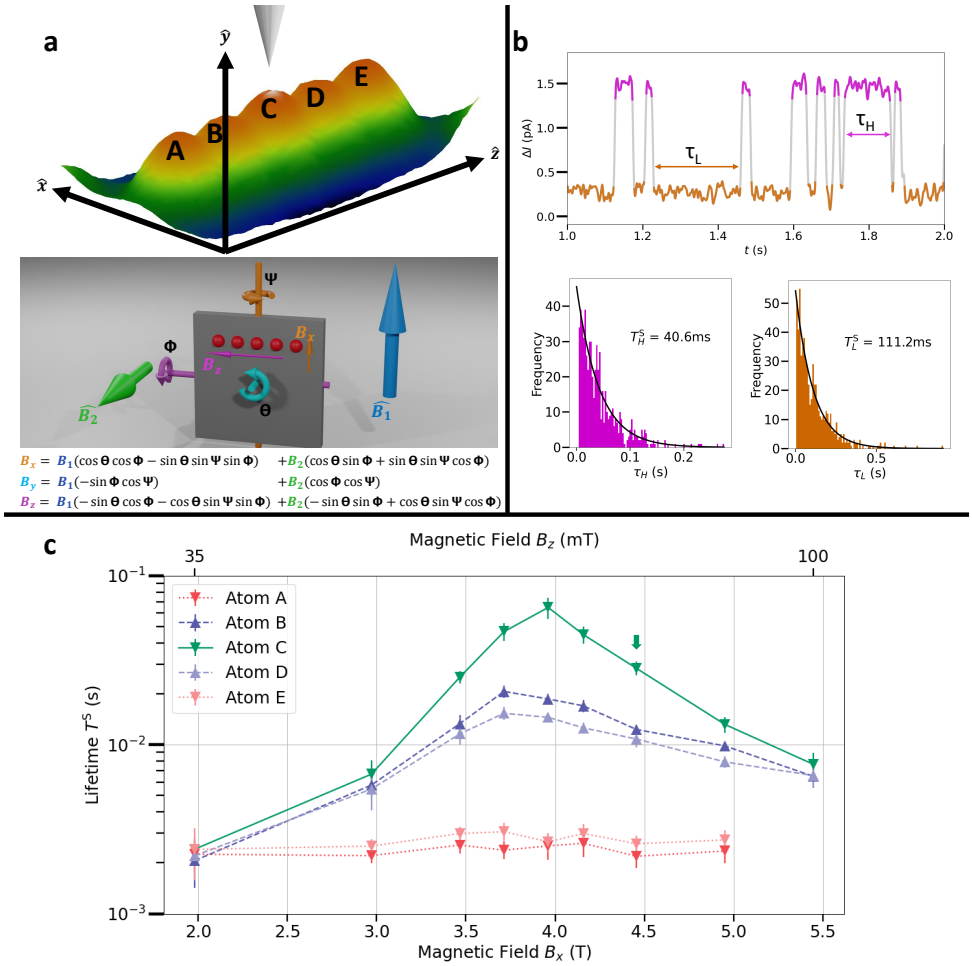

Figure 4.1: Experimental Design for diabolic point measurement. **(a)** Topographic rendering of a constant-current map on Fe_5 with its spin axes defined and the atoms labeled A-E. An STM tip is shown for illustrative purposes. Shown below are the three relevant angles Θ, Ψ and Φ that define how the two external magnets B_1 and B_2 contribute to the magnetic field along the structure's axes B_x, B_z and (not shown) B_y. The equations are derived using Euler rotations in which subsequently Φ, Ψ and Θ are rotated. **(b)** (top) A section of a constant-height time trace taken on the Fe_5. A spin-polarized tip reveals two spin states (H and L, red and blue respectively). The duration spent in either state is called τ with an adequate subscript. (bottom) Histograms of τ_H and τ_L, fit to an exponential function to get lifetimes T_H^S and T_L^S, respectively. The sum $(T^S)^{-1} = (T_H^S)^{-1} + (T_L^S)^{-1}$ is used for the data in **c**. **(c)** Lifetime measured according to **b** for all five atoms of Fe_5, for various magnetic fields B_x. Due to the angles indicated in panel **a**, the additional field B_z is shown on the top axis. Lines are guide to the eye. Error bars are 2σ. The data in panel **b** appears in panel **c** as atom C at $B_x = 4.5$ T, indicated with the arrow. Data taken at 1.3 K, $V_{\text{bias}} = 5$ mV, $I \approx 10$ pA. This data set is ①

For quantum computing, one of the defining features of a system is the T_1 relaxation time [21]. One of the conditions for perform quantum operations without loss of signal is a large T_1. Hence, any mechanism through which T_1 can be increased deserves explo-

ration. We will focus on the lifetime of two spin states N_A and N_B, which will be denoted as T_H^S and T_L^S. As one of these two spin states will be associated with a higher energy, T_α^S for appropriate α can be considered relaxation time T_1. We will show that around a diabolic point these spin lifetimes can increase by several orders of magnitude. As has been previously shown, the case of a single Fe-atom on $Cu_2N/Cu(100)$, following 2.1 is exhibits various diabolic points [19], as a function of B_x and B_z. Here we show that this is also applicable for spin chains, with the additional advantage of longer lifetime overall and smaller required field strengths, making it much more accessible from an experimental point of view.

4.1. EXPERIMENTAL DESIGN

Figure 4.1a illustrates the set-up of the experiment. Shown is a chain of five atoms, Fe_5, on $Cu_2N/Cu(100)$ with the STM tip over one of them. The axes $\hat{x}$, $\hat{y}$, $\hat{z}$ are defined according to anisotropy set up by the Hamiltonian 2.1. In Chapter 2 we learned that when B_x is swept with a certain value of B_z a peak in the spin lifetime will appear. Here we will perform a similar experiment: B_x will be swept and the spin lifetime T^S will be determined on each atom of the chain. The Fe_5 data will be presented in terms of data sets (7 total). In our setup we apply external fields B_1 and B_2, which are decomposed into B_x, B_y and B_z as shown in the diagrams of Figure 4.1a. The decomposition depends on three angles: crystal angle Θ, sample angle Φ slant Ψ. The sample angle is 8° by design [22] and the slant is supposed to be 0°. The crystal angle is measured to be about $-1°$ for most data sets and can be adjusted during sample preparation. All these angles are approximate up to 0.5°. The external field $B_2 = 0$ T for most data sets. The main parameter varied is B_1, which has typical values between 2 T and 5 T. Through the decomposition this results in $B_x \approx B_1$, $B_y =\sim 500$ mT and $B_z =\sim 50$ mT. As the T^S, B_x-curve depends strongly on B_z, even for small values of B_z each figure sweeping B_1 will show B_x on the lower x-axis and the additional B_z in the upper x-axis.

Figure 4.1b shows how the data is acquired. We place a spin-polarized STM tip over one of the atoms and record the current I as a function of time t in constant-height mode at $V_{\text{bias}} = 5$ meV. From the time trace we identify two states (H and L, for high and low current, respectively). We identify the times τ_H and τ_L as the duration spent in either state, which is then turned into a histogram and subsequently fitted to an exponential function $ce^{-\tau/T_\alpha^S}$, yielding lifetimes T_H^S and T_H^S, respectively. The lifetime plotted in Figure 4.1c is $T^S = (\frac{1}{T_H^S} + \frac{1}{T_L^S})^{-1}$, which we call the spin lifetime. The ratio of the lifetimes $\frac{T_H^S}{T_L^S}$ will be used later as a proxy for the ratio of populations. Data is taken at constant-height mode after initializing after a 1 s integration at 10 pA. Temperature $T = 1.3$ K, which are typical values throughout the experiment.

Figure 4.1c shows how T^S increased by about 1.5 orders of magnitude from 2 ms at $B_x = 2$ T to 70 ms at $B_x = 4$ T for atom C. From the rate equations in Chapter 2 we can see that the spin lifetime can be extended if either the energy difference between the ground state and first excited state $\Delta E_{0,1}$ exceeds the available energy, or if the scattering amplitude $P_{0,1}$ decreases. The behaviour shown in Figure 4.1c is similar to Figure 2.11 and Figure 2.16 where the parametric proximity to a diabolic point reduces the scatter-

Table 4.1: Overview of data sets. Sets ① and ⑦ are taken on the same chain but with a different tip apex and are explored further in Figure 4.1 and Figure 4.3, respectively. Sets ②+③ and ⑤+⑥ are taken with the same tip apex on the same chain. The former two vary the applied V_{bias}, the latter two vary the external field B_2. Data set ④ has a different Θ compared to the other sets. Data set ⑦ is part of a larger data set taken at various current setpoints.

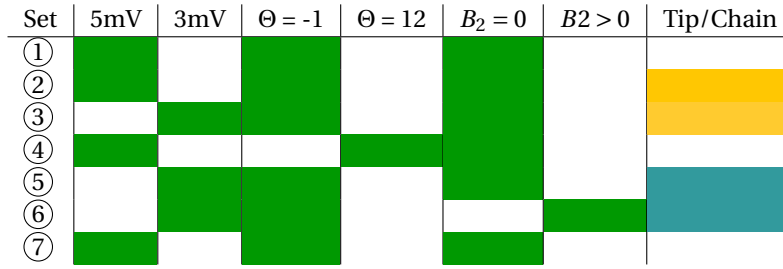

ing amplitude $P_{0,1}$ between the two lowest energy states. To prove that it is indeed the decrease in scattering amplitude rather than not providing enough energy for $\Delta E_{0,1}$ we note that the bias voltage $V_{\text{bias}} \geq 3$ meV where $\Delta E_{0,1} \ll 1$ meV. This last inequality follows from IETS measurements and simulations performed on chains in Chapter 2. Furthermore, if energy was the limiting factor, only one of T_H^S and T_L^S should increase, while in reality both increase. For example, the lifetimes in panel (b) show both being larger than 10 ms. We therefore posit that this data can be associated with a diabolic point.

The lifetimes curves behave different, depending on which atom is probed: atom C shows the largest lifetime increase, followed by atoms B/D and the peak is absent in atoms A/E. In Section 2.1.3 we learned that over-the-barrier excitations can limit lifetimes. Meanwhile from Figure 2.14 we know that outer atoms experience their main excitation at a lower energy. This is also corroborated in Section 3.3 and relates to the excitations towards states mainly composed of $\{\pm 1, \mp 2, \pm 2\}$ and $\{\pm 2, \mp 2, \pm 1\}$. For atoms A/E the over-the-barrier excitations cause state-switching at a higher rate than the quantum tunneling of magnetization would do. Atoms B/D are in an intermediate situation. This is only possible because the temperature is finite, giving a small portion of the energy distribution of the electrons enough energy to excite the chain from atoms B/D, but not C.

4.2. ROBUSTNESS

In order to prove the robustness of this effect, various chains are assembled and experimental parameters are varied. For Fe_5 this results in seven data sets, summarized in Table 4.1, with each data set being signified by an encircled number. Certain data sets are related in that they are taken on the exact same chain with or without the exact same tip apex. This is encoded by like colors in the last two columns on the table. All data referred to in this table is taken with $I = 10$ pA, although data set ⑦ is part of a larger data set where the current setpoint is varied; this is further explored in Figure 4.3. The lifetime curve on atom C for these seven data sets is shown in Figure 4.2b. Despite the

variations in parameters, all curves show similar qualitative behaviour.

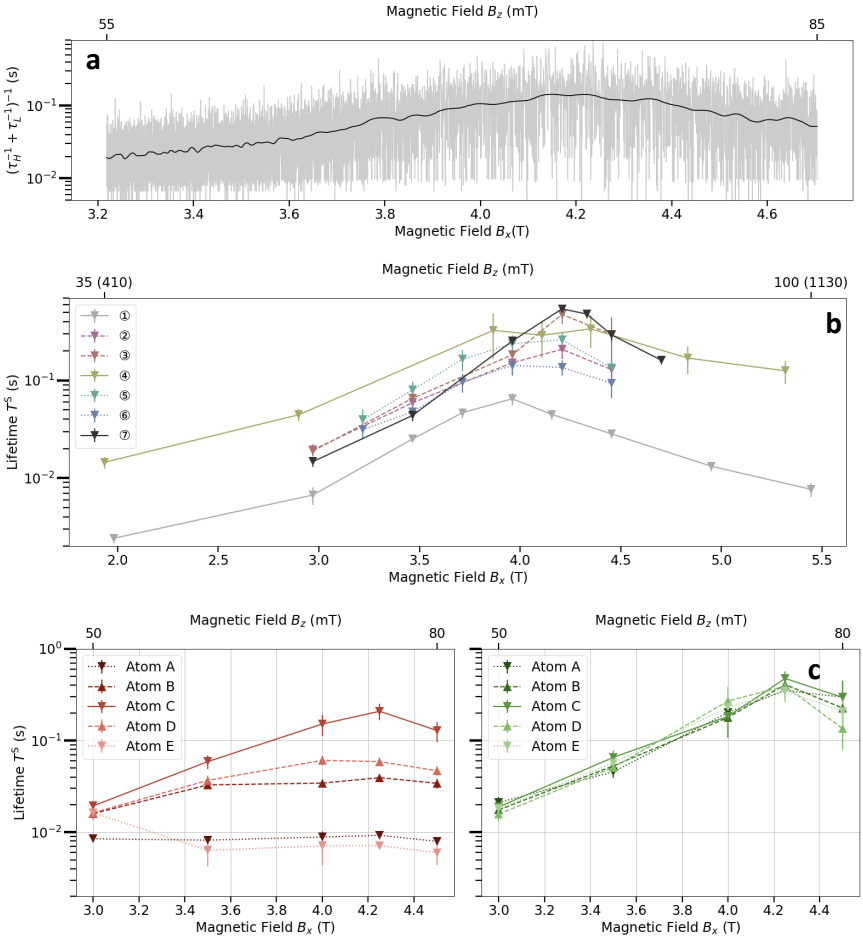

Figure 4.2: Robustness test of diabolic point measurement. **(a)** Constant-current duration $\tau_H + \tau_L$ measurement as the magnetic field is swept between $B_x \approx 3.25T$ and $B_X \approx 4.75$ T, with according B_z shown on top. Black line is Gaussian filtered from the gray line behind it. **(b)** Seven sets of data, taken on atom C of various Fe_5-chains with unique names. ① is the dataset shown in Figure 4.1c. ② has the same settings as ②, but taken on a different chain with a different tip. It is also shown in panel **c**.③ has the same settings as ②, but taken at 3 mV, also shown in panel **d**. ④ has the same settings as ①, but taken at $\theta_4 = 12°$. ⑤ has the same settings as ①, but with a different chain and tip and at 3 mV. ⑥ has the same settings as ⑤, but with an additional magnetic field B_2 that doubles the ϕ-induced B_y. ⑦ has the same settings as ①, on the same chain but with a different tip and further explored in Figure 4.3. The additional field B_z is shown on top, with the value for ④ in parentheses due to $\theta_{①} = 12°$. **(c)** Diabolic point measurements taken 5 mV (②) and **(d)** 3 mV (③). Solid lines with down-triangles indicate atom C. Dashed lines with up-triangles indicate atoms B/D. Dotted lined with down-triangles indicate atoms A/E. Lines are guide to the eye. Error bars are 2σ.

Data sets ②+③ compare the effect of lowering the V_{bias}. As described before, Figure 4.1c shows that atoms A/E do not show a peak in the lifetime for the given measurement parameters, due to over-the-barrier excitations, while atoms B/D show a peak with less intensity. Figure 4.2c shows that this behaviour is consistent for a second chain, where in red are lifetime curves for $V_{\text{bias}} = 5$ mV on all five atoms. Meanwhile in green, for $V_{\text{bias}} = 3$ mV, all five atoms show basically the same lifetime curve, indicating that at this voltage lifetimes are not limited by over-the-barrier excitations. In this particular case, even for atom C at 5 mV the lifetime of the chain is slightly limited by over-the-barrier excitations, as indicated by $\tau^{S}_{3\text{mV}}/\tau^{S}_{5\text{mV}} > 1$ at the peak.

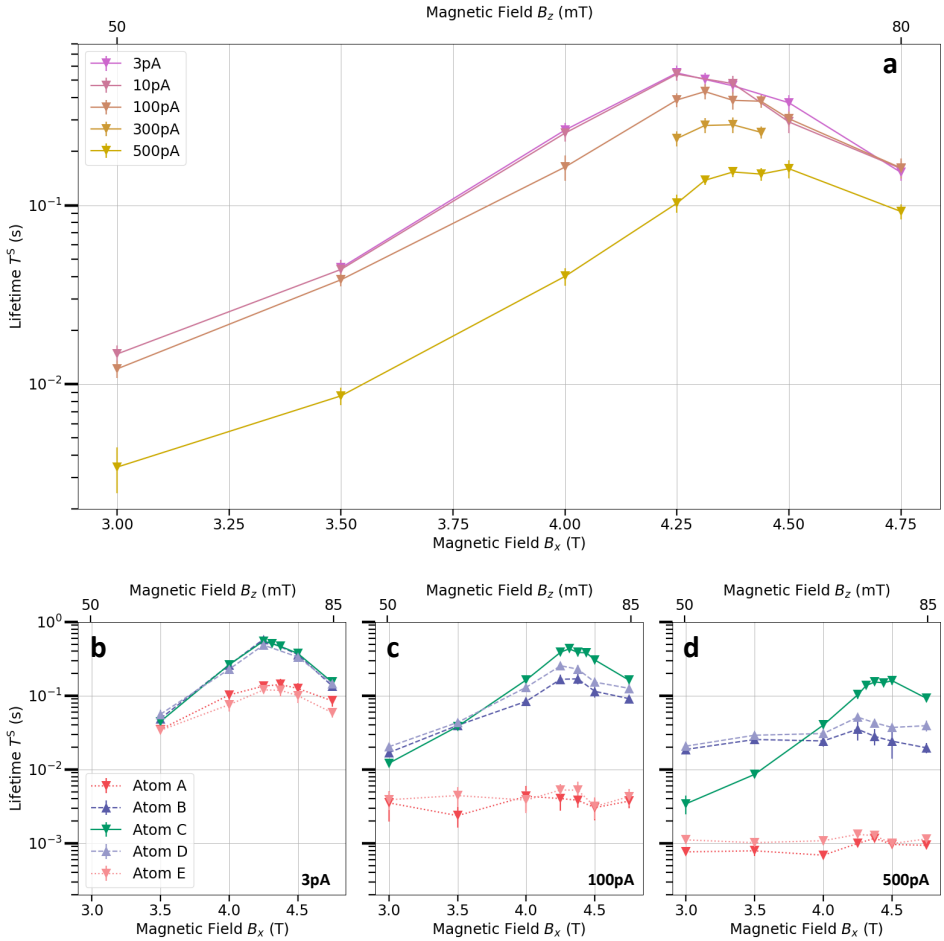

Figure 4.3: Current dependence of diabolic point measurement. **(a)** Lifetime measurements on atom C, for various values of current set point. **(b-d)** Lifetime measurments on atoms A-E for three different current set points: 3 pA, 100 pA and 500 pA, respectively. All data is taken at 5 mV, $T = 1.3$ K. Associated B_Z is shown on the top axes. Data on atom C of panels **b-d** appear also in panel **a**. Lines are guide to the eye. Error bars are 2σ.

The color shades dark to light indicate atom position A to E, respectively. Down arrows indicate atoms A/C/E, up arrows indicate B/D. Dotted lines indicate outer atoms (A/E), dashes lines indicate semi-outer atoms (B/D) and solid lines indicates inner atom (C). This color, arrow and line encoding is consistent throughout this chapter with the only exception in Figure 4.2b.

Data set ④, shown also in Figure 4.2b can be compared with Data set ① for the effect of varying the crystal angle Θ. With $\Theta_{④} = 12°$, as compared to $\Theta = 1°$ for all other data sets, the additional field B_z is much larger. In order to compare this data set with the others, the value in parentheses on the top x-axis of Figure 4.2b applies to this data set. From Chapter 2, in particular Figure 2.12, we would expect the peak width to scale with B_z, making the peak width about 10 times as large for this data set compared to others. However, estimations for the peak width $W_{④} \approx 1.5$ T compared to $W \approx 1$ T for other data sets do not support this scaling. This suggests that there may be additional causes for the broadening of the peak. Two of these were explored also in Chapter 2: inhomogenous g-factors and tip field.

Data sets ⑤+⑥ compare the effect of applying B_2, in order to increase B_y. The value of B_2 is scaled with B_1 such that the total value of B_y is doubled. Figure 4.2b shows that the application of this field lowers the lifetime at the peak only slightly. This is consistent with simulations (not shown).

In order to prove the consistency of the behaviour of these lifetime curves against a different experimental design, Figure 4.2a shows the time the duration of two consecutive switches $\tau_H + \tau_L$ on atom C while the magnetic field was being swept in gray. The black line is a rolling average. While this reduces the total measuring time from about 1 day to about 1 hour, the method is also prone to accidental tip crashes. It also requires the system to operate in constant-current mode, which requires a feedback loop whose response time limits the observable lifetimes. Nonetheless, even with this method we observe about one order of magnitude increase in the lifetime on atom C between ~ 3.25 T and ~ 4.25 T, which is consistent with Figure 4.2b.

Next we consider the effect of increasing the current set point. We observe several effects, which are shown in Figure 4.3. First, with increasing current the lifetime goes down. This is expected as tunneling electrons perform measurements and spin flips, leading to state switches, as explained in Chapter 2. For atoms A/E, in panels b-d this effect follows $\frac{1}{T^S} \sim I$. This makes sense as the over-the-barrier excitations are done by tunneling electrons alone. Meanwhile atom C also has its lifetime going down, although the effect seems quite reduced. This also makes sense because the lifetime is limited by quantum tunneling of magnetization, which is done by both tunnelling and bath electrons. Notice that over-the-barrier excitations are also possible on atom C, but the relevant excited energy eigenstates for this are spatially modulated to along the chain to have a higher intensity at the edges. The most peculiar effect happens on atoms B/D, where the lifetime away from the diabolic point seems to stay stable. We interpret this as a combination of lifetime reducing effects like the ones on atoms A/C/E and lifetime increasing effects as shown by Yan et al. [12] on even-numbered atoms in an odd chain.

This last effect is due to an exchange coupling with the tip and adatoms. Interestingly this effect does not seem to have a significant effect at the diabolic point itself, as there the lifetime is still reduced. Secondly, we find that as the tip gets closer, B_{diab} shifts to higher fields, suggesting the tip is counteracting the external magnetic field. This indicates that a local B_x on a single atom is able to shift B_{diab} of the whole structure. Finally, the peak width W did not significantly alter for higher currents.

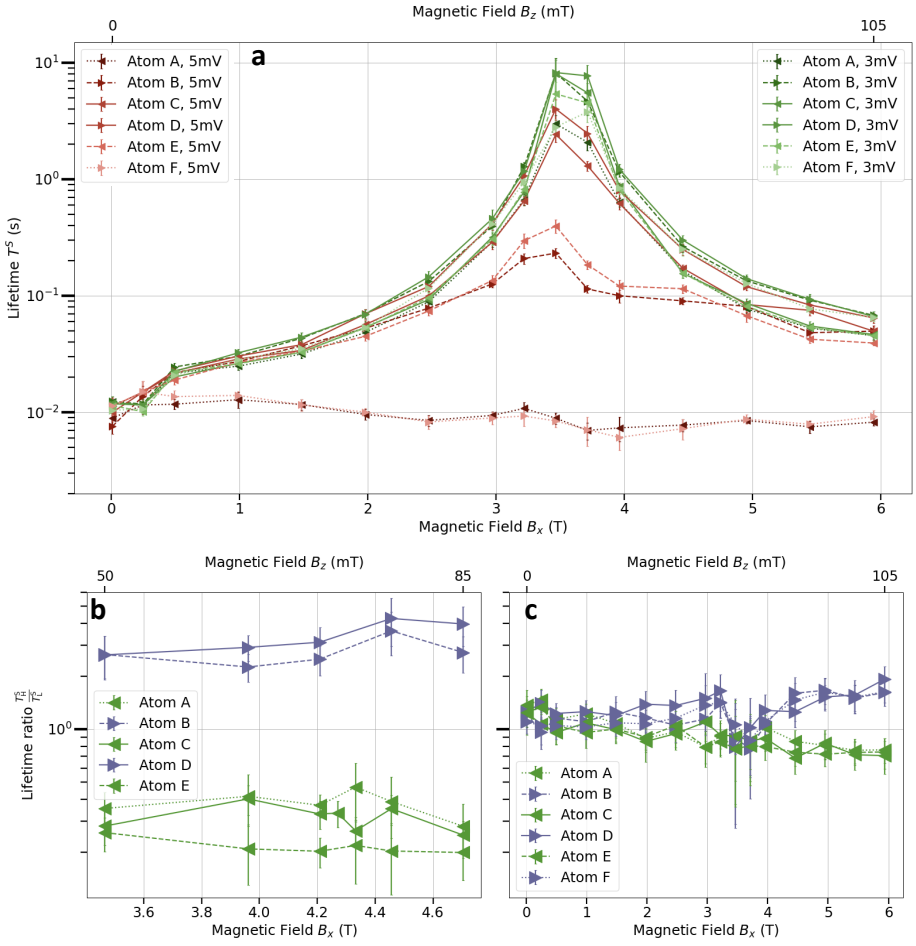

Figure 4.4: Diabolic point measurement on Fe_6 and lifetime ratio. **(a)** Lifetime measurements on all atoms of Fe_6. Red colored data is taken at V_{bias} = 5 mV. Green colored data at 3 mV. Current setpoint is 10 pA and T = 1.3 K. **(b)** Ratio of lifetimes T_1^H/T_1^L for data set corresponding to Figure 4.3b. **(c)** Ratio of lifetimes for dataset corresponding to panel **a**. Colors are green for atoms A/C/E and blue for atoms B/D/F, indicating the two states of N_B. Lines are guide to the eye. Error bars are 2σ.

4.3. ORIGIN OF PERTURBATION

For an odd chain, like Fe_5, in a magnetic field that contains a sizeable B_z, it is clear that there is no degeneracy, even at $B_x = B_{\text{diab}}$, as explained in Chapter 2, which allows for a diabolic lifetime peak to be measured. This lifting of the degeneracy we consider as a perturbation and the associated energy perturbation energy. For an even chain, like Fe_6 it is less obvious that there is perturbation energy. In fact, in an ideal situation there should be no perturbation energy and so no lifetime peak to be measured. Yet, Figure 4.4 clearly shows a peak in the lifetime of more than 2 orders of magnitude compared to both experimental values and literature values [23]. This is true for the data taken at $V_{\text{bias}} = 3$ mV for all atoms, and atoms C/D at 5 mV. As shown in Figure 2.17, it is still possible for an even chain to exhibit a peak in the lifetime if either the g-factors are inhomogenous along the chain or if the magnetic tip's field is sufficiently large. We will show using lifetime ratios $\frac{T_{\text{H}}^{\text{S}}}{T_{\text{L}}^{\text{S}}}$ that both apply to this Fe_6.

For this, let us first consider a more obvious example, shown in Figure 4.4b. Here the lifetime ratios of the five atoms of an Fe_5 (dataset equivalent with Figure 4.3b) are shown. The ratio in lifetime is a proxy for the population distribution. In the case of $V_{\text{bias}} = 0$ mV, this should follow Boltzmann statistics. Atoms A/C/E all have a lifetime ratio around 0.3, whereas atoms B/D have a lifetime ratio of about 3. If we apply Boltzmann statistics to this, it would show that the energy difference $\Delta E_{0,1}$ between the ground state ψ_0 and the first excited state ψ_1 is about $\ln(3) k_B T \approx 120$ μeV, where k_B is the Boltzmann constant and $T = 1.3$ K. This is order of magnitude consistent with the expected Zeeman energy $E_{\text{Zeeman}} = g\mu_B B(S_z^{\psi_1} - S_z^{\psi_0}) \approx 35$ μeV. Here $S_z^{\psi_i}$ is the total spin of the entire chain for state i, which is assumed to be ± 2. The difference can be accounted for by variations in the exact value of θ, ϕ and Ψ. Note that from Figure 4.3 the lifetime does not differ significantly between 3 pA and 10 pA, suggesting that the conductance with the substrate bath dominates, in which case Boltzmann statistics becomes valid. What is clear is that all five atom show a lifetime ratio which is consistent with a Néel configuration (e.g. N_B). This behaviour is consistent among all seven sets addressed in Figure 4.2.

On the other hand, for the Fe_6 data, Figure 4.4c shows this Néel-like configuration only for $B_x > 4$ T, although the behaviour can be said to start around 2 T with a break at $B_{\text{diab}} \approx 3.6$ T. Meanwhile for $B_x < 2$ T, the lifetime ratio for all atoms is measured to be approximately the same. With the spin polarized contrast yielding ~ 8pA for the low current and ~ 15pA for the high current, we conclude that the states are clearly skewed towards N_A and N_B. Yet, all atoms show similar lifetime ratio of about 1.1. The reason for this is that each atom that is being probed will experience a tip field B_{tip}. Depending on whether the tip is over atoms A/C/E or B/D/F, the ground state will be skewed towards either N_A or N_B. This results in all atoms showing similar lifetime ratios for $B_x < 2$ T. For larger values of B_x this does not hold anymore, because the perturbation due to inhomogenous g-factors scales with B, whereas the effect of B_{tip} does not. This means that this Fe_6 dataset has two regimes: for $B_x < 2$ T the tip's field is the main cause of perturbation, and for $B_x > 2$ T, the inhomgenous values of g are the main cause of perturbation. What's interesting is that for $B_x = B_{\text{diab}}$ the lifetime ratios are closer to 1, which is consistent with the minimum energy in an avoided crossing of the diabolic point. Finally, we

must state that it is also possible that the perturbation energy is caused by significantly inhomogenous values of D and/or E in the Hamiltonian 2.1, but we deem this unlikely due to the required deviation of those values and the fanning out of the lifetime ratios for $B_x > 4$ T.

To summarize, we have shown the existence of a peak in the lifetime of more than 2 orders of magnitude when sweeping hard-axis magnetic field B_x for spin chains, in particular Fe_N on Cu-sites on $Cu_2N/Cu(100)$. The effect is shown to be due to a reduction in switching rates through-the-barrier, which in Chapter 2 is explained to be due to a reduction in the scattering amplitude. This is established to be the result of crossing a diabolic point with a perturbation energy due to the parity of the structure, the tip field or inhomogenous g-factors. It is shown that this phenomenon is robust to various experimental parameters such as voltage V, current I, tip field B_{tip}, intermediate axis magnetic field B_y, crystal angle Θ and chain length parity.

There are multiple ways to expand upon this work, of which two will be presented. As was briefly addressed near the end of Chapter 2, the introduction of J in a chain of Fe_N splits the diabolic point in N. One can thus extend the length of the chain to reduce the required field for the second peak. It is expected that Fe_8 will have peaks around $B_x = 3$ T and $B_x = 8$ T, which is within the range of QNS's Bob system (which goes up to 9 T). This would experimentally prove the existence of multiple diabolic points.

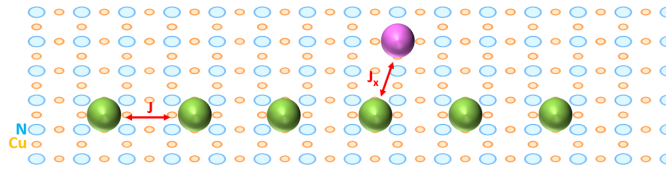

Figure 4.5: Lifetime Spectroscopy Concept. Experimental design in which an Fe_6 chain is built on $Cu_2N/Cu(100)$ (green) with a nearby Fe atom in pink. The pink atom has its easy axis perpendicular to the chain, and will induce an effective field on the chain through the coupling J_x.

Alternatively, since this experiment is based on sweeping B_x, one could design an experiment that probes the coupling strength J_x between two systems with their easy axes perpendicular. One such experiment is sketched in Figure 4.5. Here an Fe_6-chain is built on $Cu_2N/Cu(100)$, in green and a probed atom is depicted in pink. This can be an Fe atom on a Cu-site that is hopped, and thus has its easy axis, perpendicular to the chain. Following $J_x \mathbf{S}_i \cdot \mathbf{S}_j$ This should induce an effective B_x^{ind} from the pink atom onto the chain, which, as per Figure 4.3, should shift the measured B_{diab}. This shift will be up or down, depending on the spin-state of the investigated atom. As the investigated atom will have a lifetime significantly shorter than the integration time of the measurement, this would essentially lead to an ensemble measurement in which both are measured at the same time. This would then produce two peaks, where $\Delta B_X = 2B_x^{\text{ind}}$. From this the coupling strength between two atoms that have their easy axis perpendicular to one another could be measured.

BIBLIOGRAPHY

1. Hirjibehedin, C. F. *et al.* Large Magnetic Anisotropy of a Single Atomic Spin Embedded in a Surface Molecular Network. *Science* **317,** 1199–1203. https://doi.org/10.1126/science.1146110 (2007).
2. Paul, W. *et al.* Control of the millisecond spin lifetime of an electrically probed atom. *Nature Physics* **13,** 403–407. ISSN: 1745-2481. https://doi.org/10.1038/nphys3965 (Apr. 2017).
3. Donati, F. *et al.* Magnetic remanenence in single atoms. *Science* **352,** 318–321. ISSN: 6283. https://doi.org/10.1126/science.aad9898 (2016).
4. Vaxevani, K. *et al. Extending the spin excitation lifetime of a magnetic molecule on a proximitized superconductor* 2022. https://arxiv.org/abs/2203.05613.
5. Heinrich, B. W., Braun, L., Pascual, J. I. & Franke, K. J. Protection of excited spin states by a superconducting energy gap. *Nature Physics* **9,** 765–768. ISSN: 1745-2481. https://doi.org/10.1038/nphys2794 (Dec. 2013).
6. Yang, K. *et al.* Electrically controlled nuclear polarization of individual atoms. *Nature Nanotechnology* **13,** 1120–1125. ISSN: 1748-3395. https://doi.org/10.1038/s41565-018-0296-7 (Dec. 2018).
7. Balashov, T. *et al.* Magnetic Anisotropy and Magnetization Dynamics of Individual Atoms and Clusters of Fe and Co on Pt(111). *Phys. Rev. Lett.* **102,** 257203. https://doi.org/10.1103/PhysRevLett.102.257203 (25 June 2009).
8. Khajetoorians, A. A. *et al.* Spin Excitations of Individual Fe Atoms on Pt(111): Impact of the Site-Dependent Giant Substrate Polarization. *Phys. Rev. Lett.* **111,** 157204. https://doi.org/10.1103/PhysRevLett.111.157204 (15 Oct. 2013).
9. Liu, B. *et al.* An Iron-Porphyrin Complex with Large Easy-Axis Magnetic Anisotropy on Metal Substrate. *ACS Nano* **11,** 11402–11408. ISSN: 1936-0851. https://doi.org/10.1021/acsnano.7b06029 (Nov. 2017).
10. Rejali, R. *et al.* Complete reversal of the atomic unquenched orbital moment by a single electron. *npj Quantum Materials* **5,** 60. ISSN: 2397-4648. https://doi.org/10.1038/s41535-020-00262-w (Aug. 2020).
11. Hastings-Simon, S. R. *et al.* Zeeman-level lifetimes in $Er^{3+}:Y_2SiO_5$. *Phys. Rev. B* **78,** 085410. https://doi.org/10.1103/PhysRevB.78.085410 (8 Aug. 2008).
12. Yan, S., Choi, D.-J., Burgess, J. A. J., Rolf-Pissarczyk, S. & Loth, S. Control of quantum magnets by atomic exchange bias. *Nature Nanotechnology* **10,** 40. https://www.doi.org/10.1038/nnano.2014.281 (Dec. 2014).
13. Victor, B. M. & Mark, W. Diabolical points in the spectra of triangles. *Proc. R. Soc. Lond.* **A,** 15–43. https://doi.org/10.1098/rspa.1984.0022 (1984).

14. Yang, J. *et al.* Diabolical points in coupled active cavities with quantum emitters. *Light: Science & Applications* **9,** 6. ISSN: 2047-7538. https://doi.org/10.1038/s41377-020-0244-9 (Jan. 2020).

15. Kirillov, O. N., Mailybaev, A. A. & Seyranian, A. P. Unfolding of eigenvalue surfaces near a diabolic point due to a complex perturbation. *Journal of Physics A: Mathematical and General* **38,** 5531–5546. https://doi.org/10.1088/0305-4470/38/24/007 (June 2005).

16. Wernsdorfer, W. & Sessoli, R. Quantum Phase Interference and Parity Effects in Magnetic Molecular Clusters. *Science* **284,** 133–135. https://doi.org/10.1126/science.284.5411.133 (1999).

17. Wernsdorfer, W., Chakov, N. E. & Christou, G. Quantum Phase Interference and Spin-Parity in Mn_{12} Single-Molecule Magnets. *Phys. Rev. Lett.* **95,** 037203. https://doi.org/10.1103/PhysRevLett.95.037203 (3 July 2005).

18. Burzurı, E. *et al.* Quantum Interference Oscillations of the Superparamagnetic Blocking in an Fe_8 Molecular Nanomagnet. *Phys. Rev. Lett.* **111,** 057201. https://doi.org/10.1103/PhysRevLett.111.057201 (5 July 2013).

19. Bruno, P. Berry Phase, Topology, and Degeneracies in Quantum Nanomagnets. *Physical Review Letters* **96.** https://doi.org/10.1103/physrevlett.96.117208 (Mar. 2006).

20. Garg, A. Berry phases near degeneracies: Beyond the simplest case. *American Journal of Physics* **78,** 661–670. https://doi.org/10.1119/1.3377135 (2010).

21. Kloeffel, C. & Loss, D. Prospects for Spin-Based Quantum Computing in Quantum Dots. *Annual Review of Condensed Matter Physics* **4,** 51–81. https://doi.org/10.1146/annurev-conmatphys-030212-184248 (2013).

22. Hwang, J. *et al.* Development of a scanning tunneling microscope for variable temperature electron spin resonance. *Review of Scientific Instruments* **93,** 093703. https://doi.org/10.1063/5.0096081 (2022).

23. Loth, S., Baumann, S., Lutz, C. P., Eigler, D. M. & Heinrich, A. J. Bistability in Atomic-Scale Antiferromagnets. *Science* **335,** 196–199. https://doi.org/10.1126/science.1214131 (2012).

5

REMOTE DETECTION

Atomic spin structures assembled by means of STM provide valuable insight into the understanding of atomic-scale magnetism. Among the major challenges are the detection and subsequent read-out of ultrafast spin dynamics due to a dichotomy in travel speed of these dynamics and the probe tip. Here, we present a device composed of individual Fe atoms that allows for remote detection of spin dynamics. We have characterized the device and used it to detect the presence of spin waves originating from an excitation induced by the STM tip several nanometres away; this may be extended to much longer distances. The device contains a memory element that can be consulted seconds after detection, similar in functionality to e.g. a single photon detector. We performed statistical analysis of the responsiveness to remote spin excitations and corroborated the results using basic calculations of the free evolution of coupled quantum spins.

5.1. INTRODUCTION

Spin waves, quantum-mechanically described as *magnons*, are collective magnetic excitations that, due to their long-distance coherence [2], are considered promising candidates for future spintronic devices [3–6]. In light of the intrinsic quantum nature of these waves, their exact behaviour is difficult to predict. Scanning tunelling microscopy (STM)-based atom manipulation allows for the assembly of artificial spin structures [7, 8]: a technique that has enabled studies of collective magnetism ranging from the emergence of magnetic bistability [9–11] to spin waves [12], phase transitions [13, 14] and topologically protected edge states [15–17]. More recently, the implementation of electron spin resonance (ESR) [18] has led to coherent manipulation of combined atomic spin states [19]. However, by nature of the STM design, in each of these studies the effect of local tip-induced stimuli can only be probed there where they are generated.

Parts of this chapter have been published in Communications Physics **3**, 94 (2020) [1].

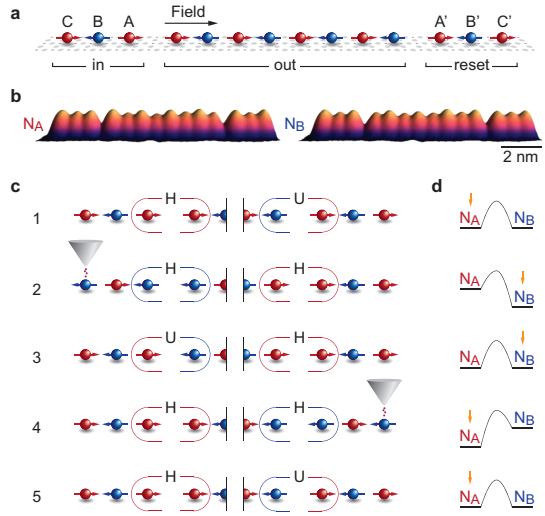

Figure 5.1: Operating principle of the spin wave detector. **(a)** Schematic overview of a 3-8-3 structure, consisting of an input lead (length $n_{in} = 3$), an output lead ($n_{out} = 8$) and a reset lead ($n_{reset} = 3$). Atoms in the input and reset leads are labeled alphabetically, counting outward from the output lead. **(b)** Side-view spin-polarized tunelling topographies (1 mV/10 pA at 1.5 K, 0.5 T) of a 3-8-3 in the two allowed states of the output lead: Néel states N_A and N_B. **(c)** Simplified operation cycle outlined in five steps; see text for more information. Favourable coupling configurations between the output and input/reset are labeled "H" (happy); unfavourable configurations are labeled "U" (unhappy). **(d)** Simplified energy diagrams showing N_A and N_B in the five situations described in (c). The arrow indicates the state of the output lead.

For atomic structures that have a static spin state, remote detection schemes exist that make use of a nearby atomic probe [20–22]. In order to remotely probe the dynamic response occurring faster than the tip travel time, one would need to implement a memory unit that stores this response until the tip has had time to arrive. Such memory-based remote detection schemes have been implemented for dynamic processes not based on spin [23, 24]. In this work, we present a device that provides memory-based remote detection of spin dynamics in atomic spin structures. By comparing experimental results to calculations we show that the triggering of the detector correlates with the probability of a magnetic excitation induced elsewhere reaching the detector due to free quantum evolution.

5.2. RESULTS

5.2.1. DESIGN OF SPIN WAVE DETECTOR

The general design of the spin wave detector, shown in Fig. 5.1a, is based on Fe atoms on top of Cu_2N. All structures are built in a line along a nitrogen row of the Cu_2N molecular network. This direction coincides with the easy axis of the Fe atom spins, which we treat as effective $S = 2$ [25]. During the experiment we apply a magnetic field $B = 0.5 - 1.0$ T along this direction in order to maintain spin-polarized tunelling contrast [9]. Struc-

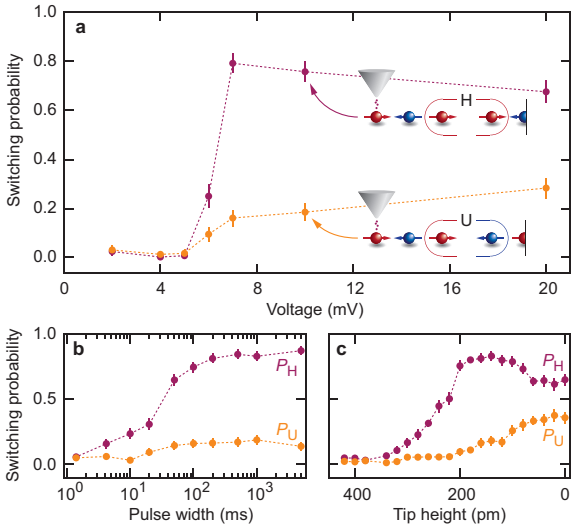

Figure 5.2: Switching probabilities as a function of pulse voltage, pulse width and tip height. **(a)** Measured values of switching probabilities P_H and P_U as a function of pulse voltage. Data taken with 550 ms pulses at 20 pA (1.5 K, 0.5 T). **(b)** Measured values of P_H and P_U as a function of pulse width. Data taken at 10 mV, 1.1 pA (1.5 K, 1 T), corresponding to a tip height of 160 pm. Tip heights are defined in comparison to regulating at 1 mV, 3 pA on the Cu_2N island. **(c)** Measured values of P_H and P_U as a function of tip height. Data taken at 10 mV, pulse width 200 ms (1.5 K, 1 T). All data based on $N \geq 180$ attempts with the error bars showing 1.5σ for a binomial distribution with μ at the recorded rate. Dashed lines are guides to the eye.

tures consist of three parts: an input lead, an output lead and a reset lead. The length of these parts are given as n_{in}, n_{out} and n_{reset} respectively. For reasons discussed below, the output lead is required to have an even length, whereas the input and reset leads are required to be odd. Throughout this paper we will use $n_{out} = 8$, $n_{reset} = 3$ and $3 \leq n_{in} \leq 9$. To describe the structures we will use the shorthand "n_{in}-n_{out}-n_{reset}"; for example, the structure shown in Fig. **??** will be referred to as "3-8-3".

Neighbouring atoms that are part of the same lead are separated by two unit cells of the Cu_2N lattice, which is known to result in an antiferromagnetic coupling with coupling constant $J = 0.7$ meV [26]. Adjacent atoms from different leads are separated by three unit cells. We have determined through inelastic electron tunnelling spectroscopy and spin-polarized STM that this separation results in a ferromagnetic coupling -0.05 meV$< J' < 0$ meV. This is shown in Section 3.3. We will use $J' = -0.05$ meV throughout the rest of this chapter. See Chapter 2 for a detailed description of the Hamiltonian.

As demonstrated by means of spin-polarized STM in Fig. 5.1b, the output lead will at any time be in either of two Néel states N_A and N_B. For $n_{out} = 8$, both these states have a lifetime upward of several seconds [9]. We define N_A to be the state where the output atom closest to the input lead is aligned with the field. Since n_{in} and n_{reset} are odd, atoms A and A' (see Fig. 5.1a) will also prefer to align with the field. As a result, when neither the input nor the reset lead is excited, the N_A-state will have a favoured ('happy') coupling to the input lead and an unfavoured ('unhappy') coupling to the reset lead. In this situation N_A and N_B are degenerate.

An operation cycle consists of the five steps outlined in Fig. 5.1c. (1) First, the output lead is set to N_A. If this is not the case, the output can be initialized by starting the cycle at step 3. (2) A spin excitation is induced in the input lead, affecting the spin state of atom A. The resulting energy splitting between N_A and N_B causes the system to fall to its ground state N_B. (3) The output lead, consulted by the STM tip, retains its state N_B after the input lead relaxes to its original state. Further actuation on the input lead does not change the output state. (4) A reset is performed by means of a similar excitation on the reset lead, after which (5) the system returns to its initial state N_A. This design provides a ratchet behaviour, where the output lead should switch only if the coupling configuration on the input side is 'happy', and never if it is 'unhappy'. In the following experiments we always start with the tip on the input lead. We then define P_H as the measured probability for the output lead to switch from N_A to N_B, and P_U the probability to switch from N_B to N_A.

In the figure, the input and reset leads are shown to fully invert. However, we emphasize that switching of the output lead would also occur if atom A in step 2 is only partially inverted due to a spin excitation. In fact, as we will discuss below, switches of the output lead can occur already if the magnetization of atom A is changed from $S_z = -2$ to $S_z = -1$, i.e., due to a single short-lived $|\Delta S_z| = 1$ excitation.

5.2.2. TRIGGERING BY MEANS OF VOLTAGE PULSES

We have tested the functionality of the device by switching the input lead in two different ways: by means of local spin excitations in the input lead and by means of tip field-induced static inversion of the input lead as a whole. In the first method we perform voltage pulses on input atoms, and we characterize the response of the output lead as a function of pulse parameters. Fig. 5.2a shows the switching efficiency after applying voltage pulses of varying height on atom C. Pulse width and tunelling current are kept constant at 550 ms and 20 pA to ensure the same number of electrons for all pulses. We note that this current is too low for the input trimer to spend a significant amount of time in the inverted state. Statistics throughout this paper are based on $N \gtrsim 100$ attempts. During readout of the output lead, the tunnel junction is set to 10 pA at 2 mV, i.e. below the excitation energy.

For small pulse amplitudes, measured switching probabilities are close to zero. However, from approximately 7 mV, which corresponds to the energy of a spin excitation on atom C from its $S_z = -2$ to its $S_z = -1$ state, increased values are found. Switching probability P_H, for switches originating from the state where the input lead is in the 'happy' configuration, reaches 80%. Note that switching probability P_U from the 'unhappy' configuration remains much lower, consistent with the expected behaviour of the device. For even larger pulse voltages P_U increases while at the same time P_H decreases. This can be explained in terms of secondary switches during a single pulse back towards the 'happy' state. Hence $P_H + P_U \leq 1$.

Figures 5.2b and c show P_H and P_U as a function of pulse width and tip height, respectively. For the settings used in Fig. 5.2b, we find an approximate switching time $\tau = 25$ ms. As I depends exponentially on tip-sample distance, both graphs show an equivalent range of number of electrons per pulse, $I\Delta t \approx [10^4, 10^8]$. While both graphs behave similar for small $I\Delta t$, they diverge at higher values: when increasing pulse width, P_H and P_U are found to plateau, while increasing I eventually increases P_U (thus reduc-

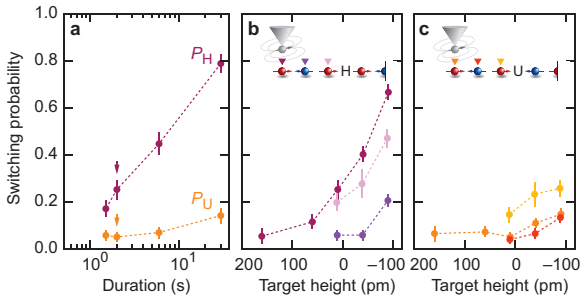

Figure 5.3: Switching the input by tip exchange field. **(a)** Switching probabilities P_H and P_U as a function of duration at a target tip height of 10 pm, using a bias voltage of 1 mV. Arrows indicate data points that also appear in panels b and c. **(b)** P_H for atoms A, B and C, for a duration of 2 seconds. Note how atom B is less sensitive to the tip field than atoms A and C. **(c)** Same as (b) but for P_U. Data in all three subpanels is taken at 1.5 K, 1 T. The error bars show 1.5σ for a binomial distribution with μ at the recorded rate. Dashed lines are guides to the eye.

5

ing P_H). This suggests a path for switching from the 'unhappy' configuration which is based on a multi-excitation process, presumably due to magnon excitations tunelling into the output lead (see Section 5.5).

5.2.3. TRIGGERING BY MEANS OF TIP EXCHANGE FIELD

In order to exclude the possibility of tunelling magnons, the second method to switch the output lead involves reversing the input lead via controlled exchange coupling with the tip [27]. In this experiment the voltage is kept below the excitation threshold and the tip is held over an input atom at a certain target height for a certain duration. Figure 5.3a shows the switching probabilities P_H and P_U as a function of duration for a fixed target height of 10 pm (as compared to regulating at 1 mV, 3 pA on Cu_2N). For this target height we find $\tau \approx 5$ s.

A more detailed investigation is shown in figure 5.3b (c), which shows P_H (P_U) on the different atoms of the input lead as a function of target height. For sufficiently large tip separation, no switching is observed. Bringing the tip closer to the input lead induces switches of the output lead, suggesting that the tip field causes the predominant state of the input lead to switch from $(S_z^C, S_z^B, S_z^A) = (-2, +2, -2)$ to $(+2, -2, +2)$. For target heights down to -100 pm, P_H on atoms A and C increases, while P_U does not increase significantly. Likewise, P_H on atom B does not increase significantly beyond P_U.

We emphasize that the essence of the switching mechanism is different in this second method compared to the first: here the input lead spends a significant amount of time in the fully inverted state, whereas in the first case, $|\Delta S_z| = 1$ excitations on one side of the barrier are the dominant cause for the reduction of the time averaged S_z^A.

5.2.4. EXTENDED INPUT LEAD AND COMPARISON WITH CALCULATIONS

Having characterized the sensitivity of the detector to spin excitations on the input lead as described in Fig. 5.2, we now consider the effect of introducing these excitations at different distances. In Fig. 5.4a,b we compare switching measurements for various tip

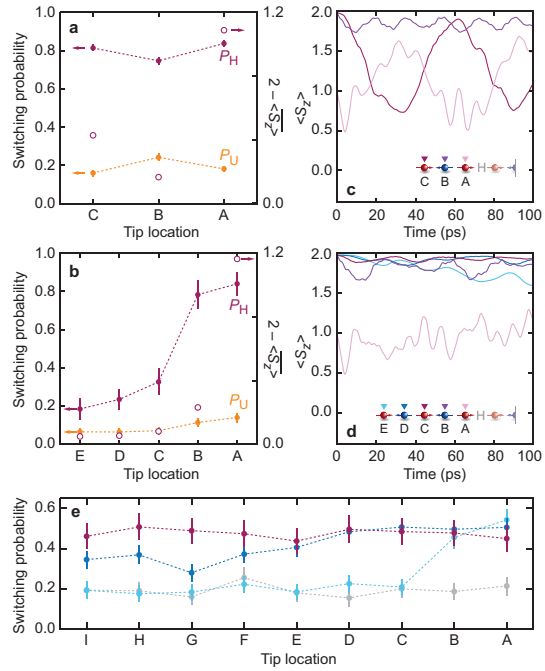

Figure 5.4: Switching probabilities as a function of tip location and input length compared to calculations. **(a)** Closed circles: switching probabilities P_H and P_U as a function of tip location for $n_{in} = 3$ (10 mV, 2 pA, 550ms). Open circles: values averaged over the first 20 ps from panel (c). Note the different axes used for open and closed circles. **(b)** Same as (a) but for $n_{in} = 5$ (10 mV, 1.6 pA, 100ms) **(c)** Time-dependent Schrödinger equation calculations performed on an Fe trimer. The curves show the time evolution of the expectation value of S_z at atom A following a single excitation on each of the input atoms. **(d)** Same as (c) but for an Fe pentamer. **(e)** P_H as a function of tip location for $n_{in} = 9$. Different curves correspond to different tip heights: 180 pm (420 fA), 80 pm (4.3 pA) and 30 pm (15.2 pA) for respectively light blue, dark blue and magenta. All voltage pulses last 300 ms at 10 mV. The grey curve is taken at 180 pm, 1 mV, for reference. Data in subpanels a, b, e are taken at 1.5 K, 1 T. The error bars show 1.5σ for a binomial distribution with μ at the recorded rate. Dashed lines are guides to the eye.

locations on the input lead for $n_{in} = 3$ and 5. While the measurements on the 5-8-3 indicate a monotonous decrease of the switching probability as a function of distance to the output lead, both for switches from the 'happy' and 'unhappy' states, measurements on the 3-8-3 show a marked reduction in P_H, and corresponding increase in P_U, when the tip is located on atom B.

In order to gain insight into this behaviour, we performed time-dependent Schrödinger equation calculations simulating the dynamics of the input lead upon an excitation (Fig. 5.4c,d). In these calculations we model only the input lead. The coupling to the output lead is modeled by an effective magnetic field on atom A (see Section 5.5). First, we initialize the system by finding the ground state of the Hamiltonian. Next, we perform a single spin excitation on one of the input atoms (i.e., we apply the $\hat{S}_+$ or $\hat{S}_-$ operator depending on the position in the antiferromagnetic input lead), after which we apply the time-dependent Schrödinger equation to the resulting state. Plotted are the values $S_z^A(\alpha)$ after

an excitation on atom α. Dissipation effects are not considered in these calculations.

Figures 5.4c,d show the results of calculations for the first 100 ps on a trimer and pentamer, respectively. As expected, S_z^A values never reach much lower than +1, so a full inversion of the input lead does not occur in these calculations. We estimate the lifetime of an excitation to be ~ 10 ps (see Section 5.5, not to be confused with the ~ 1 μs lifetime of the inverted state, see Section 3.4). Therefore we took the averaged values of $S_z^A(\alpha)$ over the first 20 ps and plotted these as open circled in figures 5.4a,b. As in the experimental data, this results in a deviation from $S_z^A = 2$ that alternates for the trimer, while it decreases monotonously for the pentamer. These results suggest that the spin wave detector is able to register unitary spin dynamics.

Finally, in Figure 5.4e, we show switching experiments on a 9-8-3 device. Here we find that it is possible to switch the output lead from as far away as 6.8 nm (19 Cu_2N lattice sites). We find that as the current increases, the distance where $P_H \approx 50\%$, the maximum value for this structure, also increases: from 7 lattice sites for $z = 180$ pm to at least 19 lattice sites for $z = 30$ pm. For this structure the results are compared with a background measurement ($V = 1$ mV, $z = 180$ pm), which yields a minimum switching rate of ~ 20%. We attribute this increased base switching probability to łonger lifetime of the input lead (in the order of 1 second), therefore spending extended periods of time in the inverted state, even in the absence of excitations.

5.3. DISCUSSION

In summary, we have developed an atomic device that can be used to detect dynamic and nonlocal spin phenomena such as magnons. We have tested the device for its sensitivity to spin excitations, as well as a complete inversion of the input lead. We have shown that the device is sensitive to spin excitations originating up to 9 atoms away. In subsequent experiments the input lead may be replaced by more exotic spin architectures. This method thereby provides a tool in studying dynamic spin processes on the atomic scale.

5.4. METHODS

We used a UNISOKU USM-1300s ^{3}He STM system, operating at 1.5 K and $B = 0.5 - 1$ T in the plane of the sample, along the axis of the structures. The $Cu_2N/Cu_3Au(100)$ sample was prepared as described by Gobeil et al. [28]. The tip is prepared as in Loth et al. [9]. Fe atoms were picked up from the Cu_2N by using bias pulses of approx. 1 V at (regulation 100 pA, 20 mV, then move −300 pm) and dropped at −600 μV with the tip gradually nearing the surface until a change in current is observed. The Fe was subsequently maneuvered into place with a pulse of approximately 1 V at (100 pA, 20 mV). Calculations were performed using QuTip [29] [30], a library for Python.

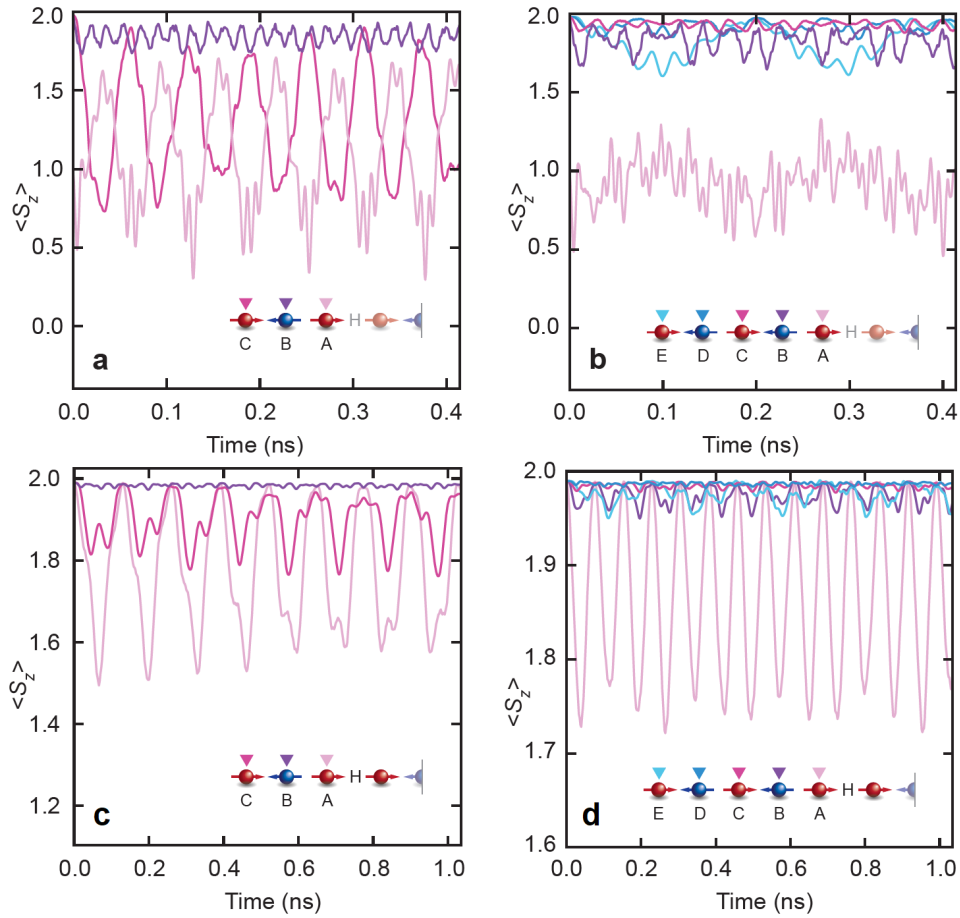

Figure 5.5: Time-dependent Schrödinger equation solution. **(a)** Time-dependent S_Z-value of atom A of a trimer biased to an octomer after an excitation on atoms A, B, C (colored light pink, deep pink and purple, respectively). **(b)** Same as a but for a pentamer. **(c)** Same as **a** but the calculations include the first atom of the octomer. **(d)** same as **c** but for a pentamer.

5.5. SIMULATIONS

The Hamiltonian used for the simulations are described in Chapter 2. Figure 5.5 shows the spin value of atom A after an excitation on various atoms of a trimer (a) and pentamer (b). This is the last atom prior to detector. It also shows the spin value of the first atom of the adjacent octamer for an input trimer (c) and pentamer (d). Figures (a,b) are extended figures compared to Figure 5.4(c,d). The experimental findings show that with a trimer as input, excitations on atoms A and C are able to cause flips on the octomer very effectively, while excitations originating from atom B are not as effective in causing flips of the octomer. This is also shown in Figure 5.5(a,c). The different colors indicate excitations performed on atoms A, B and C, see diagram. It is clear that excitations in atoms A and C cause significant spin variation on atom A (panel a). It also clear that

these cause significant spin variations in the first atom of the octomer (panel c). Both panels also show excitations in atom B not affecting atom A or the first atom of the octomer so much. Although the excitations are short-lived compared to the range of this figure, even taking the average variation of the first 20ps is enough to support the claim of the paper. What's more, in a pentamer experimental findings show a decaying effect on atom A / first atom of the octomer as the excitation happens further from atom A. Panels b and d clearly show an excitation on atom A has very strong effects. The second largest effect during the first 20ps comes from excitations originating in atom B, followed by C and then D and E. What's interesting is that even though the coupling from E to atom A is quite significant given enough time (about 100ps, from panel b), experimentally this is not supported. The conclusion drawn from this is that the excitations really do have a lifetime of about 10ps. A subsequent conclusion drawn from panels c and d is that the excitations enter the octomer. This explains how at very large excitation current, the output trimer seems to behave differently, as shown in Figure 5.2.

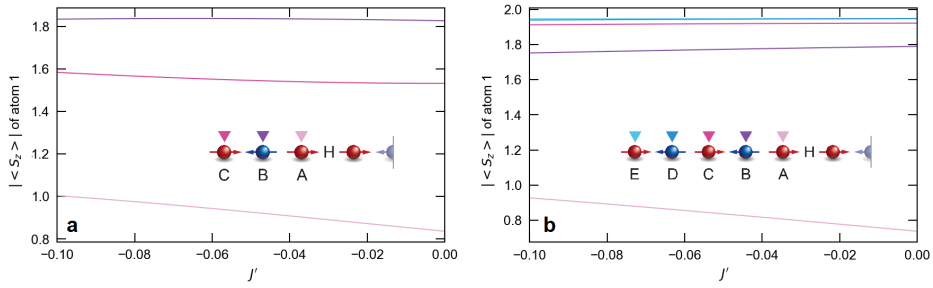

Figure 5.6: Sweeping J'. Both panels show $S_z^A(\alpha)$ as a function of J', with α indicated by color. Panel (a) applies to an input trimer. Panel (b) applies to an input pentamer.

Throughout this chapter we assume $J' = -0.05$, the coupling strength between atom A and the octomer. This value was based on fitting IETS data of dimers, as shown in section 3.3. These fits have a large uncertainty however, so any value $-0.1 < J' < 0$ would pass the fit. One could wonder whether the claims of this chapter are different depending on the value of J'. Figure 5.6 shows that the claims remain the same. Shown is the average value of the first atom of the octomer after an excitation on the various input atoms (A-C for trimer, panel a and A-E for pentamer, panel b). Since none of the colored lines cross, the behaviour stays the same and the claim is justified. What's more, this graph shows that an excitation on atom B in a pentamer should have similar effects as an excitation on atom B in a trimer, which is supported by experimental evidence.

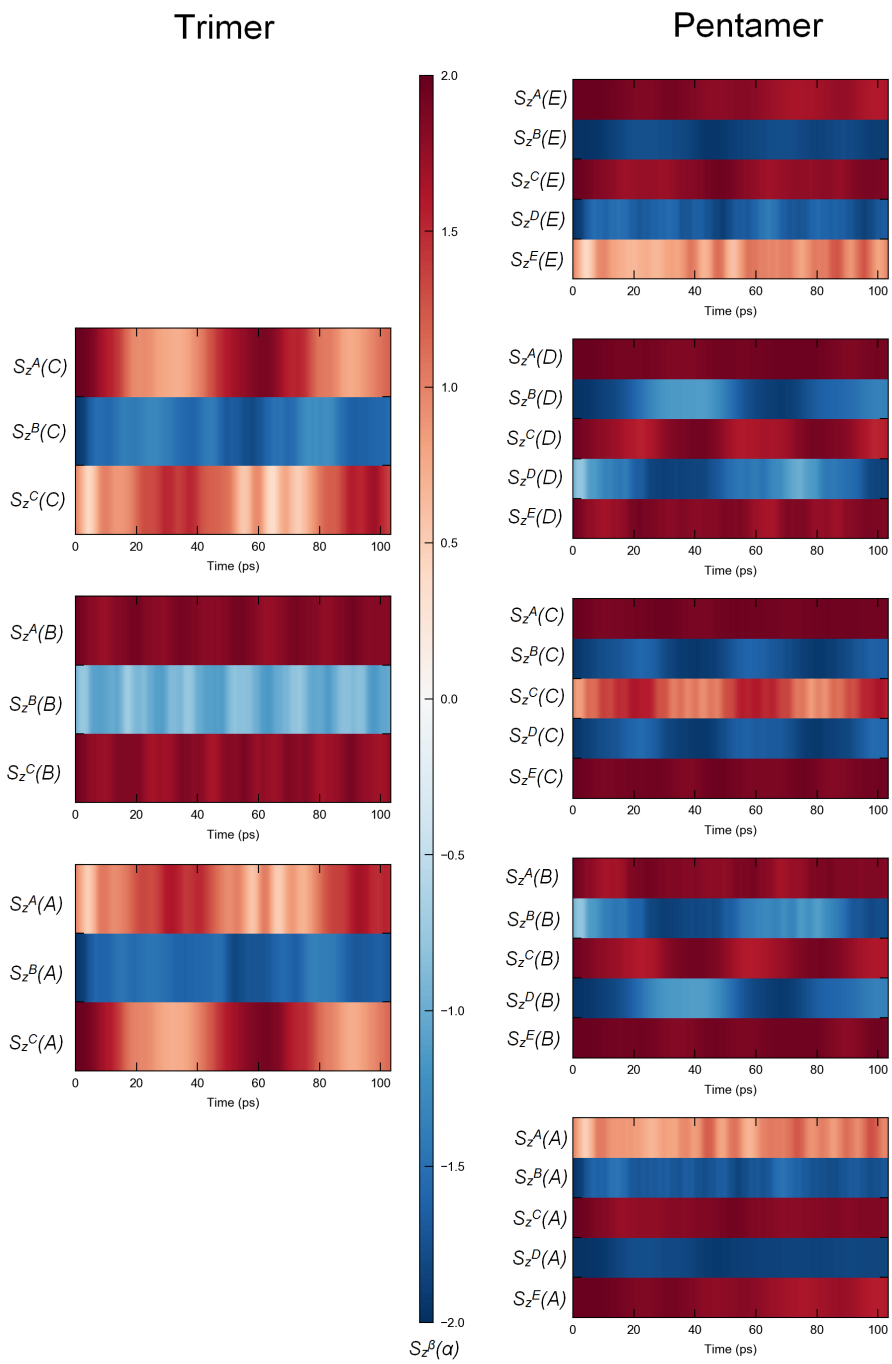

Figure 5.7: Full results of Time-Dependent Schrödinger Equation (TDSE) calculations. All 8 panels show $S_z^\beta(\alpha)$:the Sz value on atom β after an excitation is performed on atom α, shown for the first 100 ps. Panels on the left correspond to an input trimer. Panels on the right correspond to an input pentamer. Top row of each panel corresponds to atom A

Figure 5.7 explores what happens with the S_z-value on the various atoms β after an excitation is performed on atom α. Shown is the value $S_Z^{\beta}(\alpha)$. No octomer atom is included in the simulation here, though a lead is applied on atom A. The top row of each plot corresponds with Figure 5.5a,b. The first and third plot on the left show clearly a magnon bouncing backing and forth along the chain. We can estimate the magnon speed at 50 m/s. We can also see how an excitation in atom B is kind of "stuck" in atom B. This makes sense as the way to initialize this state was by means of an S_+ operator. The resulting increase in spin cannot really be distributed to other atoms, as they are already near their maximum spin value. Only once atom B is in a pentamer can it perform some kind of coupling, with its next nearest neighbour atom D. Its exchange of spin is significantly smaller than atoms A/C on the trimer. Interestingly, on the pentamer it is near impossible for excitations starting in atoms A, C or E to reach any of the others (A, C or E). This is explained by atoms B and D, now able to exchange some of their spin variation, being much better at blocking magnons.

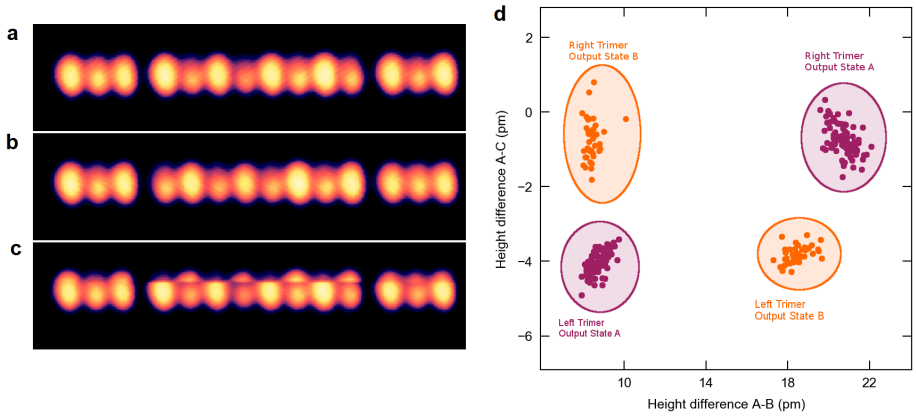

Figure 5.8: Remote sensing of the output state. **(a,b)** Topographic images of a 3-8-3 in its two states, N_A and N_B. The left trimer in the *a* and the right trimer in *b* show a weaker Néel-like contrast. Images taken at 1 mV/10 pA, 0.5 T, 1.5 K. **(c)** Similar topographic image showing a switch in the octamer, which also affects the trimers. **(d)** Scatterplot with the difference in height between atoms A and B (C) for the x-axis (y-axis). Data points are grouped based on the Néel state of the octamer and on which trimer this difference was measured (left or right). A total of 122 images were analysed.

5.6. REMOTE READ-OUT

As was shown before [20], it is possible to remotely read out the state of the bistable spin structure by means of a weakly coupled trimer. As shown in Supplementary Figure 5.8 this is possible also in our structure. In fact, it may even be visible in topographies.

When the output lead is in N_A, as shown in panel (a), the spin-polarized contrast of the reset lead is enhanced compared to that of the input lead. When the output lead is in N_B (panel (b)), this difference is inverted. Figure (c) shows the distribution of height

differences between atoms A,B ($\Delta z_{A,B}$) and A,C ($\Delta z_{A,C}$). Both trimers experience a stark difference in $\Delta z_{A,B}$ depending on the state of the output lead, one that is even observable by eye.

A total of 122 images were taken over the course of 160 minutes. During this time, the octamer has switched four times. Panel (c) shows such a switch on the output lead, which has a slight effect on the trimers.

BIBLIOGRAPHY

1. Elbertse, R., Coffey, D., Gobeil, J. & Otte, A. Remote detection and recording of atomic-scale spin dynamics. *Communications Physics* **3.** https://doi.org/10.1038/s42005-020-0361-z (May 2020).
2. Lenk, B., Ulrichs, H., Garbs, F. & Münzenberg, M. The building blocks of magnonics. *Physics Reports* **507,** 107–136. https://doi.org/10.1016/j.physrep.2011.06.003 (2011).
3. Chumak, A. V., Vasyuchka, V. I. & Serga A. A.and Hillebrands, B. Magnon spintronics. *Nature Physics* **11,** 453. https://doi.org/10.1038/nphys3347 (2015).
4. Khajetoorians, A. A., Wiebe, J., Chilian, B. & Wiesendanger, R. Realizing All-Spin–Based Logic Operations Atom by Atom. *Science* **332,** 1062–1064. https://doi.org/10.1126/science.1201725 (2011).
5. Han, J., Zhang, P., Hou, J. T., Siddiqui, S. A. & Liu, L. Mutual control of coherent spin waves and magnetic domain walls in a magnonic device. *Science* **366,** 1121–1125. https://doi.org/10.1126/science.aau2610 (2019).
6. Wang, Y. *et al.* Magnetization switching by magnon-mediated spin torque through an antiferromagnetic insulator. *Science* **366,** 1125–1128. https://doi.org/10.1126/science.aav8076 (2019).
7. Hirjibehedin, C. F., Lutz, C. P. & Heinrich, A. J. Spin Coupling in Engineered Atomic Structures. *Science* **312,** 1021–1024. https://doi.org/10.1126/science.1125398 (2006).
8. Choi, D.-J. *et al.* Colloquium: Atomic spin chains on surfaces. *Rev. Mod. Phys.* **91,** 041001. https://doi.org/10.1103/RevModPhys.91.041001 (4 2019).
9. Loth, S., Baumann, S., Lutz, C. P., Eigler, D. M. & Heinrich, A. J. Bistability in Atomic-Scale Antiferromagnets. *Science* **335,** 196–199. https://doi.org/10.1126/science.1214131 (2012).
10. Loth, S., Etzkorn, M., Lutz, C. P., Eigler, D. M. & Heinrich, A. J. Measurement of Fast Electron Spin Relaxation Times with Atomic Resolution. *Science* **329,** 1628–1630. https://doi.org/10.1126/science.1191688 (2010).
11. Khajetoorians, A. A. *et al.* Current-Driven Spin Dynamics of Artificially Constructed Quantum Magnets. *Science* **339,** 55–59. https://doi.org/10.1126/science.1228519 (2013).
12. Spinelli, A., Bryant, B., Delgado, F., Fernández-Rossier, J. & Otte, A. F. Imaging of spin waves in atomically designed nanomagnets. *Nature Materials* **13,** 782. https://doi.org/10.1038/nmat4018 (July 2014).

13. Khajetoorians, A. A. *et al.* Atom-by-atom engineering and magnetometry of tailored nanomagnets. *Nature Physics* **8,** 497–503. https://doi.org/10.1038/nphys2299 (2012).

14. Toskovic, R. *et al.* Atomic spin-chain realization of a model for quantum criticality. *Nature Physics* **12,** 656–660. https://doi.org/10.1038/nphys3722 (2016).

15. Nadj-Perge, S. *et al.* Observation of Majorana fermions in ferromagnetic atomic chains on a superconductor. *Science* **346,** 602–607. https://doi.org/10.1126/science.1259327 (2014).

16. Kim, H. *et al.* Toward tailoring Majorana bound states in artificially constructed magnetic atom chains on elemental superconductors. *Science Advances* **4.** https://doi.org/10.1126/sciadv.aar5251 (2018).

17. Ruby, M. *et al.* End States and Subgap Structure in Proximity-Coupled Chains of Magnetic Adatoms. *Phys. Rev. Lett.* **115,** 197204. https://doi.org/10.1103/PhysRevLett.115.197204 (19 2015).

18. Baumann, S. *et al.* Electron paramagnetic resonance of individual atoms on a surface. *Science* **350,** 417–420. https://doi.org/10.1126/science.aac8703 (2015).

19. Yang, K. *et al.* Coherent spin manipulation of individual atoms on a surface. *Science* **366,** 509–512. https://doi.org/10.1126/science.aay6779 (2019).

20. Yan, S. *et al.* Nonlocally sensing the magnetic states of nanoscale antiferromagnets with an atomic spin sensor. *Science Advances* **3.** https://doi.org/10.1126/sciadv.1603137 (2017).

21. Natterer, F. D. *et al.* Reading and writing single-atom magnets. *Nature* **543,** 226–228. ISSN: 1476-4687. https://doi.org/10.1038/nature21371 (Mar. 2017).

22. Hermenau, J. *et al.* Stabilizing spin systems via symmetrically tailored RKKY interactions. *Nature Communications* **10,** 2565. https://doi.org/10.1038/s41467-019-10516-2 (2019).

23. Kügel, J. *et al.* Remote Single-Molecule Switching: Identification and Nanoengineering of Hot Electron-Induced Tautomerization. *Nano Letters* **17,** 5106–5112. https://doi.org/10.1021/acs.nanolett.7b02419 (2017).

24. Heinrich, A. J., Lutz, C. P., Gupta, J. A. & Eigler, D. M. Molecule Cascades. *Science* **298,** 1381–1387. https://doi.org/10.1126/science.1076768 (2002).

25. Hirjibehedin, C. F. *et al.* Large Magnetic Anisotropy of a Single Atomic Spin Embedded in a Surface Molecular Network. *Science* **317,** 1199–1203. https://doi.org/10.1126/science.1146110 (2007).

26. Bryant, B., Spinelli, A., Wagenaar, J. J. T., Gerrits, M. & Otte, A. F. Local Control of Single Atom Magnetocrystalline Anisotropy. *Phys. Rev. Lett.* **111,** 127203. https://doi.org/10.1103/PhysRevLett.111.127203 (12 2013).

27. Yan, S., Choi, D.-J., Burgess, J. A. J., Rolf-Pissarczyk, S. & Loth, S. Control of quantum magnets by atomic exchange bias. *Nature Nanotechnology* **10,** 40. https://www.doi.org/10.1038/nnano.2014.281 (Dec. 2014).

28. Gobeil, J., Coffey, D., Wang, S.-J. & Otte, A. F. Large insulating nitride islands on Cu3Au as a template for atomic spin structures. *Surface Science* **679,** 202–206. https://doi.org/10.1016/j.susc.2018.09.001 (2019).

29. Johansson, J., Nation, P. & Nori, F. QuTiP: An open-source Python framework for the dynamics of open quantum systems. *Computer Physics Communications* **183,** 1760–1772. https://doi.org/10.1016/j.cpc.2012.02.021 (2012).

30. Johansson, J., Nation, P. & Nori, F. QuTiP 2: A Python framework for the dynamics of open quantum systems. *Computer Physics Communications* **184,** 1234–1240. https://doi.org/10.1016/j.cpc.2012.11.019 (2013).

6

IMPLEMENTATION OF ESR-STM THROUGH AN ANTENNA

6.1. INTRODUCTION

This chapter consists of two parts. In the first part we will consider the installation of an RF antenna in the SPECS' JT system for ESR-purposes. In the second part we will go over ESR results, performed in the context of [1]. Note that the results shown in section 3.5 are performed in the same context and show both the largest ESR-STM peak published (3 pA, Figure 3.7a) and the one taken at the lowest tunneling current (800 fA, Figure 3.7b).

6.2. ANTENNA INSTALLATION

As explained in Section 3.5, ESR is based on applying radio frequency (RF) oscillating voltages to the tip-sample junction. The leading theory is that the oscillating voltages result in an oscillating electric field which moves the adatom through the gradient of the tip's magnetic field [2]. This is further exemplified through the successful control of a TiH system through the gradient of a neighbouring Fe atom [3].

In order for V_{RF} to reach the tip-sample junction two methods have been implemented. In the original implementation, the signal was applied directly to the tip [4], which has been repeated in several other instances [5–8]. Alternatively, one can send the signal to an antenna placed close to the tip-sample junction [1, 9], with some having designs for extra high frequencies up to 100 GHz [10]. In this chapter we explore an installation of the second type.

6.2.1. DESIGN

There are certain requirements for the cabling and connectors. This includes UHV proof, not responsive to magnetic fields, operational at very low temperatures, sufficient signal transfer up to 40 GHz and there must be a way to limit the transmission of mechanical noise. Figure 6.1 shows how the cabling from the RF generator to the antenna is made

up of four pieces. First, the cable from the RF source to the cryostat, which are both equipped with SMK connectors is done with a semi-rigid rigid cable (BRAND) of 1.8 m. Then inside the cryostat there are two semi-rigid cables (ULT-04 by Keycom) of length 0.9 m and 1.1 m, that are thermally anchored five times, including at 300 K, 77 K and 4 K. They are connected with SMK and SMP connectors. This specific coax cable was chosen for its high transmission even at low temperatures. Finally, in order to not transmit vibrations to the STM head, a flexible cable of 18 cm is chosen: Cooner Wire CW2040-3650F. To further reduce the vibration transmission the plastic coating was carefully stripped. This cable connects the previously mentioned semi-rigid cables via SMP connectors (Pasternack PE44961 and PE44785) to the antenna through SMPM connectors (Johnson 125-0692-111 /Johnson 125-0593-001). The antenna is also a ULT-04 semi-rigid of 3 cm and is stripped at the end. The stripped part is 6.5 mm long, bent after 1 mm, leaving 5.5 mm parallel to the tip. The antenna is 6 mm removed from the tip and about 0.5 ~ 1.0 mm removed from the sample.

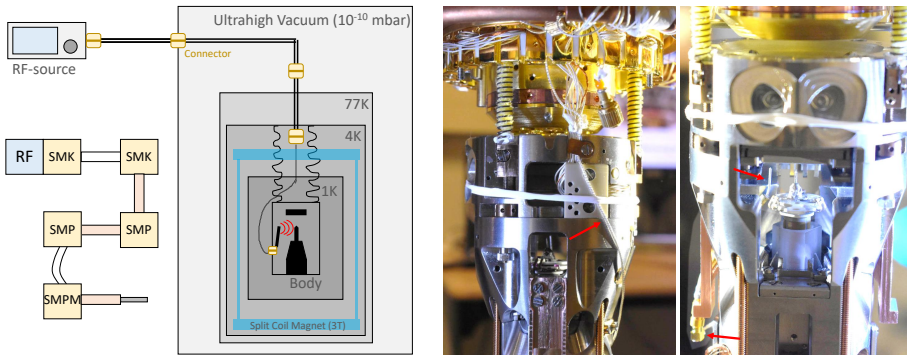

Figure 6.1: Cabling Path The RF signal is supplied to an antenna through a series of cables. On the left is a simplified diagram where orange cables are Keycom's ULT-04, the white cable is Coax Co., LTD.'s SC-219/50-SC and the bent cable is a stripped Cooner Wire CW2040-3650F. Left photo: stripped CW2040-3650F held close to the body by teflon tape. Right photo: antenna. Bottom arrow shows angled SMPM connection.

While SMP connectors are easier to solder than SMPM connectors, and both provide sufficient transmission along the range of $0-40$ GHz, the former are too bulky to be placed on the head. Not only would they increase the weight of the head, but also their size would not be permitted by the tight fit of the 1K-shield. The antenna is held in place by a copper piece, which is copied and placed on the opposite side of the head as well for balancing purposes. Since the sample stage is able to move laterally, it is possible to install so-called double decker samples for four-probe measurements by moving the stage sideways, inserting the sample, and moving the sample back.

6.2.2. TRANSFER FUNCTION

We will now consider the transfer function of the cabling from the RF generator to the tip-sample junction. This will be measured in two ways. First, by using a virtual network analyzer (VNA). This allows us to measure each individual part, but is limited in that it does not operate *in situ*. Secondly we can measure the transfer function through

broadening of IETS steps, as described in section 3.5, which is an *in situ* measurement but is limited in that it can only be a full transfer function and does not readily provide phase information. However, we will show through Fourrier analysis that we can still get information about various components of the transfer function. We will also show the importance of full detente connections, as opposed to smooth bore. First let us go over several tests to determine the right cabling. We are particularly interested in the regime of $20-40$ GHz as the minimum temperature $T = 1.3$ K results in population ratios close to unity for states split with less energy than the equivalent of 20 GHz while 40 GHz is the maximum frequency supplied by the many RF supplies. The transfer functions will be presented in terms of dB_V, i.e. one order of magnitude in voltage per ten dB, as compared to the more commonly used dB_P which is one order of magnitude in power per ten dB. This is standard practice in ESR-STM and results in a factor two decrease in value.

FLEXIBLE CABLE

For the flexible cable we compared three options, as shown in Figure 6.2a: Pasternack's PE-P047, Amphenol's FleXtra series .065" with SMA connectors and CoonerWire CW2040-x650F series. For the latter initial tests were performed with the larger CW2040-2650F since the soldering is easier, reducing the transmission losses there. This leads to all three cables having similar diameter. Amphenol and CoonerWire had similar transmission, especially in the $20-40$ GHZ regime, summarized with the dot around 0 GHz. With Amphenol being significantly stiffer than CoonerWire, that option was discarted. Figure 6.2b shows that the transmission increases more for CoonerWire than for Pasternack when submerged in liquid nitrogen at 77 K. Shown is also the semi-rigid ULT-04 from KeyCom as a reference.

The stiffness of the cables are assessed by hand, and it was found that CW2040-2650F was slightly less stiff than PE-P047. Removing the plastic jacket did not reduce the stiffness significantly for PE-P047, while it did reduce the stiffness significantly for CW2040-2650F. This even more true for CW2040-3650F, which was already less stiff due to its smaller diameter, which lead to it being chosen for the final design. The photo in Figure 6.2a shows a series of cables including in the middle the stripped CW2040-3650F that was installed. The resulting transfer function is lower than that of CW2040-2650 not only because the diameter is smaller and the jacket is removed, but also because it is soldered to an SMP and SMPM connector which are not designed for such small wires. The soldering is assumed to be non-perfect and is assumed to never reach perfection. The other two cables are KeyCom's ULT-04 and Pasternack's FleXtra 0.14", which both provide excellent transmission and can therefore mostly be disregarded. While the loss is larger, we determined the difference to be small enough to install it, given its much lower stiffness.

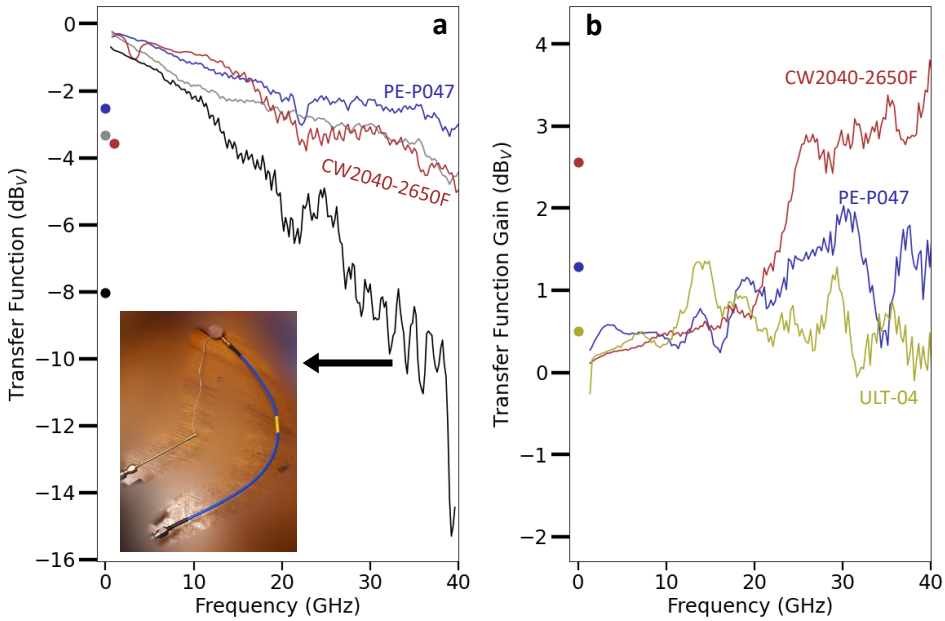

Figure 6.2: Flex Cable tests (a) Transfer function in dBVolt for Pasternack's PE-P047 (blue), Amphenol's FleXtra .065" (grey), CoonerWire's CW2040-2650F (red) and the set-up shown in the photo, which is a comination of KeyCom's ULT-04, a stripped CoonerWire's CW2040-3650F and Amphenol .014", with SMP and SMPM connectors on either side, simulating the final design (black). **(b)** The difference in transfer function for Pasternack's PE-P047, CoonerWire's CW2040-2650F and KeyCom's ULT-04 between 300 K and 77 K. The circles at 0 GHz is the average value between 20 – 40 GHz. Data is smoothed to see trends.

6

ANTENNA

To determine the right installation of the antenna, several tests have been performed, summarized in Figure 6.4. For this both the tip and antenna are modeled the same: a stripped coax cable. The signal entering the receiving side of the VNA is not exactly the same as the induced voltage at the tip-sample junction, but it will serve as an appropriate proxy for this. We will find that standing waves on the tip and sample are important determinants for the transmission:

$$f_\alpha(n) = \frac{2n+\delta_\alpha}{2}\frac{0.150}{\sqrt{\epsilon_r}l}\,[\text{GHz}] \tag{6.1}$$

Here $\alpha = \{\uparrow,\downarrow\}$ are related to peaks and troughs, respectively, in the transmission. With the delta-funcion $\delta_\alpha = \{\uparrow = 1, \downarrow = 0\}$, this leads to oscillatory behaviour for a frequency sweep. The value 0.150 is based on $c = 3\cdot 10^8$, considering l the wavelength in meters. The value $\sqrt{\epsilon_r}$ is the relative permittivity, which is 1 for air and about 2.3 for teflon (i.e. inside coax cables). Hence for a stripped coax cable of 5 mm, a trough in the transmission is expected at 30 GHz while peaks are expected at 15 GHz and 45 GHz.

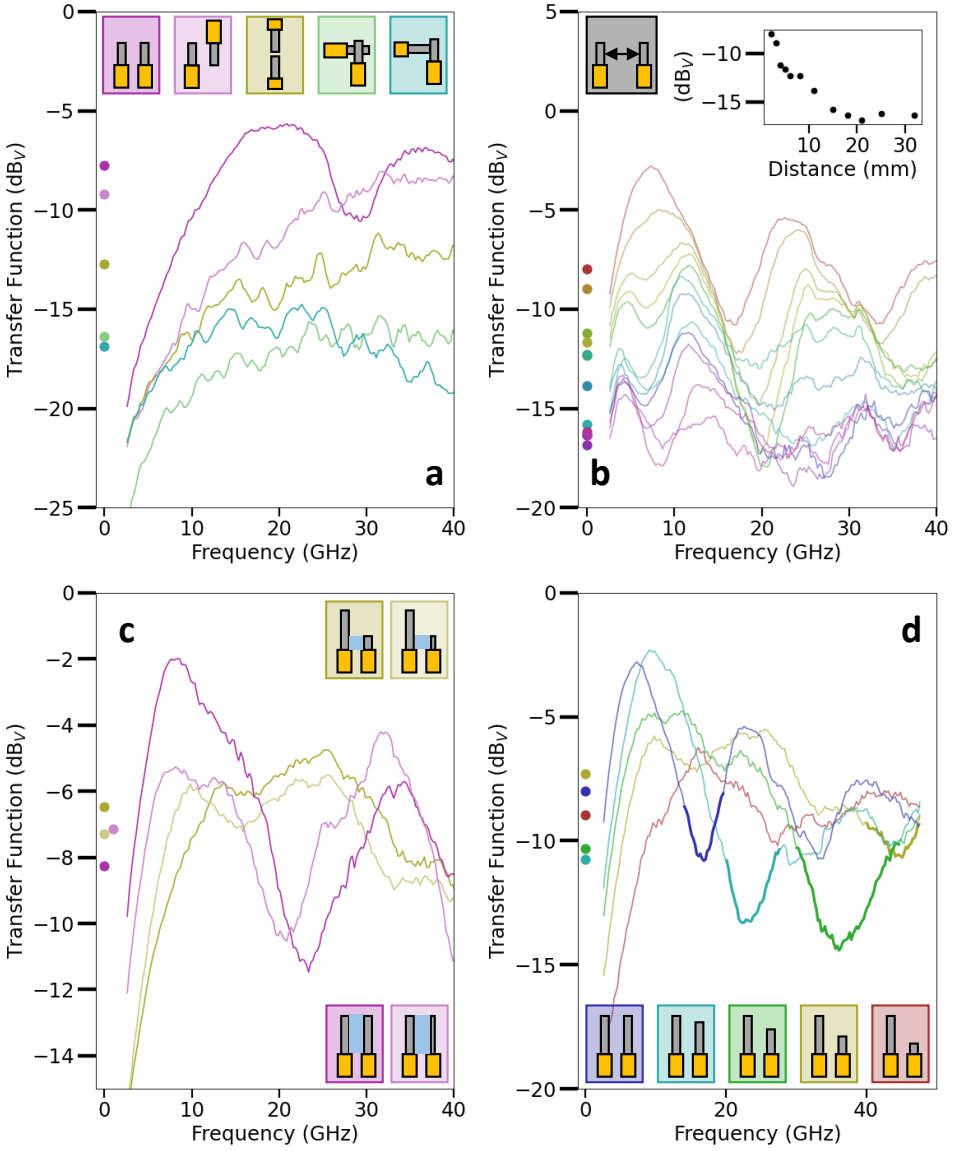

Figure 6.3: Antenna tests (a) Comparison of orientations, with the orientations show on the diagrams above. **(b)** Comparison of different lateral distances with a gradient color scheme going from 2 mm (red) to 32 mm (purple). Inset shows average transmission between 20 – 40 GHz as a function of distance. **(c)** Comparison of different rod radii. In pink: 10.7 mm ULT-04 / 7.7 mm ULT-04 (dark) and10.7 mm ULT-04 / 6.8 mm PE-P047 (light). In yellow: 10.7 mm ULT-04 / 2.8 mm ULT-04 (dark) and 10.7 mm ULT-04 / 3 mm PE-P047 (light). The blue shaded areas in the diagram indicates the overlap height. **(d)** Comparison of rod length where one is kept constant at 10.7 mm, and one varies between 10.3 mm (blue), 6.30 mm (cyan), 4.25 mm (green), 2.80 mm (yellow) and 1.75 mm (red). The yellow data in panel **d** corresponds to the dark yellow data on panel **c**. Rods in all panels are ULT-04 unless stated otherwise. All data is smoothed to show trends. Dots around 0 GHz indicate average transmission between 20 – 40 GHz.

Figure 6.4a uses two stripped ULT-04s and compares the relative orientation of tip and antenna and shows that parallel orientation is preferred, especially side-to-side. Further tests will take this orientation and this orientation will also be implemented. Figure 6.4b shows that as the distance between the tip and antenna increases, the transmission goes down. The antenna will therefore be placed as close as possible, which turned out to be 6 mm. Figure 6.4c compares the thickness of the tip/antenna in two instances (red and blue). Both instances show a slightly higher transmission when one of the two rods is thinner. However, the difference is considered too small to offset the trade-off in sturdiness. Further tests will use the thicker ULT-04 and this will also be implemented. Figure 6.4d compares different tip/antenna lengths. This heavily affects the standing wave pattern in that longer rods will produce more peaks and troughs within the relevant frequency range, consistent with Equation 6.1. Bolded are the troughs related to a tip/antenna of 10.3 mm (blue), 6.30 mm (cyan), 4.25 mm (green), 2.80 mm (yellow) and 1.75 mm (red). The other rod is kept constant at 10 mm. Notice that although the red curve overall has a lower transmission than the blue curve, it is much more homogeneous. Installed is an antenna of 5.5 mm length parallel to the tip. Although this would result in a trough at around 28 GHz, it would also result a peak at 14 GHz. Alternatively, if one uses a smaller tip, one should obtain a more homogeneous transfer function. As such, the idea is that by replacing the tip the user has the option between two modes: high power for certain frequencies or homogeneous transfer function.

This last point, about the difference between long and short tip, can also be seen in Figure 6.4c, where the yellow data is more homogeneous and the pink data is more oscillatory. This is the result of a smaller overlap height. In Figure 6.4b the standing waves are affected by lateral distance in a non-trivial manner, where a peak at 8 GHz turns into a trough for larger distances, and the trough at 18 GHz and 32 GHz increase in frequency also for larger distances. The former is considered the result of changing from the near field to the far field regime. The latter we account to deviating longitudinal distance. *Ex-situ* experiment show that the same long/short tip effect shown in panels c and d can also be reproduced by changing the longitudinal distance instead of the rod lengths, thereby also affecting the overlap height, as defined in panel c. However, as we will see in the next section, *in-situ* measurements with a tip length of 10 mm do not fully corroborate the oscillatory behaviour.

FOURRIER ANALYSIS

In this section we will compare the transfer function as measured through a VNA and measured *in-situ*. Figure 6.4a shows how for the latter an RF signal is send to the tip-sample junction and an IETS measurement is performed with and without this RF signal which smoothes the signal. By alternating between these on/off cycles (blue/orange, respectively), a lock-in amplifier operating at the same frequency can determine the difference in current at the IETS step, which is a measure for V_{RF}. The power sent from the RF generator P_{gen} reaches the tip-sample junction, where it results in a voltage V_{RF} with some losses, to be measured as a lock-in signal (LI). The losses, and therefore the lock-in signal will be different depending on the chosen frequency, and so through an iterative feedback loop a transfer function can be determined.

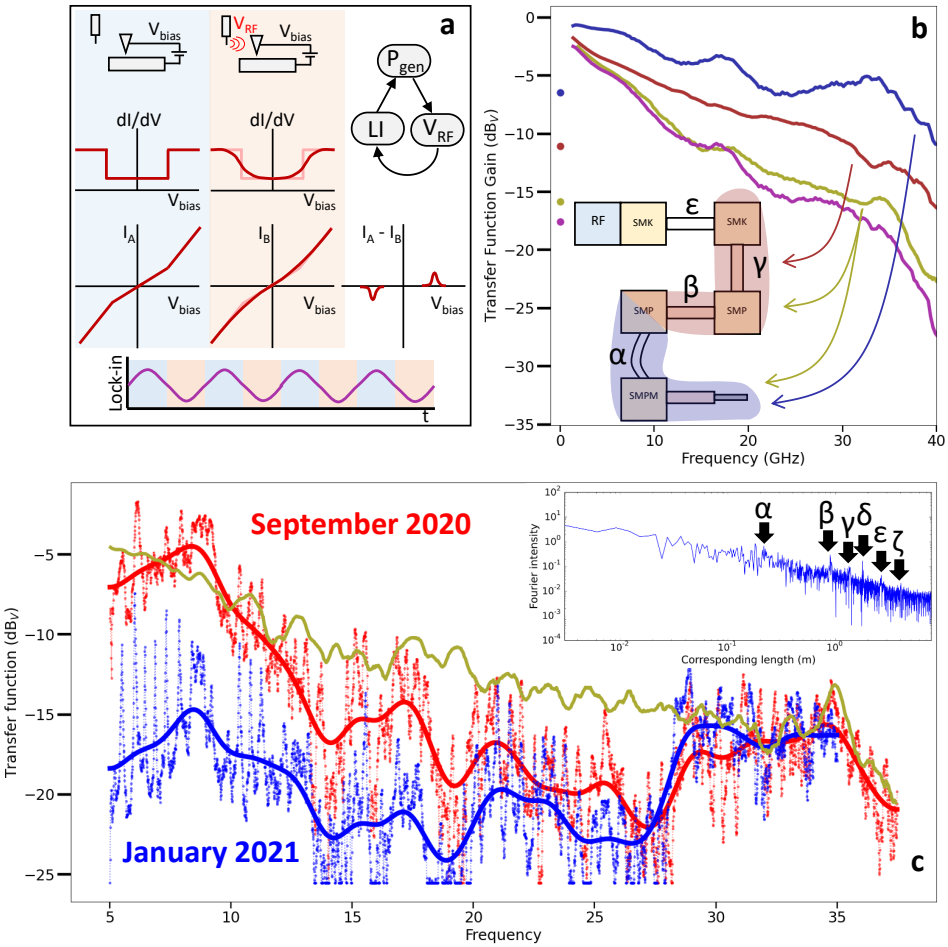

Figure 6.4: Transfer Function (a) Transfer function determination *in-situ*. An IETS step is compared with and without V_{RF} in blue and orange, respectively. The resulting current difference between the two is sent to a lock-in amplifier operating at the same frequency as the alternation rate. A feedback loop between the power sent from the generator P_{gen}, resulting in a V_{RF} and measured as a lock-in signal (LI) is used to determine the transfer function. **(b)** Transfer function *ex-situ*. Blue corresponds to the lower part of the cabling: the flex cable and an unstripped ULT-04. Red corresponds to the upper part of the cabling: from the entrance of the cryostat to the SMP connector prior to the flex cable. Purple is the numerical summation of red and blue. Yellow corresponds to the entire cryostat, i.e. red and blue together. All data is smoothed to show trends. **(c)** *In-situ* transfer functions taken in September 2020 (red) and January 2021 (blue) with a rolling average in thick. Shown is also the yellow data from panel **b**. Inset: Fourrier spectrum of September 2020 data with the x-axis showing the corresponding length for cabling with teflon as propogating medium. Six peaks indicated by Greek letters. Some of these letters also appear in panel **b**.

Figure 6.4b shows the *ex-situ* transfer function. In blue is shown the transfer function of the SMP connector attached to the flex, up until the antenna. Note that this measurement was done prior to stripping the antenna, and it was terminated with an SMK connector. In red is shown the transfer function of the cryostat cabling, ending at the same

SMP connector point. Numerically adding these two up yields the magenta curve. Actually measuring from the entry port of the cryostat until the same SMK connector on the antenna prior to stripping yields the yellow curve, which should correspond to the magenta curve. Note that in the numerical summation an additional SMP connector and an additional small piece of ULT-04 is involved, which may account for the difference, especially for higher frequencies. With this taken into account, the summation provides a good match.

Using the *in-situ* method for determining the transfer function yields Figure 6.4c. In red is shown the transfer function in September 2020, shortly after installing the antenna. This can be compared with the yellow curve, which is the *ex-situ* measurement shown in panel b, also yellow. The transfer function is a lower for the range 10 – 30 GHz. One could argue a trough in the transfer function around 20 GHz with subsequent peaks around 10 and 30 GHz, which would correspond with an antenna length of 7.5 mm and a tip equally large or larger. The transfer function was assessed with a tip about 10 mm long, but an antenna only 6.5 mm long, of which only 5.5 mm parallel to the tip. We have not done any measurements for a shorter tip to test the second mode: lower but more homogeneous transmission.

After installing the antenna, during the closing process two large electrodes need to be soldered for the magnets to function. Unfortunately these were not properly soldered and came lose during the closing of the STM. The result is that the STM had to be reopened in October 2020. During this process the cryostat may experience mechanical shocks (due to bumps, thermal shocks, etc.). After the subsequent second closing, another transfer function was established *in-situ* in January 2021, shown in blue. The transmission for lower frequencies is significantly lower. The hypothesis is that the smooth bore SMP connector, connecting the flex cable with the semi-rigid had come loose during the second opening. For a faulty connection only the high frequencies are expected to transmit properly, as lower frequencies would operate more like DC: they cannot bridge gaps. During a later opening, the connector was indeed found to have come loose. It has since been replaced with a full detente SMP connector (Pasternack PE44962).

The inset in Figure 6.4c shows the Fourrier spectrum of the unsmoothed September 2020 data. Oscillations in the transfer function are related to standing waves along the path. In total six peaks in the Fourrier spectrum, and so six standing waves have been identified, named α through ζ, some of which are also shown in panel b. All the different cables have been found, including the cable between the RF generator and the cryostat (ϵ). There are even standing waves between multiple cables, such as δ which is the sum of α and β and ζ which is a a single standing wave from the RF generator to the antenna. The presence of these standing waves indicates that the connectors provide suboptimal transmission. Fourrier analysis on the transfer function of [1] does not show such peaks in the Fourrier spectrum, indicating fewer reflections at the connectors (i.e. better soldering).

6.3. ESR RESULTS

In this section some results on TiH_B will be presented.

6.3.1. I, V_{RF} AND T DEPENDENCE

Some basic ESR tests include sweeping a certain paramater, such as current setpoint I, RF voltage V_{RF} and temperature T. These tests are shown in Figure 6.5 in panels a, b and c respectively. Meanwhile panels d, e and f show the peak height and peak width of the respective parameter sweep data. The peak height is given in ‰, i.e. per mille in terms of the tunnel current. Mathematically the peakheight can be described as [11]:

$$I_{\text{peak}} = I_{\text{sat}} \cdot \frac{\Omega^2 T_1 T_2}{\Omega^2 T_1 T_2 + 1} \tag{6.2}$$

where Ω is the Rabi flop rate, T_1 is the spin lifetime and T_2 is the spin coherence time. Once the Rabi flop rate, a function of V_{RF} and the tip's field gradient, which scales with current, becomes large, I_{peak} reaches a saturation current I_{sat} where the population of the two states of TiH_B becomes equal. The peak width can be found through:

$$\Gamma = \frac{1}{\pi T_2} \sqrt{1 + T_1 T_2 \Omega^2} \tag{6.3}$$

From panels a and c we see that the normalized peak height shows a slight increase around $10 - 15$ pA, suggesting that the as the tip gets closer, the larger magnetic field gradient increases Ω. The last two data points show a lower normalized peak height, indicating that the population shift is reaching the saturation point. The peak width, inversely proportional to the decoherence time T_2 [11] increases linearly with current. This reflects the increasing number of electrons decohering the system, resulting in a lower T_2. Finally, we note that with the offset between subsequent plots in panel a being proportional to the tunneling current spacing, a linear relationship between the current and the ESR frequency is found. This supports a linear relationship between tunneling current and tip-field [12].

The data in panels b and d, taken with a different tip apex, reveal also a linear relation between V_{RF} and peak height resulting from a larger Rabi oscillation frequency. The data shows no apparent relation between peak width and V_{RF}: just a reduction of uncertainty towards a stable value. This suggests the lifetime T_1 and decoherence time T_2 are small, compared to the Rabi flop rate Ω, most likely due to a weak tip field. The relatively small peak heights of only about 3 per mille also suggest a weak field gradient, although an alternative explanation would be a low spin polarization.

Panels c and f reveal a decreasing peak height with increasing temperature. This reflects the Boltzmann distribution reaching a unity ratio between the populations of both states. The exact peak height cannot be fit to a Boltzmann distribution, suggesting I_{sat} is not yet reached. The peak width increases, as the Fermi energy increases the decoherence from the substrate, resulting in a lower T_2 and through Equation 6.3 to a larger peak width. The peak width at 10.7K is considered to be hard too hard determine due to the

small peak size.

These results do not provide any new insights, but are a showcase of typical ESR measurements and their interpretation. Thanks to the extremely large peak height in Figure 6.5c, it is possible to measure an ESR peak above 10 K.

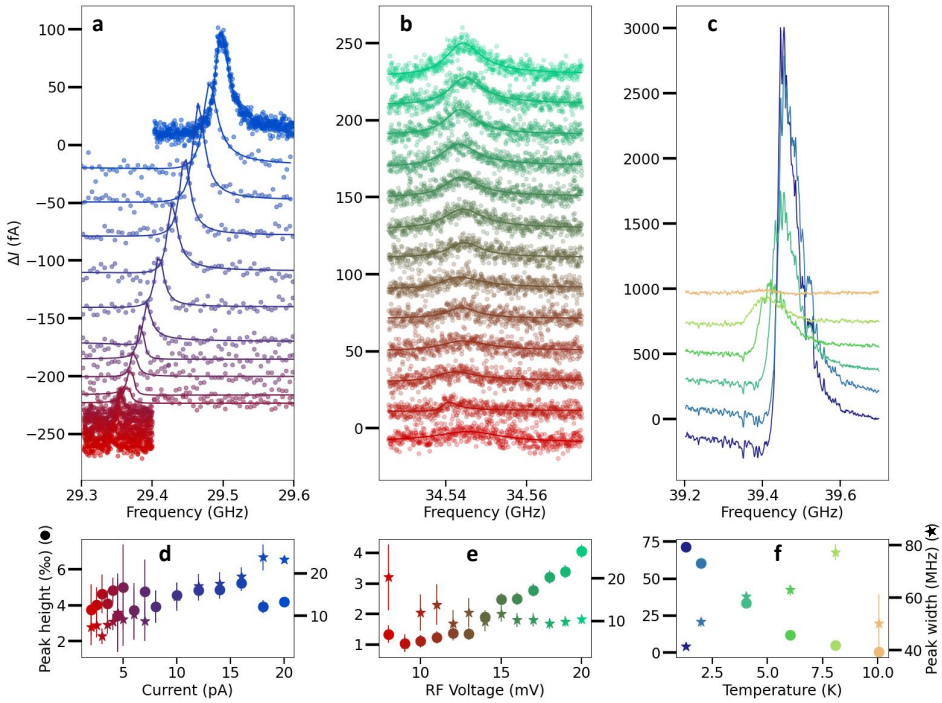

Figure 6.5: Basic ESR Parameter sweeps (a) Current sweep, from 2 pA to 20 pA. Circles are raw data, lines are fits. Subsequent sweeps are offset by 15fA per pA in their parameter setting. V_{RF} = 8 mV, V_{DC} = 50 mV, B = 1.19 T, T = 1.3 K. **(b)** RF voltage sweep, from 8 mV to 20 mV. Circles are raw data, lines are fits. Subsequent sweeps are offset by 20 fA. I = 5 pA, V_{DC} = 50 mV, B = 1.40 T, T = 1.3 K. **(c)** Temperature sweep from 1.30 T to 10.05 T. Subsequent sweeps are offset by 200 fA. I = 40 pA, V_{RF} = 20 mV, V_{DC} = 40 mV, B = 1.6 T. **(d-f)** Peak height (left axis, circles) and peak width (right axis, stars) for the data in panels **a-c**, respectively. The colors are applied correspondingly.

BIBLIOGRAPHY

1. Hwang, J. *et al.* Development of a scanning tunneling microscope for variable temperature electron spin resonance. *Review of Scientific Instruments* **93,** 093703. https://doi.org/10.1063/5.0096081 (2022).
2. Seifert, T. S. *et al.* Longitudinal and transverse electron paramagnetic resonance in a scanning tunneling microscope. *Science Advances* **6,** eabc5511. eprint: https://www.science.org/doi/pdf/10.1126/sciadv.abc5511. https://doi.org/10.1126/sciadv.abc5511 (2020).
3. Phark, S.-H. *et al. Double Electron Spin Resonance of Engineered Atomic Structures on a Surface* 2021. https://arxiv.org/abs/2108.09880.
4. Baumann, S. *et al.* Electron paramagnetic resonance of individual atoms on a surface. *Science* **350,** 417–420. https://doi.org/10.1126/science.aac8703 (2015).
5. Natterer, F. D. *et al.* Upgrade of a low-temperature scanning tunneling microscope for electron-spin resonance. *Review of Scientific Instruments* **90,** 013706. https://doi.org/10.1063/1.5065384 (2019).
6. Friedlein, J. *et al.* A radio-frequency spin-polarized scanning tunneling microscope. *Review of Scientific Instruments* **90,** 123705. https://doi.org/10.1063/1.5104317 (2019).
7. Van Weerdenburg, W. M. J. *et al.* A scanning tunneling microscope capable of electron spin resonance and pump–probe spectroscopy at mK temperature and in vector magnetic field. *Review of Scientific Instruments* **92,** 033906. https://doi.org/10.1063/5.0040011 (2021).
8. Chen, Y., Bae, Y. & Heinrich, A. J. Harnessing the Quantum Behavior of Spins on Surfaces. *Advanced Materials* **n/a,** 2107534. https://doi.org/10.1002/adma.202107534.
9. Seifert, T. S. *et al.* Single-atom electron paramagnetic resonance in a scanning tunneling microscope driven by a radio-frequency antenna at 4 K. *Phys. Rev. Research* **2,** 013032. https://doi.org/10.1103/PhysRevResearch.2.013032 (1 Jan. 2020).
10. Drost, R. *et al.* Combining electron spin resonance spectroscopy with scanning tunneling microscopy at high magnetic fields. *Review of Scientific Instruments* **93,** 043705. https://doi.org/10.1063/5.0078137 (2022).
11. Willke, P. *et al.* Probing quantum coherence in single-atom electron spin resonance. *Science Advances* **4,** eaaq1543. https://doi.org/10.1126/sciadv.aaq1543 (2018).

12. Yang, K. *et al.* Tuning the Exchange Bias on a Single Atom from 1 mT to 10 T. *Phys. Rev. Lett.* **122,** 227203. https://doi.org/10.1103/PhysRevLett.122.227203 (22 June 2019).

7

CONCLUSION

Thus, it is shown that the Hamiltonian of Equation 2.1 permits rich physics, including magnons and diabolic points, both of which can be addressed theoretically and experimentally. From a theoretical point of view, rate equations provide a sound basis, through which experiments such as IETS can be simulated. Through comparison with actual IETS measurements, one can determine the coefficient such D, E and J of the Hamiltonian. The rate equations can also be used to predict lifetimes of states, which has been used to predict the peak in the lifetime near diabolic point as a result of decreasing scattering amplitude. While these equations can be used for predictions, for a deeper understanding of such diabolic points one needs to consider Berry phases, which is outside the scope of this thesis.

Chapters 2 and 4 show that these diabolic points occur in magnetic field space at values $B_z = 0$ and $B_x = B_{\text{diab}}$, which amounts to several Tesla. The number of diabolic points increases with spin S, and so also with chain length N. For N large enough, it becomes experimentally viable to measure two such diabolic points, as the lowest-lying diabolic points move down in required B_x. These diabolic points are energy crossings between symmetric ψ_0 and antisymmetric ψ_1 (which are then inverted beyond the diabolic point). By applying a small value of B_z the energy crossings become avoided crossing, which can be seen through a slice away from the diabolic point in Figure 2.13. At this avoided crossing, states ψ_0 and ψ_1 are heavily skewed towards Néel stats N_A and N_B, leading to a reduced scattering amplitude between the two, which results in longer lifetimes as through-the-barrier transitions become less likely. Thus by measuring the lifetime with a spin-polarized STM tip and applying a voltage bias significantly below the over-the-barrier excitation voltage, a peak in the lifetime appears when sweeping B_x across the diabolic point. This is achieved both as an continuous sweep (Figure 4.2a) and discrete sweeps.

The implications of these measurements are both fundamental and technological. On a fundamental level, atomically ensembled spin chains which exhibit Berry phases

are of interest due to the rich physics they offer. Due to the extreme sensitivity of the spin lifetimes on B_x and the simplicity of the measurements presented in this thesis, these measurements offer a new way to study Berry phases. The fact that even with B_z significantly large (~ 1 T) it is easy to find a peak in the lifetime is a testimony to the robustness of the behaviour. Further relevance lies in how limited experimental literature is on this topic within spin systems, while at the same time how rich theoretical literature on this topic is.

From a technological perspective, the ability to control the lifetime of a spin chain by several orders of magnitude with a magnetic field provides opportunities for spintronics. The phenomenon can also be used for spectroscopic purposes, to determine the coupling strength between neighbouring atoms whose easy axis are perpendicular, as the value of B_x required to achieve B_{diab} seems to be affected by the tip's field. By considering the lifetime ratios of an even chain Fe_6 around its diabolic point it was determined that tip-field and the inhomogeneity of the g-factors of the individual atoms of a spin chain caused the required avoided crossing energy gap. Based on the peak width the avoided crossing energy gap can be determined beyond the limitations of thermal broadening.

Chapter 3 describes the key results, physics and implementation of STM, IETS, P&P and ESR. For the latter two Markov Chain simulations are used to showcase the time ensemble measurement that takes place during such experiments. IETS is used to identify various elements and binding sites, or even surfaces. In conjunction with the simulations of the previous chapter, the results can be used to determine coefficients of a Hamiltonian. With P&P it was found that the trimers of the remote detection set-up ("383") exhibits lifetimes roughly the same as literature values for trimers. This suggests that the trimers act independent from the neighbouring octomer. P&P has also been used to find increasing lifetimes nearing a diabolic point for Fe_3, although no data set has found a peak, suggesting this value to be outside the scope of the magnetic field available during the experiment (6 T). ESR-STM is exemplified with two extremes in measurements: the largest reported peak height of 3 pA and the peak measured a the lowest recorded current set point of 800 fA. This is achieved through extreme noise cancellation achieved by the Eve system. By pushing these limits, the range of operation can be expanded, including, for example, a situation in tunnel current is minimal impact.

Chapter 5 shows one method to remotely detect incoming magnons along a chain. The magnons exist on atomic spin chains built of Fe on $Cu_2N/Cu(100)$ and have a lifetime around 10 ps. With an estimated velocity of 50 m/s, the furthest distance recorded is about 7 nm. The magnons are injected into the chains through tunneling electrons that perform S_+ and S_- operations on the ground state. The scheme works by having an octomer default to a degenerate ground state through its even parity and symmetric neighbouring trimers in a global magnetic field along the easy axis B_z. As an incoming magnon on one of the trimers lifts the degeneracy through the coupling between the trimer and octomer, the octomer's state switching rate provides a measure for the magnon density reaching the closest atom of the trimer to the octomer. It is shown

through increasing the number of tunneling electrons by both time and current that a multi-electron process is able to randomize the octomer's state, suggesting that this multi-electron process is able to insert magnons from the trimer into the octomer. The switching rate of the octomer is not only affected by magnons, but also by full inversion of the trimer as shown by zero-Volt tip-field induced trimer inversions. The remote detection scheme thus provides a test bed for comparing theoretical predictions about magnons with experimental results, which has yielded good corroboration.

Chapter 6 gives insight into the installation of a radio frequent antenna for the purposes of ESR-STM. Chosen is a stripped CoonerWire's CW2040-3650F for its low vibration transmission and relatively good RF transmission, especially at lower temperatures. The removal of the plastic coating increasing the flexibility significantly, while lowering the RF transmission only by a small amount. It is shown that parallel antennas operate best and that peaks and troughs in the transfer function depend non-trivially on the antenna-tip distance as a result of near-field or far-field transmission. A short tip or antenna should provide a flatter transfer function as the standing wave on either can cause significant oscillations in the transfer function. *Ex-situ* measurements show this effect stronger than *in-situ*. Picking a thinner antenna or tip might improve the transfer function to a small degree, although this was considered to not be big enough to warrant a thin antenna, as the sturdiness would be lower. The standing waves not only on the antenna and tip, but also on the cables themselves can be determined through a Fourrier analysis of the transfer function, and allowed us to identify all parts of the cabling. This suggests improper connections, which, once fixed, should make the transfer function flatter. Also shown is the importance of using full detente connections, as smooth bore connections may disconnect over time. This works can provide additional reference to other groups intending on installing RF cabling for the same purpose, which is of great importance thanks to the many findings brought by ESR-STM. The chapter also provides some basic ESR-STM measurements and their interpretation as a reference.

ACKNOWLEDGEMENTS

First and foremost, I would like to thank my promotor and mentor Sander. From the honest feedback and guidance to developing myself and my research to the flexible and pun-loving (and pun-cringing) nature, I deeply appreciate the opportunity you have given me, and the effort you have put into helping me on my journey. A journey that you have supported and has lead me all the way other side of the globe.

On this other side of the globe, I would like to give a very warm thank you to Yujeong for welcoming me with open arms in your team. Within a short time, you have made me feel like an indispensable part of the team where I can freely be myself.

Of course, none of the exchange would've been possible without the support, in all ways, by Andreas and Michelle. Thank you very much for the invitation, my stay in South Korea and in particular at QNS has truly been a unique, memorable, cherished and fun experience!

In a similar international note, I want to thank Fernando for the many interesting and long discussions.

Both in Delft and in Seoul, my experience would not have been the same if it wasn't for my direct colleagues. Thank you all for having survived my endless puns, for collaborating on many interesting projects, for helping me out in times of need, for your guidance, feedback and fruitful discussions. Particular acknowledgements also go out to my four students, Cleo, Maaike, Jorn and Hester: it was a pleasure working with all of you and I myself have also learned a lot from supervising you.

While the above-mentioned people are often acknowledged also in terms of (co-)authorship, I find it also important to be thankful of those who support us throughout the entire research. Thank you Maria, Karin, Sokyeong and Hyein for the administrative support. Thank you Ronald and Erik for helping me during the many, many requests. Of course, a big thank you to all other support members such as Tino, Sangwon, Minsu and others.

My biggest and deepest appreciation goes out to you, Vanesa. Thank you for always supporting me in two different countries during my PhD, even during my not-so-forgiving work hours. Thank you, truly, for all the love and support you have given me and our family with Diva and Lady. Thank you for your keen eye, soldering tips, help with filtering, encouragement, helping analyze and always making me look forward to coming home to you. You are the love of my life and the happiness you give me on a daily basis makes it so easy to overcome any struggle I face at work. Our love is that special ingredient that makes everything so much better. I love you.

APPENDIX

A.1. OVERVIEW OF RELEVANT CONSTANTS

Constant	Name	Value	Unit	Comment	Source
g	g-factor	2.11	-	Fe on Cu-site on Cu_2N/Cu(100)	[1]
μ_B	Bohr magneton	$5.788 \cdot 10^{-}5$	$eV\,T^{-1}$	Equals $\frac{eh}{2m_e}$	[2]
S_x	Pauli spin operator	$\frac{1}{2}\begin{bmatrix} 0 & 2 & 0 & 0 & 0 \\ 2 & 0 & \sqrt{6} & 0 & 0 \\ 0 & \sqrt{6} & 0 & \sqrt{6} & 0 \\ 0 & 0 & \sqrt{6} & 0 & 2 \\ 0 & 0 & 0 & 2 & 0 \end{bmatrix}$	-	For $S = 2$	[3]
S_y	Pauli spin operator	$\frac{1}{2i}\begin{bmatrix} 0 & 2 & 0 & 0 & 0 \\ -2 & 0 & \sqrt{6} & 0 & 0 \\ 0 & -\sqrt{6} & 0 & \sqrt{6} & 0 \\ 0 & 0 & -\sqrt{6} & 0 & 2 \\ 0 & 0 & 0 & -2 & 0 \end{bmatrix}$	-	For $S = 2$	[3]
S_z	Pauli spin operator	$\begin{bmatrix} 2 & 0 & 0 & 0 & 0 \\ 0 & 1 & 0 & 0 & 0 \\ 0 & 0 & 0 & 0 & 0 \\ 0 & 0 & 0 & -1 & 0 \\ 0 & 0 & 0 & 0 & -2 \end{bmatrix}$	-	For $S = 2$	[3]
S_+	Pauli spin operator	$\begin{bmatrix} 0 & 2 & 0 & 0 & 0 \\ 0 & 0 & \sqrt{6} & 0 & 0 \\ 0 & 0 & 0 & \sqrt{6} & 0 \\ 0 & 0 & 0 & 0 & 2 \\ 0 & 0 & 0 & 0 & 0 \end{bmatrix}$	-	For $S = 2$	[3]
S_-	Pauli spin operator	$\begin{bmatrix} 0 & 0 & 0 & 0 & 0 \\ 2 & 0 & 0 & 0 & 0 \\ 0 & \sqrt{6} & 0 & 0 & 0 \\ 0 & 0 & \sqrt{6} & 0 & 0 \\ 0 & 0 & 0 & 2 & 0 \end{bmatrix}$	-	For $S = 2$	[3]
D	Uniaxial magnetic anisotropy	-1.87	meV	Fe on Cu-site on Cu_2N/Cu(100)	[4]
E	Transverse magnetic anisotropy	0.31	meV	Fe on Cu-site on Cu_2N/Cu(100)	[1]
J	Heisenberg coupling parameter	0.70	meV	$(2,0)$-spacing of Fe on Cu-sites	[5]
J'	Heisenberg coupling parameter	-0.05	meV	$(3,0)$-spacing of Fe on Cu-sites	[4]
J_{xy}	Heisenberg coupling parameter	?	meV	$(?,?+\frac{1}{2})$-spacing of Fe on Cu-sites	-

BIBLIOGRAPHY

1. Hirjibehedin, C. F. *et al.* Large Magnetic Anisotropy of a Single Atomic Spin Embedded in a Surface Molecular Network. *Science* **317,** 1199–1203. https://doi.org/10.1126/science.1146110 (2007).
2. Mohr, P. J. & Taylor, B. N. CODATA recommended values of the fundamental physical constants: 1998. *Rev. Mod. Phys.* **72,** 351–495. https://doi.org/10.1103/RevModPhys.72.351 (2 Apr. 2000).
3. Wheeler, N. *Remarks concerning the explicit construction of SPIN MATRICES FOR ARBITRARY SPIN* Aug. 2000.
4. Elbertse, R., Coffey, D., Gobeil, J. & Otte, A. Remote detection and recording of atomic-scale spin dynamics. *Communications Physics* **3.** https://doi.org/10.1038/s42005-020-0361-z (May 2020).
5. Bryant, B., Spinelli, A., Wagenaar, J. J. T., Gerrits, M. & Otte, A. F. Local Control of Single Atom Magnetocrystalline Anisotropy. *Phys. Rev. Lett.* **111,** 127203. https://doi.org/10.1103/PhysRevLett.111.127203 (12 2013).

CURRICULUM VITÆ

Robbie ELBERTSE

25-11-1992	Born in Zoetermeer, the Netherlands.

EDUCATION

2004–2010	Secondary School Erasmus College, Zoetermeer (2004–2008) Bataafs Lyceum, Hengelo (2008–2010)
2010–2014	BSc. Applied Physics, BSc. Applied Mathematics Delft University of Technology Universidad de Buenos Aires (2013)
2014–2017	MSc. Applied Physics Delft University of Technology
2018-2022	PhD. Physics Delft University of Technology Visitor at: Center for Quantum Nanoscience *Thesis:* Lifetime of Atomic Spin Chains *Promotor:* Prof. dr. A. F. Otte

AWARDS

2020	Nominated Best Poster FYSICA Conference
2021	3rd Place Promotion Article NTvN
2021	Article placed in Dutch Vacuum Society (NEVAC) newsletter
2022	Nominated Award IVC-22

LIST OF PUBLICATIONS

2. J. Hwang, D. Krylov and **R.J.G. Elbertse**, S. Yoon, T. Ahn, J. Oh, L. Fang, W. Jang, F.H. Cho, A.J. Heinrich and Y. Bae *Development of a scanning tunneling microscope for variable temperature electron spin resonance,* Review of Scientific Instruments **93**, 093703 (2020).

1. **R. J. G. Elbertse**, D. Coffey, J. Gobeil and A.F. Otte *Remote detection and recording of atomic-scale spin dynamics,* Commun Phys **3**, 94 (2020).